DISS. ETH NO. 19447

MICROFORCE-SENSING PROBES AND METHODOLOGIES FOR MICROMECHANICAL AND DIMENSIONAL METROLOGY

A dissertation submitted to

ETH ZURICH

for the degree of

DOCTOR OF SCIENCES

presented by

Simon D. Muntwyler

MASTER OF SCIENCE, ETH ZURICH
Born on December 21, 1980
Citizen of Zurich

Accepted on the recommendation of

Prof. Dr. Bradley J. Nelson, examiner
Prof. Dr. Peter Bøggild, co-examiner

2010

Preface

This Ph.D. thesis describes the work performed during an intensive time at the Institute of Robotics and Intelligent Systems at ETH Zurich. The primary objective of this project was to develop novel, revolutionary tools, systems and methodologies enabling a new approach to metrological problems in the microworld.

The result obtained in the course of this thesis would not have been possible without the support of a number of people. First and foremost, I would like to thank my adviser Prof. Bradley Nelson for giving me the opportunity to work on this topic during my studies as well as creating a very friendly and creative working atmosphere. Additionally I would like to thank Prof. Peter Bøggild for his time and effort in the co-advising of this thesis. I would also like to express my gratitude to all the members of the Institute of Robotics and Intelligent Systems for their support, advice and countless fruitful discussions on the subject. Further, I am also very grateful for the collaboration with a number of scientific colleagues, including Joey Doll and Enrico Klotzsch.

Abstract

The increasing interest in investigating ever smaller samples and the industrial trend toward miniaturization has created a need for novel metrological tools and methodologies for micromechanical and dimensional measurements in the nanonewton to micronewton range and nanometer to millimeter range.

The most common instrument of choice, the atomic force microscope, imposes a number of limitations, such as off-axis displacements when loaded and the restriction to low aspect ratio samples with small step heights. Even in spite of the metrological limitations of this cantilever-based system, viable alternatives are nevertheless scarce. Besides the need for metrological tools, no standardized methodology for their calibration and the calculation of their measurement uncertainties exist to date. Therefore the majority of the results obtained and published in the nanonewton to micronewton force range are not traceable back to SI-units, rendering the estimation of their accuracy impossible.

With this problem in mind, the goal of this thesis was to develop novel microfabricated, MEMS-based metrological tools and systems as well as the methodologies necessary for traceable force measurements in the micronewton to nanonewton range. During the course of this thesis the first three-axis microforce-sensing probe was developed, enabling the simultaneous measurement of forces in the x-, y-, and z-directions with submicronewton resolution. Therefore a novel microfabrication process has been developed, enabling a major reduction in the fabricational complexity of multi-axis in- and out-of-plane sensors and actuators. And by combining sensing as well as actuation elements on a single chip, the first monolithically integrated multi-axis microtensile-tester chip has been developed, allowing the direct measurement of the mechanical as well as electrical properties of a sample along multiple directions.

Motivated by the unavailability of reference standards in the nanonewton range, a methodology for the calibration of microforce sensors has been developed. In combination with the implementation of the latest advancement in the field of multivariate uncertainty analysis using a Monte Carlo method, this allows for SI-traceable microforce measurements in the nanonewton to micronewton range. As a first in literature, the utilization of capacitive-based

microfabricated force-sensing-probes – with a four-spring configuration allowing for a parallel motion when deflected, and integrated capacity-to-voltage converter – is proposed as an ideal transfer standard for the dissemination of the primary reference standard from national metrology institutes in the nanonewton to micronewton force range.

Accurate microforce-sensing tools are only one component necessary for micromechanical or dimensional measurements. Therefore, the development of an automated microcoordinate and property measuring machine (μCPMM) is presented allowing for true three-dimensional metrology that enables the measurement of topographical and stiffness maps of complex samples.

To finalize this work, the functionality of these tools and systems is demonstrated on a number of applications, for which up-to-date no-quantitative investigation has been possible. This should clearly indicate the importance of the results, presented in this thesis, as well as their potential to enable new possibilities for researchers in different fields and various industrial applications.

Zusammenfassung

Getrieben durch die kontinuierliche Miniaturisierung und das zunehmende Interesse an immer kleineren Komponenten und Proben wurde ein Bedürfnis für messtechnische Instrumente geschaffen, welche es ermöglichen, Kräfte im Mikro- und Nanonewton-Bereich zu messen.

Das bis anhin vorwiegend verwendete Messinstrument, das Rasterkraftmikroskop (AFM), hat diverse Nachteile wie zum Beispiel laterale Bewegung bei einer vertikalen Belastung oder die Einschränkung auf Proben, deren Strukturen nur ein kleines Aspektverhältnis vorweisen. Trotz der zahlreichen Limitationen des Rasterkraftmikroskops gibt es bis jetzt noch keine brauchbare Alternative. Nebst der Notwendigkeit neuer Instrumente existiert keine standardisierte Methodik für die auf die SI Einheiten rückführbare Kalibration solcher Instrumente und der Abschätzung derer Messunsicherheiten. Daher sind der Grossteil der publizierten Resultate im Mikro- und Nanonewton-Bereich nicht rückführbar und die Abschätzung derer Genauigkeit nicht möglich.

Basierend auf dieser Problemstellung liegt der Fokus dieser Arbeit in der Entwicklung neuartiger mikromechanischer Instrumente und Systeme, wie auch einer Methodik, die es ermöglicht, rückführbare Kraftmessungen im Mikro- und Nanonewton-Bereich zu machen.

Im Laufe dieser Arbeit wird der erste Dreiachsen-Mikrokraftsensor präsentiert, der es ermöglicht, simultan Kräfte in allen drei Raumrichtungen mit Submikronewton Auflösung zu machen. Im weiteren wird ein neuartiger Mikrofabrikationsprozess vorgestellt, der es ermöglicht, Mehrachsen-Sensoren wie auch Mehrachsen-Aktuatoren mit stark reduzierter Fabrikationskomplexität herzustellen, was ein wesentlicher Beitrag an eine zukünftige, kommerzielle Verfügbarkeit solcher Instrumente leisten kann. Weiter wurde durch die Kombination von Sensor- and Aktuationsprinzipien auf einem Chip die erste integrierte Mehrachsen-Mikrozugmaschine entwickelt, die ein mechanisches Testen kleinster Proben erlaubt.

Motiviert durch die Nichtverfügbarkeit von Referenzsystemen im Nanonewton-Bereich wird eine Methodik für die Kalibration von Mikrokraftsensoren präsentiert, die in Kombination mit den neusten Entwicklungen im Bereich der Multivarianten Unsicherheitsanalyse mittels einer Monte Carlo Methode die rückführbare Kalibration von Mikrokraftsensoren im Mikro- und Nanonewton-Bereich ermöglicht.

Durch die Kombination der Mikrokraftsensoren mit motorisierten Mikromanipulatoren, Kameras, Kontrollelektronik und Software wird ein komplettes Mikrokoordinaten und mechanische Eigenschaften messendes System entwickelt, das die automatisierte Messung von Topographien und mechanischen Eigenschaften erlaubt. Um das Potenzial dieser Instrumente und Systeme zu demonstrieren wird deren Anwendung in verschiedenen Applikationen präsentiert, die klar machen, wie die Resultate dieser Arbeit dazu beitragen, neue Möglichkeiten für die Erforschung kleinster Proben und die Entwicklung neuer miniaturisierter Produkte zu erschliessen.

Contents

Preface ..... **I**

Abstract ..... **II**

Zusammenfassung ..... **IV**

Contents ..... **VI**

List of Tables ..... **VIII**

List of Figures ..... **IX**

1 Introduction **1**

1.1 Motivation 1

1.2 Current Status and Challenges 2

1.3 Potential Technological Impact 5

1.3.1 MEMS Test Equipment Market 5

1.3.2 Microcoordinate Measuring Machine (μCMM) Market 5

1.3.3 Micromechanical Material Testing Market 6

1.3.4 Summary 7

1.4 Objectives 7

1.4.1 Microforce-Sensing Tools 8

1.4.2 Calibration and Uncertainty Analysis Methodology 8

1.4.3 System Integration 8

1.5 Organization 9

2 Microforce-Sensing Probes **10**

2.1 Microforce-Sensing Technologies 10

2.2 Capacitive Microforce Sensing 12

2.3 MEMS Technology for Microfabricated Force-Sensing Probes 14

2.4 Single-Axis MEMS-Based Capacitive Microforce-Sensing Probes 19

2.5 Multi-Axis MEMS-Based Capacitive Microforce-Sensing Probes 21

2.6 Monolithically Integrated MEMS-Based Microtensile Tester on a Chip 27

2.7 Microfabrication Processes 30

2.8 Capacity-to-Voltage Conversion 33

2.9 Summary 35

3 Sensor Calibration and Uncertainties Analysis 36
3.1 Small-Force Metrology: Current Status and Challenges 36
3.2 Uncertainty Analysis 41
3.3 Sensor Characteristics 45
3.4 Calibration of the Single-Axis Reference-Force Sensor 48
3.5 Calibration of Single-Axis MEMS-Based Microforce-Sensing Probes 53
3.6 Calibration of Multi-Axis MEMS-Based Microforce-Sensing Probes 58
3.7 Calibration of the Multi-Axis Position Feedback Sensors 61
3.8 Range Tunable Microforce Sensing 65
3.9 Summary 70

4 System Integration: Microcoordinate and Property Measuring Machine 71

5 Measurement Applications 77
5.1 Topographical Measurements of Optical Lenses 77
5.2 The Stress-Versus-Strain Curves of Single Fibronectin Fibers 79
5.3 Measuring the Touch Sensitivity of Microorganisms 82
5.4 Stiffness Measurement of Individual Petunia Trichome Cells 84
5.5 Summary 88

6 Summary and Contributions 89

7 References 92

8 Appendix 99
8.1 Additional Source of Uncertainty 99
8.2 Process Sequence for the SOI-Based Tools 100
8.3 Process Sequence for the Double SOI-Based Tools 103
8.4 Capacitive Readout Schematics 107
8.5 Calibration Setup Schematic 109

Curriculum Vitae 110

List of Tables

Table 1: Design parameters of the single-axis MEMS-based capacitive microforce-sensing probe 21
Table 2: Design parameters of the two-axis MEMS-based capacitive microforce-sensing probe 23
Table 3: Design parameters of the three-axis MEMS-based capacitive microforce-sensing probe 26
Table 4: Design parameters of the two-axis microtensile-tester's actuator and position feedback sensors 29
Table 5: Young's modulus measurements of the same silicon specimen with different AFM cantilevers [48] 37
Table 6: Terms and definitions in the uncertainty analysis [60] 42
Table 7: Uncertainties in the single-axis reference-force sensor calibration 51
Table 8: Calibration and uncertainty analysis results: single-axis reference-force sensor 52
Table 9: Calibration and uncertainty analysis results: single-axis MEMS-based microforce-sensing probe 57
Table 10: Calibration and uncertainty analysis results: two-axis MEMS-based microforce sensor (tensile tester) 60
Table 11: Calibration and uncertainty analysis results: two-axis position feedback sensors in the microtensile tester 64
Table 12: Three-axis MEMS-based capacitive microforce-sensing probe characteristics at two different CVC settings 69
Table 13: Technical specifications of the microcoordinate and property measuring machine (μCPMM) 73
Table 14: Parameters for the spin-coating of the AZ 4562 as well as the S1813 photoresist 101
Table 15: Parameters for the spin-coating of the AZ 4562 photoresist (device layer) 105

List of Figures

Fig. 1: Different approaches for the measurement of small forces in the micronewton to nanonewton range based on the measurement of the displacement of the movable body; (a) by visually observing an attached vernier [8], (b) by visually measuring the movement of a reference point to the measurement point [9], (c) by a miniaturized optical encoder [10] and (d) by measuring a capacitive change between attached electrodes [11]..... 3

Fig. 2: (a) Microcoordinate measuring machine F25 by Carl Zeiss AG [29], (b) Microcoordinate measuring machine UMAP103 by Mitutoyo Corp.[30]. 6

Fig. 3: (a) and (b) Electrostatic force balance (EFB) developed by NIST [31], (c) Piezoresistive microforce-sensing cantilever developed by (PTB) [32]. 10

Fig. 4: (a) Photograph and (b) schematic of a single-axis cantilever-based capacitive microforce sensor. 13

Fig. 5: Relationship between the relative displacement and the relative capacitive change in a differential capacitive microforce sensor as shown in Fig. 4.... 14

Fig. 6: Schematic of a photolithographic process [38]. 16

Fig. 7: Schematic of the advanced silicon etch (ASE) process developed by Surface Technology Systems Plc.(STS). 17

Fig. 8: (a) Photograph and (b) schematic of a single-axis MEMS-based capacitive microforce-sensing probe (the immovable outer frame is not shown)..... 19

Fig. 9: (a) Photograph and (b) schematic of a two-axis MEMS-based capacitive microforce-sensing probe (the immovable outer frame is not shown)..... 22

Fig. 10: Cross section of the sensing capacitor, visualizing the bidirectional out-of-plane sensing principle. 23

Fig. 11: (a) Photograph and (b) schematic of a three-axis MEMS-based capacitive microforce-sensing probe (the immovable outer frame is not shown)..... 24

Fig. 12: Mechanical response of the three-axis MEMS-based capacitive microforce-sensing probe to an applied force in: (a) the x-direction, (b) the y-direction and (c) the z-direction. 25

Fig. 13: Close-up views of the three-axis MEMS-based capacitive microforce-sensing probe. 25

Fig. 14: (a) Photograph and (b) schematic of the monolithically integrated MEMS-based two-axis microtensile tester (the chip size is 7 mm by 10.8 mm). 27

Fig. 15: Schematic of one single-axis electrostatic actuator with integrated capacitive position feedback sensor..... 28

Fig. 16: Schematic of the SOI-based microfabrication process for in-plane sensing and actuation. 31
Fig. 17: Schematic of the double SOI-based microfabrication process for in- and out-of-plane sensing. 32
Fig. 18: Schematic of the electrical connections from a single-axis capacitive microforce-sensing probe to the capacity-to-voltage converter. 33
Fig. 19: Block diagram of the capacity-to-voltage converter IC (MS3110 and CVC 1.1). 34
Fig. 20: Redefining the primary standard of the kilogram: (a) The avogadro project by NPL [50], (b) The watt balance project by NPL [50]. 38
Fig. 21: Schematic of the Monte Carlo method (MCM). 43
Fig. 22: Cause and effect diagram for the propagation of the diverse sources of uncertainty in the calibration chain. 44
Fig. 23: Initial stabilization characteristic of a microforce-sensing probe based on the MS3110 CVC. 47
Fig. 24: Calibration results of the single-axis reference-force sensor consisting of (a) the calibration data (x) as well as the best estimate (-), the 68% (--), and the 95% (..) coverage intervals of the calibration curve, (b) – (d) contour lines of the multivariate PDF of the calibration coefficients for coverage probabilities of 10%, 30%, 50%, 70% and 90%, projected onto the calibration coefficient plane of (b) c_1 and c_2 (c) c_1 and c_3 (d) c_2 and c_3. 48
Fig. 25: (a) Sensor output voltage V_j and the moving average filter output voltage $V_{MA,j}$; (b) standard uncertainty due to the sensor output signal drift as a function of the time interval, extracted from the data in (a). 50
Fig. 26: Numerical stabilization of the MCM with the increasing number of iterations for the standard deviation of (a) the calibration coefficients, (b) the uncertainty in the calibration coefficients, (c) the correlation coefficients and (d) the expansion coefficients. 52
Fig. 27: Calibration results of the single-axis MEMS-based microforce-sensing probe consisting of (a) the calibration data (x) as well as the best estimate (-), the 68% (--), and the 95% (..) coverage interval of the calibration curve, (b) – (d) contour lines of the multivariate PDF of the calibration coefficients for coverage probabilities of 10%, 30%, 50%, 70% and 90%, projected onto the calibration coefficient plane of (b) c_1 and c_2 (c) c_1 and c_3 (d) c_2 and c_3. 53
Fig. 28: The probability density function of (a) the input range and (b) the resulting dimensional *overetch*, extracted from the calibration of 371 single-axis

MEMS-based microforce-sensing probes. 54
Fig. 29: Cross sensitivity measurement data (x) as well as the best estimate (-) and its standard uncertainty (-) for the applied force (a) in the z-direction and (b) in the y-direction..... 55
Fig. 30: Influence of (a) the relative humidity change from 82% RH to 18% RH (at 25.2 ± 0.9 °C) and (b) the environmental temperature change from 10 °C to 40 °C (at 59 ± 19% RH) on the sensor's output voltage offset and sensing gain. 56
Fig. 31: Calibration results of the two-axis MEMS-based microforce sensor (tensile tester) consisting of the calibration data (+,*) as well as the best fit (-), 68% (--), and 95% (..) coverage intervals of the calibration curve in (a) the x-direction and (b) the y-direction, and contour lines of the multivariate PDF of the calibration coefficients in (c) $\boldsymbol{A}_x$ and (d) $\boldsymbol{A}_y$ for coverage probabilities of 10%, 30%, 50%, 70% and 90%. 59
Fig. 32: Microscope picture of the tensile tester's end effectors with the geometrical model fitted to its outline, used for the visual rigid body tracking..... 62
Fig. 33: Calibration results of the tensile tester's two-axis position feedback sensor in the actuated arm consisting of the calibration data (+,*) as well as the best fit (-), 68% (--), and 95% (..) coverage intervals of the calibration curve (a, c) in the x-direction and (b, d) in the y-direction, contour lines of the multivariate PDF of the calibration coefficients in (e) $\boldsymbol{A}_x$ and (f) $\boldsymbol{A}_y$ for coverage probabilities of 10%, 30%, 50%, 70% and 90%. 63
Fig. 34: Gravitational, electric, Van-der-Waals, and surface tension attractive forces between a sphere and a plane as a function of the their characteristic dimension [66]..... 65
Fig. 35: Calibration curves for the single-axis MEMS-based capacitive microforce-sensing probe for varying C_{int}..... 65
Fig. 36: Sensor characteristics for the single-axis MEMS-based capacitive microforce-sensing probe for varying C_{int} and *Gain*. 66
Fig. 37: Sensor characteristics for the three-axis MEMS-based capacitive microforce-sensing probe for varying C_{int} and *Gain*. 67
Fig. 38: The calibration curves of the three-axis MEMS-based microforce-sensing probe for the two different CVC settings indicated in Table 12 (squares indicate the raw calibration data V_x, circles V_y and triangles V_z)..... 68
Fig. 39: (a) Microcoordinate and property measuring machine (μCPMM); (b) micromechanical testing system on inverted microscope. 71

Fig. 40: Schematic of the direct linear transformation (DLT) from the camera image plane to the object plane. 74
Fig. 41: Force versus position measurement data at a single sample location and its linear extrapolation to extract the topographical height and stiffness α of the sample at the current location. 75
Fig. 42: (a) Photograph of the sensing probe used for coordinate measuring applications, realized by attaching a tungsten wire with tip radius of approximately 100 nm; (b) topographical map of an optical lens obtained using the μCPMM presented in Chapter 4. 78
Fig. 43: Photograph of the single-axis MEMS-based microforce-sensing probe with attached tungsten wire, capable of measuring forces lateral to its probe and (b) its calibration data and linear fit..... 79
Fig. 44: (a), (b) Photographs and (c), (d) results of the stress-versus-strain curve measurement of a single Fn fiber with a diameter of 3.5 ± 0.2 μm suspended over a trench with a width of 30 μm..... 80
Fig. 45: (a) – (d) Photograph of a Fn fiber during its recovery from the extended state, (e), (f) results from the investigation of the mechanical property recovery after variable recovery periods t_w. 81
Fig. 46: (a) Results and (b) photograph of the touch sensitivity measurements on different C. elegans strains. 83
Fig. 47: Photography of the two-axis microtensile tester aligned with a trichome of the petunia plant (W115). 85
Fig. 48: All 10 measurement curves on one of the nine measurement locations on the trichome cell: The upper curves are the results from compressing and the lower curves are the results from releasing the cell. The dashed lines are linear fits to the data between the upper and the lower limit..... 86
Fig. 49: Measurement results of the trichome cell characterization: (a) The microtensile tester's end effectors aligned with the trichome indicating the region of the stiffness measurements, (b) results of the stiffness-versus-cell-diameter measurement for the compression of the cell, (c) results of the stiffness-versus-cell-diameter measurement for the releasing of the cell..... 87
Fig. 50: (a) Photograph and (b) circuit schematic of the printed circuit board for the-single channel capacity-to-voltage conversion based on the MS3110 IC.. 107
Fig. 51: Photograph of the printed circuit board for the (a) three- and (b) four-channel capacity-to-voltage conversion based on the CVC1.1 IC..... 107
Fig. 52: Circuit schematic of the printed circuit board for the three-channel capacity-

to-voltage conversion based on the CVC1.1 IC. 108
Fig. 53: Schematic of the calibration setup used for single- and multi-axis microforce and position feedback sensor calibration. 109

1 Introduction

This chapter provides an introduction to the current status of and challenges in the field of microforce-sensing probes for micromechanical and dimensional metrology. An overview of the current approaches used in the development of such systems, as well as a short description of the open challenges, is given; these motivated the developments made within the course of this work. Additionally an estimate of the potential impact of this technology on the industrial market is presented, underlying its importance. Finally, the objectives and organization of this thesis are presented.

1.1 Motivation

Advances in miniaturization technologies have had dramatic impacts on our lives. Radios, computers, and telephones that once occupied large spaces now fit in the palm of a hand [1]. Using specially developed microfabrication processes, large electronic circuits and components are integrated into millimeter-sized integrated circuit (IC) chips. In addition to the benefit of enabling smaller components, microfabrication offers other advantages, such as reduced production costs due to a highly parallelized batch fabrication and better performance. Microelectromechanical systems (MEMS) utilizes these fabrication processes originally developed for the IC industry, to produce mechanical structures and components as well as integrate mechanical systems such as sensors and actuators with electronics on a common silicon substrate. “Small is beautiful [2]” because small is better: With increasing miniaturization, devices often yield better performance, such as faster response time or higher sensitivity. But due to the microscopic dimensions of these devices or components, conventional, macroscopic tools for the testing and especially mechanical characterization have reached their limitations. Besides this industrial trend towards ever smaller components, the focus in various fields of research such as plant biology has shifted from studying the organization of the whole body or individual organs toward the behavior of the smallest units of the organism, the individual cell [3]. Measuring the mechanical characteristics of a cell by

applying a force can give insights into its structures or functionalities since the mechanical properties of biological materials are tightly coupled to their physiological functions.

For the continuous, successful industrial miniaturization and ongoing investigation of smaller samples in research, a new set of metrological tools for testing and characterization are required.

1.2 Current Status and Challenges

The most commonly used system for dimensional and mechanical investigation of microscopic samples and devices is the atomic force microscope (AFM). Primarily developed for dimensional metrology, the AFM also allows for the measurement of small forces. It consists of a bending beam with a sharp tip at its end, attached to a micropositioner, allowing it to be scratched over a surface or pushed against a sample. The deflection of the beam, which is proportional to the force acting on its tip, is calculated by measuring the displacement of an optical beam reflected from its surface. This approach offers high spatial as well as force resolution but involves a number of limitations, which makes it a poor choice for a variety of applications.

For dimensional metrology the AFM-based techniques are limited to low aspect ratio and step heights and therefore are not suitable for true three-dimensional (3-D) metrology. Although optical systems are frequently used – offering high measurement speeds, noncontact measurement modes and high vertical resolution – their lateral resolution is limited and they can also only be used for samples with low aspect ratio [4]. Therefore increasing effort currently is being made by different research institutes and companies like Carl Zeiss AG or Mitutoyo Corp. in the development of force-probe-based microcoordinate measuring machines (μCMM) but these are currently limited to forces in the hundreds of micronewtons or probe tips in the tens of micrometers.

For the micromechanical testing of small samples such as the measurement of the stiffness of biological cells or microfabricated structures the AFM-based technique is limited in its versatility. Due to the large size of the optical beam deflection measurement system, the AFM is difficult (if not impossible) to integrate into a complete testing system with a high-resolution microscope, such as a scanning electron microscope (SEM). Although much effort has been made in the development of fully integrated AFMs, where the optical beam deflection principle is replaced by, e.g., a piezoresistive sensing element [5], [6], these sensors are usually limited to single-axis measurements and are based on the deflection of a cantilever. Cantilever-based sensors are sensitive to off-axis loads and induce lateral motions when they are deflected,

inducing slippage in the worst case. Given the metrological limitations of the cantilever as a force sensor, which are acknowledged and appreciated by most in the AFM community, it is interesting that viable alternatives are still scarce [7].

With the advancement of MEMS technology, fabrication techniques have become available for the development of a new generation of microforce-sensing probes with the potential to overcome the limitations of the cantilever-based techniques. Driven by the increasing number of applications requiring the measurement of small forces in different fields such as mechanobiology, material sciences, microrobotics and life sciences, microforce-sensing probes based on various different approaches have been developed. An overview of four different approaches, to overcome the drawbacks of the cantilever-type sensors are shown in Fig. 1. The applied force is transferred to a parallel displacement, which is measured by different means. Therefore, a central shuttle is suspended by four flexures (two on each side) within an outer frame. The flexure, modeled as a linear spring, results in a deflection of the body proportional to the applied force. The benefits of using this four-flexure configuration with high aspect ratio flexure lie in its parallel motion, derby-eliminating lateral tip motion, and low sensitivity to off-axis forces.

In Fig. 1(a) and (b) the displacement of this central shuttle is measured optically using a high-resolution microscope. In Fig. 1(a) a vernier-type grid is integrated into the sensor [8] and in

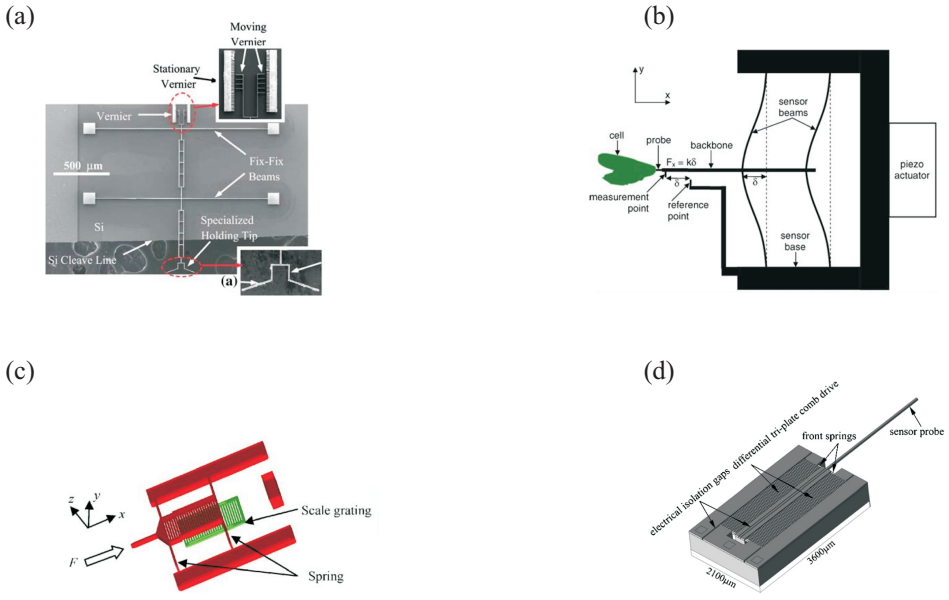

Fig. 1: Different approaches for the measurement of small forces in the micronewton to nanonewton range based on the measurement of the displacement of the movable body; (a) by visually observing an attached vernier [8], (b) by visually measuring the movement of a reference point to the measurement point [9], (c) by a miniaturized optical encoder [10] and (d) by measuring a capacitive change between attached electrodes [11].

Fig. 1(b) the relative movement of a reference point to the measurement point is visually measured [9]. A higher level of integration is shown in Fig. 1(c) and (d) where no visual feedback of the sensor is needed. In Fig. 1(c) a miniaturized optical encoder is integrated into the sensor, which measures the relative movement using a laser and a photo detector [10], and in Fig. 1(d) the displacement is measured by attached capacitive electrodes as a variation of the capacitance [12], [13]. These MEMS-based microforce-sensing probes are designed for micromechanical measurements that typically involve forces from micronewtons to nanonewtons. For the measurement of smaller forces, other technologies, such as a magnetically or optically trapped particle referred to as magnetic or optical tweezers [14], [15], are more commonly used. More recently increasing efforts have been made to extend these principles for the development of multi-axis sensors. In most cases the measurement of additional force components offers a great advantage, e.g., in the case of automated cell injection [16], since a misalignment of the cell and the injection pipette can be detected and compensated for. In [17] a two-axis piezoelectric microforce sensor and in [4], [18], [19], [20] three-axis microforce sensors based on piezoresistive materials are presented. The combined measurement of forces and torques has been demonstrated in [21] based on piezoresistive sensing and in [22] based on capacitive sensing. In [23] a full six-axis capacitive force / torque sensor is presented.

The development of the microforce-sensing probes have opened up new possibilities for researchers from different fields to perform quantitative measurements, e.g., of the forces involved in microassembly [17] or micromanipulation tasks [18], or in micromechanical material testing such as nanoindentation [13]. A large number of novel applications can be found in the emerging field of micromechanobiology, such as the measurement of the injection force or force-displacement curves of drosophila or mouse embryos [10], [11] or the force response of a cell when stretched [9]. Like an AFM, microforce-sensing probes can also be used for dimensional metrology [4] in a coordinate measuring machine (CMM), such as the F25 developed by Carl Zeiss AG. However, none of the presented approaches allow for submicronewton multi-axis measurements, limiting the resolution for micromechanical as well as dimensional metrology. And due to their relative complex microfabrication processes or the need for microassembly steps, these sensing probes are not widely available.

Despite the need for high-resolution multi-axis microforce-sensing tools, currently neither a standardized calibration methodology nor an SI-traceable reference standard exist for the calibration of forces in the nanonewton range, making the estimation of their measurement accuracy in most cases impossible.

1.3 Potential Technological Impact

In addition to the potential of accurate microforce-sensing probes in various fields of research, they will also have a great impact on a variety of industrial applications. The three most relevant markets in which these novel probes will open new possibilities are:

- **MEMS test equipment market**
- **Microcoordinate measuring machine (μCMM) market**
- **Micromechanical material testing market**

Driven by the trend of miniaturization, new applications in well-established markets, such as the CMM market and mechanical material testing market, are creating specialized subsectors for the testing and measuring of properties in the microscale, e.g., the subsector nanoindentation in the case of material testing. Due to the novelty of these subsectors, the estimation of their size is difficult and therefore based on extrapolations from data of the existing, established markets.

In the following section the most relevant information regarding these three markets is summarized based on reports from Frost & Sullivan [24], [25], [26], [27], and some extrapolations.

1.3.1 MEMS Test Equipment Market [24]

Successful wafer-level testing of MEMS dies can eliminate undetected nonfunctional dies, thereby saving significant revenues and packaging costs, as well as reducing the time to market. According to [24] the worldwide revenue created by the MEMS test-equipment market in 2007 is $56.5 million with a growth rate of about 11% (forecast for 2010 was $76.4 million). To date only electrical testing has become an integral part of the MEMS production, due to the lack of standardized mechanical testing equipment. Once standard test equipment that includes both electrical and mechanical testing is developed, the MEMS test equipment market is expected to witness high growth rates. Therefore, accurate, microforce-sensing probes with integrated electrical testing capabilities could be the key to entering into this market.

1.3.2 Microcoordinate Measuring Machine (μCMM) Market [25], [26], [28]

Even with all the advancements in noncontact 3-D measurement technologies, such as optical or laser-based systems, and the ability to accurately measure into the submicron range, there is still a need for contact probing for dimensional metrology. Although optical or laser-based systems can quickly measure small visible features, they cannot measure into deep, narrow holes or around feature edges such as undercuts. This is where touch probes are still the technology of choice. Microtouch probes are most commonly part of a multisensor system. In such systems,

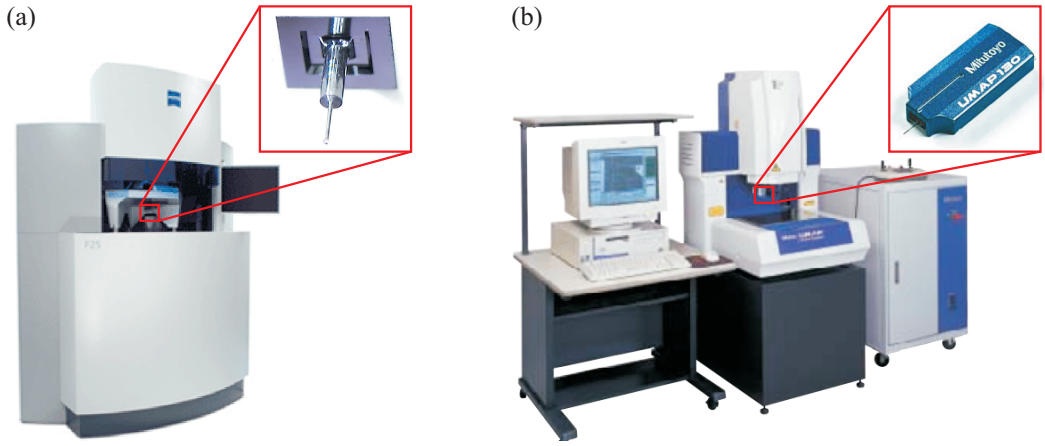

Fig. 2: (a) Microcoordinate measuring machine F25 by Carl Zeiss AG [29], (b) Microcoordinate measuring machine UMAP103 by Mitutoyo Corp.[30].

larger features are most commonly measured optically, whereas only the critical regions are measured with the touch probe sensor. The data from both sensors are then aligned through the use of software. Typical industrial applications for µCMM are in the quality control of ports on fuel injection nozzles, implantable medical devices, miniature watch components, miniature injection moldings and components for sensor technologies.

According to [25] the worldwide revenue created by the entire CMM market in 2004 was $1,112 million with a growth rate of about 5% (the forecast for 2010 is $1,476 million). Only three companies share the majority of the CMM market. They are Carl Zeiss AG with a market share of 28%, Hexagon Metrology with 27.5% and Mitutoyo Corp. with 22%. The µCMM market is a future market whose current size is difficult to estimate, but is expected to rapidly grow as products and components continue to shrink. This is confirmed by the fact that two of the three big players, Carl Zeiss AG as well as Mitutoyo Corp. are developing µCMM systems such as the F25 (Carl Zeiss AG) and the UMAP103 (Mitutoyo Corp.).

According to [26] the worldwide revenue created by the micrometrology equipment market in 2006 was $726 million with a growth rate of about 10% (the forecast for 2010 is $1,030 million). At 83% of the market share, most of this micrometrology equipment goes to noncontact measurement systems; the contact dimensional micrometrology market, which includes µCMM, holds 17% of the market share and is estimated to reach about $175 million in 2010.

1.3.3 Micromechanical Material Testing Market [27]

According to [27] the worldwide revenue created by the entire mechanical test equipment

market in 2007 was $660 million with a growth rate of about 3% (the forecast for 2010 was $728 million). The market is segmented into universal testing machines (56.3%), servohydraulic testing machines for fatique testing (23.5%), hardness test equipment (12.1%) and impact test equipment (8.1%). Universal testing machines are mechanical testing equipment used to subject a material sample or structure to either tension or compression for the purposes of experimentally determining its mechanical properties. Servohydraulic testing machines are used for dynamic or fatigue testing. Hardness test machines are used to determine the resistance of the material to plastic deformation, usually by indentation, defined as material hardness. Impact test equipment is used to determine the impact toughness of a material by measuring the energy required to break a specimen by a hammer.

To determine the percentage of each of these sectors related to measurement in the microscale, the hardness testing market is used as an example, for which the subsegment microhardness testing (also referred to as nanoindentation) is estimated by [27] at 16.5%. Assuming a similar percentage for the other two segments relevant to micromechanical testing, universal testing machines and servohydraulic testing machines, the entire micromaterial testing market is estimated to create a revenue of $120 million in 2010.

1.3.4 Summary

The entire market for micromechanical and dimensional metrology is estimated to be in the order of $370 million at present, and is expected to grow rapidly with the increasing availability of sensing probes and the trend toward miniaturization.

Microforce-sensing probes are only one component in these multisensor systems performing these measurements. However, the technology for most other components in such a system, like micropositioners, high-resolution position feedback sensors or the appropriate software and control electronics, have already matured and are commercially available. Therefore, the current dominating factor for the limited availability of such systems is the limited availability of microforce-sensing probes and their proper characterization, which can be seen as the technology that opens the door to this new and fast growing market.

1.4 Objectives

The aim of this work lay in the development of novel metrological tools, systems and methodologies for micromechanical and dimensional measurements in the nanonewton to micronewton and nanometer to millimeter range. Currently, mature microscopy and

micropositioning techniques exist. Therefore this work focused on the development and characterization of novel microforce-sensing tools. The contributions of this Ph.D. thesis can be divided into the three following areas:

1.4.1 Microforce-Sensing Tools

Material scientists, biologists or engineers in need of sensors to measure forces in the nanonewton range were so far limited to cantilever-type sensors, such as the AFM or the use of elastic structures [9] whose deflection is measured in a high-resolution microscope, such as an SEM. Thus one of the goals of this thesis was to develop a new generation of integrated, batch-fabricated microforce-sensing probes that can measure force in the nanonewton to micronewton range in three-dimensional space.

In a second step these microforce-sensing probes will be integrated into a complete micromechanical measurement system on a chip – composing of actuators, a force sensor and displacement sensors – greatly reducing the size, cost and versatility of such a system.

1.4.2 Calibration and Uncertainty Analysis Methodology

The calibration of nanonewton to micronewton forces is difficult for many reasons, such as the unavailability of standardized calibration procedures or the unavailability of an SI-traceable reference standard, such as miniature weights. The smallest available SI-traceable mass artifact in the market is 1 mg, which corresponds to approximately 10 μN. Typically microforce sensors, such as AFMs, are calibrated based on a model of the sensor, with the disadvantage of having an unknown accuracy, since the results are not traceable back to SI-units. One main goal of this thesis was thus to enable traceable microforce sensor calibration. And by implementing the most recent advancements in multivariate uncertainty analysis, the uncertainties in the characteristic parameters of the sensors could be calculated. This methodology should create the basis for the utilization of microforce-sensing probes to perform SI-traceable force measurements in the nanonewton to micronewton force range and the calculation of their measurement uncertainty.

1.4.3 System Integration

Traceable microforce-sensing probes are only one of the components necessary for micromechanical material testing. Typical systems additionally utilize micropositioners with position feedback and a visualization system, such as a camera or a microscope enabling the alignment of the sensor and sample. Manual measurements and the accurate positioning of the sensor are complex and time-consuming, and incorporate a great risk of damaging the fragile

microforce-sensing probes or the sample. Therefore a fully automated micromechanical and microcoordinate measuring machine was developed, enabling automated measurements, from the initial sensor alignment to the actual dimensional or mechanical measurements. Besides improving the repeatability of the results, automation will facilitate the measurement of large amounts of data allowing for a statistical treatment of the results.

1.5 Organization

This report is a summary of the research performed within the scope of this Ph.D. Chapter 2 starts with an overview and comparison of different microforce-sensing technologies and the selection of the most appropriate approach for the measurement of forces in the micronewton to nanonewton range followed by the presentation of the design and fabrication of multiple novel microforce-sensing tools. In Chapter 3, after an overview of the current research challenges in the field of small-force metrology, the methodology for traceable calibration of single as well as multi-axis microforce-sensing probes and the calculation of their measurement uncertainties is shown. The system necessary to perform micromechanical and dimensional measurements in the microworld is presented in Chapter 4, followed by the demonstration of its capabilities in a variety of applications in Chapter 5. To conclude this thesis a summary and listing of the most important contributions made throughout the course of this work is given in Chapter 6.

2 Microforce-Sensing Probes

The limiting factor for the development of standardized micromechanical testing systems or microcoordinate measuring machines (μCMM) is the unavailability of microforce-sensing probes that can measure forces down to the nanonewton level along multiple axes. In this chapter, after an overview of the most relevant sensing principles, the design and fabrication of novel microforce-sensing probes as well as a complete measurement system on a chip is described.

2.1 Microforce-Sensing Technologies

A microforce-sensing probe is a transducer that converts a small applied force to an electrical signal. Different approaches and sensing technologies for the development of microforce sensors, measuring forces in the micronewton to nanonewton range, have been pursued. These range from large-scale machines such as the electrostatic force balance (EFB) developed by the National Institute of Standards and Technology (NIST) shown in Fig. 3(a) and (b), to microscopic sensors developed by Physikalisch-Technische Bundesanstalt (PTB) shown in Fig. 3(c), which was fabricated using the MEMS technology.

Depending on the requirements of the application for which the sensor is developed, such as the force range or whether static of dynamic forces need to be measured, the appropriate

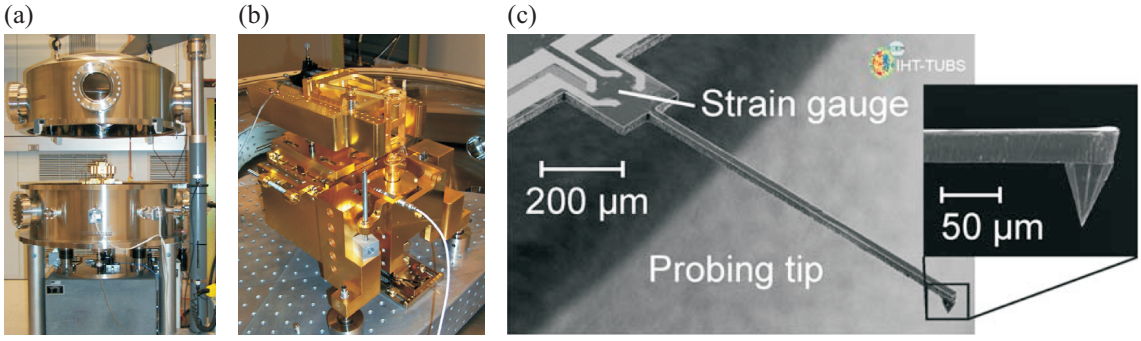

Fig. 3: (a) and (b) Electrostatic force balance (EFB) developed by NIST [31], (c) Piezoresistive microforce-sensing cantilever developed by (PTB) [32].

approach and sensing technology needs to be chosen. For the micromechanical testing of samples with micrometer characteristic dimensions, such as individual cells, MEMS-based mechanisms or biological fibers, the measurement of quasi-static forces (<1 kHz) in the micronewton to nanonewton range is required. The sensor needs to be compatible with different environments, such as air, liquid and vacuum. And to enable the integration into a measurement system, the sensor needs to be compact in size and light in weight.

For the development of miniature sensors to measure forces in the micronewton to nanonetwon range four commonly used technologies exist: piezoresistive, piezoelectric, capacitive and optical-based force sensing. More exotic principles such as magnetic-based sensing [33] or tunneling microforce sensing [34] are presented in literature, but are currently not mature enough for the development of reliable sensors. A short overview of the four main sensing technologies, as well as the selection of the most suitable approach for micromechanical measurements, is given.

A. Piezoresistive Force Sensing: A force applied to a semiconducting material such as silicon (SI), germanium (Ge) or gallium arsenide (GaAs) will result in a modulation of the electrical resistance. The modulation is a result of two effects: the geometry effect and the piezoresistive effect. The geometry effect refers to the change in resistance due to the change in the material's geometry as it gets deformed by the applied force. The piezoresistive effect refers to the variation of the specific resistance of a material induced by the applied stress, which for semiconducting material is the dominating cause of resistance change [35]. Piezoresistive sensing allows for the highest level of miniaturization (among the four discussed sensing technologies) but is limited to a relatively low sensitivity.

B. Piezoelectric Force Sensing: A piezoelectric material generates a voltage across the material when it is mechanically deformed. Piezoelectric materials are mostly crystalline materials such as gallium arsenide (GaAs) or zinc oxide (ZnO) in which the positive and negative charges are separated but symmetrically distributed. Therefore the material is overall electrically neutral. When a stress is applied, this symmetry is destroyed and the charge asymmetry generates a voltage. The typical deformations are in the nanometer range resulting in very stiff sensors with a high resonant frequency, enabling the measurement of forces at high frequencies. The disadvantage of piezoelectric sensing is the rapid decay of the electrical signal after the force is applied, rendering this technology unsuitable for the measurement of static forces.

C. Capacitive Force Sensing: Capacitive force sensors measure a force-induced displacement of an elastic element, such as a flexure, as a variation of the capacity between

attached capacitive electrodes. The capacity between two plates is given by (2.1), where A is the plate area, d is the distance between the plates and ε is the permittivity of the dielectric medium (in most cases air). Compared with piezoresistive-based sensors, capacitive sensors have the advantage of no hysteresis, better long-term stability and higher sensitivity [35].

$$C = \varepsilon \cdot \frac{A}{d} \tag{2.1}$$

D. Optical Force Sensing: The very-well known optical beam deflection technique to measure the deformation of a cantilever is the principle employed by AFM. This is the most commonly used microforce sensor and has demonstrated its potential in large variety of applications. It offers very high sensitivity and resolutions. Other optical-based microforce sensors that are, e.g., based on optical encoders or optical grids exist; however, all these sensors have the disadvantage of being relatively large, making a system integration in most cases impossible.

Each of the four force-sensing technologies has advantages and disadvantages. For the mechanical characterization of microscopic samples, forces at low frequencies (<1 kHz) need to be measured. The sensor must be compact to enable integration into an automated measurement system. Additionally it should be stable, highly sensitive to its primary input and insensitive to variations in environmental conditions. This leaves either piezoresistive or capacitive force sensing as a possible option. The superior characteristics in terms of stability and hysteresis [35] make capacitive force sensing the most suited technology for micromechanical material testing systems.

2.2 Capacitive Microforce Sensing

For the utilization as a reference-force sensor, a macroscale microforce sensor based on capacitive sensing has been developed, as shown in Fig. 4. Due to its large size, it is not as fragile as the microfabricated sensors presented later in this thesis, allowing it to be calibrated through the application of reference weights and utilized as the transfer standard for the calibration of microfabricated sensors as presented in Chapter 3.

The working principle of the sensor is schematically shown in Fig. 4. The sensor consists of a conductive cantilever (single crystalline silicon with length; l = 40 mm, width w = 6 mm, thickness t = 0.2 mm), clamped between two electrodes (10 mm by 6 mm) with an initial

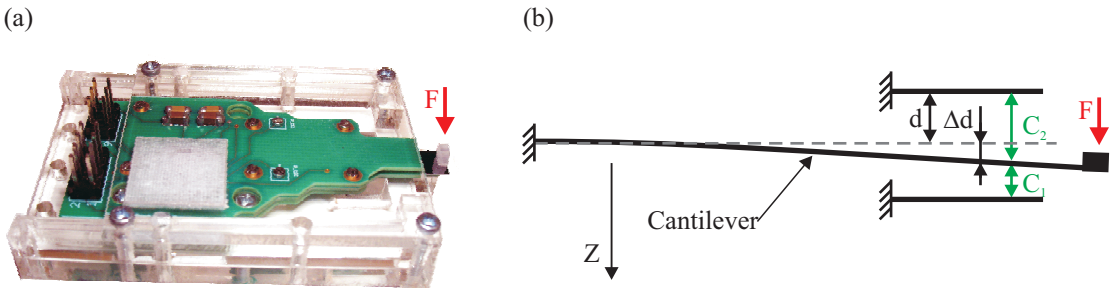

Fig. 4: (a) Photograph and (b) schematic of a single-axis cantilever-based capacitive microforce sensor.

separation of 250 µm from each of the electrodes. A force applied to the cantilever's end results in a change of the gaps between the cantilever and the electrodes, which can be measured by a change in capacitance. If the displacement of the cantilever's end is small compared with its length, the displacement is linerly proportional to the applied force.

This transversal capacitive displacement-sensing method benefits from a great sensitivity to displacements, but lacks in linearity when measuring only one of the capacitance (C_1 or C_2). However, by measuring the two capacitive changes of C_1 and C_2 (with opposite signs) differentially, the relationship is linearized as shown in Fig. 5 and equations (2.2) to (2.4), where C is the capacitance, $\varepsilon = 8.85 \cdot 10^{-12}$ $C^2/(Nm^2)$ is the permittivity of air, d is the initial gap between the capacitor electrodes, Δd is the change of this gap (induced by the applied force) and A is the overlapping area of the capacitor electrodes. For $x = \Delta d/d$ and $|x| < 1$ the Maclaurin series of $(1-x)^{-1}$ (infinite geometric series) can be used to simplify (2.2) to (2.4).

$$C_1 - C_2 = \varepsilon \cdot A \cdot \left(\frac{1}{d - \Delta d} - \frac{1}{d + \Delta d} \right) \tag{2.2}$$

$$\frac{1}{1-x} = \sum_{n=0}^{\infty} x^n \approx 1 + x + x^2 \tag{2.3}$$

$$C_1 - C_2 = \frac{\varepsilon \cdot A}{d} \cdot \left(\frac{1}{1 - \frac{\Delta d}{d}} - \frac{1}{1 + \frac{\Delta d}{d}} \right) \approx \frac{\varepsilon \cdot A}{d} \cdot \left(\frac{2 \cdot \Delta d}{d} \right) = \varepsilon \cdot A \cdot \frac{2 \cdot \Delta d}{d^2} \tag{2.4}$$

The relationship between the displacement and the resulting differential capacitive change can only be approximated by a linear relationship over a certain percentage of the initial gap (Fig. 5). With the increasing displacement range, the non-linearity in the sensor's characteristics will increase. Therefore the stiffness of the cantilever is designed such that the maximum force to be

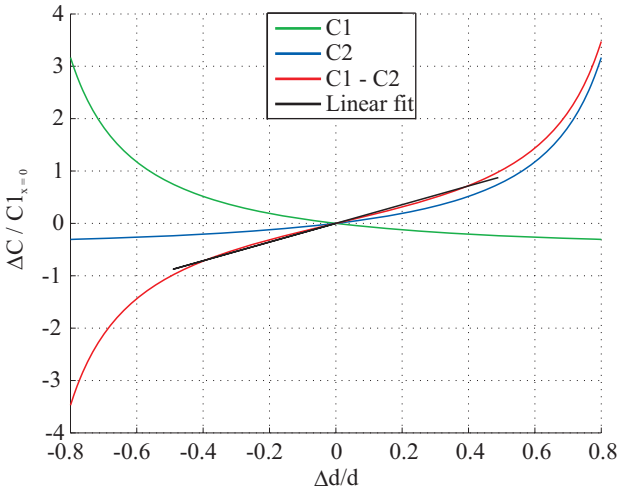

Fig. 5: Relationship between the relative displacement and the relative capacitive change in a differential capacitive microforce sensor as shown in Fig. 4.

measured causes the cantilever to deflect only half the initial electrode gap. The force sensor is designed to measure forces up to 4 mN. The differential capacities between the upper and lower electrodes to the cantilever are converted to a voltage using a commercial capacity-to-voltage converter (MS3110, Irvine Sensors Inc. [36]). The resulting characteristics, such as the calibration results of the microforce sensor, are presented in Section 3.4.

2.3 MEMS Technology for Microfabricated Force-Sensing Probes

With the advancement of the MEMS technology, the development of miniature microforce sensors has become possible, enabling a monolithic integration of the movable body, the flexure, and the capacitive electrode into a single chip. Besides making the sensors smaller and therefore simplifying the integration into a measurement system, miniaturized force sensors benefit from better performance, such as higher sensitivity. Scaling laws can be used to understand the influence of miniaturization on the behavior of a system [37]. Considering a microforce sensor, which is based on the deflection of a cantilever with a rectangular cross section, the spring constant k (for a deflection in the z-direction as shown in Fig. 4) is given by (2.5), where E is the Young's modulus, t is the thickness, w is the width and l is the length of the cantilever.

$$k = \frac{E \cdot t^3 \cdot w}{4 \cdot l^3} \tag{2.5}$$

Defining the typical linear dimension s, it can be seen that l, t, w and the spring constant k scale

linearly with s.

$$l, t, w, k \sim s \tag{2.6}$$

But the inertial force of such a sensor (2.7) is proportional to its mass m and therefore scales with s^3. Thus a microforce sensor's sensitivity to vibrations (with an acceleration given by a) decreases as the sensor's dimensions decreases.

$$F_a = m \cdot a \sim s^3 \tag{2.7}$$

When replacing the acceleration by the gravitational acceleration g, it can be seen that the smaller the sensor, the less influence its orientation (horizontal or vertical) has on it. Analysis of the effect of miniaturization on the mechanical resonance frequency f_R described by (2.8) demonstrates that the smaller the sensor, the higher the mechanical resonance frequency, and therefore measurement of forces at higher frequencies becomes possible.

$$f_R = \frac{1}{2\pi} \cdot \sqrt{\frac{k}{m}} \sim s^{-1} \tag{2.8}$$

As mentioned earlier, miniaturization also has a positive effect on the sensitivity of a sensor. Considering a capacitive-based force sensor with differential capacitive readout, the sensitivity of the output signal is given by (2.9), where F is the applied force, V_{Out} the sensor's output voltage signal, A the area of the capacitive electrodes and d the gap between these electrodes. (Details about the derivation of (2.9) are given in Section 2.4). As the sensor gets smaller, its sensitivity S gets higher, resulting in the ability to measure smaller forces.

$$S = \frac{\partial V_{Out}}{\partial F} \sim \frac{A}{d^2 \cdot k} \sim s^{-1} \tag{2.9}$$

Therefore, by reducing the size of a microforce sensor (based on differential capacitive sensing), the measurement of smaller forces at higher frequencies with reduced sensitivity to shock and vibrations becomes possible.

For the fabrication of these sensors with microscopic dimensions, traditional fabrication techniques like milling, drilling and sawing cannot be used. Microfabrication based on lithographic processes enables the fabrication of structures with features down to the micrometer level. To facilitate the understanding of the design of the microforce-sensing probes presented in the next sections, a short introduction to the most relevant aspects of microfabrication are presented here. More information about the detailed process-flow used for the fabrication of the different devices can be found in Section 2.7.

MEMS are small integrated devices or systems that combine electrical and mechanical components on a common substrate to form devices such as sensors and actuators. The microfabrication technology was originally borrowed from the integrated circuit (IC) industry, the basic fabrication processes such as, e.g., photolithography, evaporation, ion implantation and many more were adopted. Driven by the field of MEMS, a variety of new microfabrication processes and materials are being developed, which enable new kinds of miniaturized sensors and actuators. With a lithographic process, batch fabrication of a large number of devices in parallel becomes possible, greatly reducing the cost of such a sensor while (in some cases) enhancing the performance.

Photolithography is the most important process, since this allows the fabrication of structures with microscopic dimensions. A schematic of this process is shown in Fig. 6. It starts with a substrate material (a), e.g., a single crystalline silicon wafer, onto which a photosensitive polymer (photoresist) is applied by, e.g., spin coating (b). In the next step UV light is shined through a mask made from a transparent support material, e.g., glass, with the structure on it made from opaque material (c). The regions of the photoresist that are exposed to light get chemically altered, so that they can subsequently be removed (in the case of positive photo resist) using a chemical (developer) (d). In the following step, this photoresist mask can be used to either deposit a material (e) or selectively etch the underlying material. As the last step in this process, the photoresist is selectively removed leaving a micromachined structure (g) or (h).

A large number of different substrates and deposition materials can be used to create different

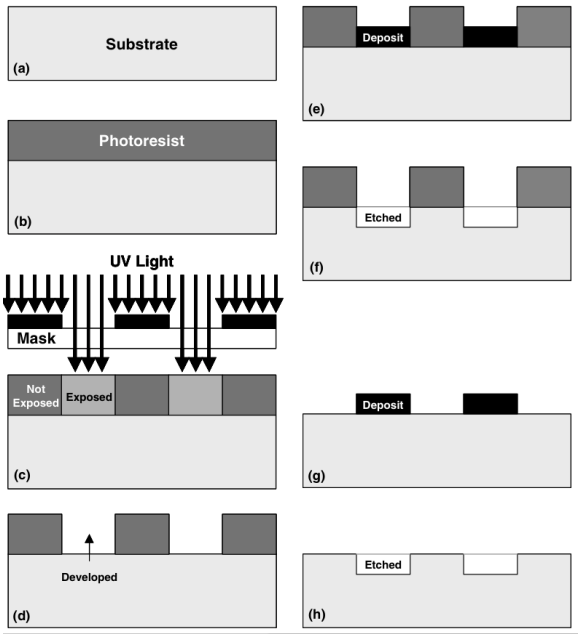

Fig. 6: Schematic of a photolithographic process [38].

kind of structures. A general differentiation between surface and bulk micromachining can be made. In the case of surface-micromachining the structure of the devices is fabricated from the relatively thin (~1 – 100 μm) deposited materials, whereas in the case of bulk micromachining the structures are etched out of the bulk of the substrate. The benefit of bulk micromachining is that it is possible to create high aspect ratio structures and make use of the superior mechanical characteristics of the single crystalline substrate material. The microforce-sensing probes are etched out of the bulk of single crystalline silicon wafers using only a combination of photolithography and dry-etching steps.

Dry etching, also referred to as ion etching, is the etching of a material by exposing it to an ion bombardment. Two different types of dry etching principles are used for the fabrication of the sensors reactive-ion etching (RIE) and deep reactive-ion etching (DRIE).

RIE is used to etch the silicon dioxide (SiO_2) layers. Plasma is generated in a chamber by applying a strong radio frequency (RF) field to the wafer. The oscillating electric field ionizes the argon gas molecules in the chamber creating ions and radicals. Due to the higher mobility of the electrons, they accumulate on the wafer substrate, negatively charging it, resulting in an electric field that accelerates the positively charged ions towards the wafer, where they transfer their kinetic energy onto the substrate, knocking out atoms; this process is called physical etching. At the same time, the radicals drift to the surface of the wafer, where they react with the material, resulting in an additional chemical etching component. Due to the directional impact, mainly of the ions, anisotropic, vertical etching into the material can be achieved.

DRIE is a special RIE process that is very important for bulk micromachining. It is used for the anisotropic etching of bulk materials, e.g., silicon, to create high aspect ratio structures with vertical sidewalls. The advanced silicon etch (ASE) process developed by Surface Technology Systems Plc. (STS) has been used for the fabrication of the microforce sensors. With ASE, the plasma is generated by a coil in a separate chamber and is called inductively coupled plasma (ICP), which enables the decoupling of the plasma generation and ion acceleration from each other, enabling a higher ion concentration. The ASE consists of two steps repeated iteratively

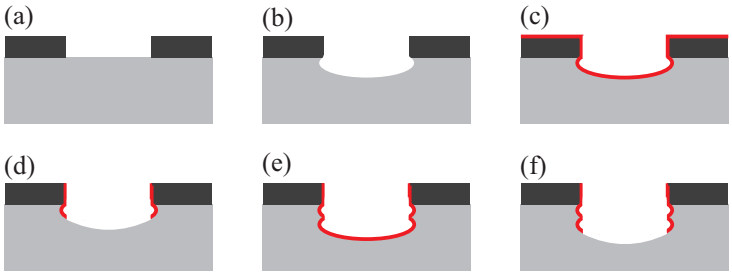

Fig. 7: Schematic of the advanced silicon etch (ASE) process developed by Surface Technology Systems Plc.(STS).

and is depicted in Fig. 7. After the argon plasma is ignited, the chamber is flooded with SF_6 gas. The SF_6 molecules collide with the ions from the plasma and are cracked. The free fluorine radicals react with the exposed silicon of the substrate material in an isotropic etching (b), onto which an anisotropic physical etching caused by the argon ions is superimposed. After a certain time, the residues are pumped out and the chamber is flooded with C_4F_8, which forms a Teflon-like passivation layer on the entire surface of the substrate (c). After a certain time, the residues are pumped out again and SF_6 is introduced to the chamber for the next etching step. Anisotropic vertical etching into the substrate is achieved, since the passivation layer is mainly removed by the physical component in the etch process, which is directional and only attacks the horizontal areas of the substrate (d). Therefore, the passivation layer on the sidewalls of the structures is not removed and protects them from the chemical etching as shown in Fig. 7. The combination of isotropic etching and passivation repeated iteratively can be used for the fabrication of high aspect ratio structures, such as the parallel-plate capacitor configurations or the high aspect ratio flexures.

The fabrication process of the microforce-sensing probes is based on silicon-on-insulator (SOI) substrates, which refers to the use of a layered silicon-insulator-silicon substrate. There are two benefits to having the insulating oxide between two silicon layers. First it can be used as an etch stop during fabrication, and second, it makes it possible to use one of the two silicon layers, called the handle layer, to form an outer frame for the sensor. The other layer, the devices layer, is used to form the active elements of the device, such as the flexures, movable bodies and capacitive electrodes. Due to the isolating silicon oxide layer, all these active components in the device layer are held together, but are electrically isolated from each other.

As previously mentioned, the smaller the sensor, the higher its sensitivity, and the smaller the forces that can be measured. How small the sensor can be made is, however, limited by the microfabrication equipment. Critical for miniaturizing the sensor are the features of the active elements, such as the flexures, and the gaps between the capacitive electrodes. Given by the mask aligner (MA/BA6 SUSS MicroTec AG), a minimum feature size of 1 μm can be achieved. And given by the dry etching equipment (ICP, STS), a maximum aspect ratio of 10 has been proven to result in reliable etching over an etch depth of at least 50 μm. As the focus of this thesis was not to optimize the microfabrication process parameters a minimum feature size of 5 μm with a device layer thickness of 50 μm was chosen to ensure reliable fabrication. More details about the process flow used for the different sensing tools can be found in Section 2.7.

2.4 Single-Axis MEMS-Based Capacitive Microforce-Sensing Probes

A variety of miniature, MEMS-based capacitive microforce-sensing probes, such as the single-axis sensor [11] shown in Fig. 8(a), have been developed. To better understand the design of the more complex devices and systems presented in this work, an introduction to the key aspects of these MEMS-based capacitive microforce-sensing probes is given here.

The working principle, schematically shown in Fig. 8, is similar to the microforce sensor presented in Section 2.2. The sensor consists of a movable body with an attached probe suspended by flexures within an outer frame. A force applied to the probe in the x-direction results in a relative motion of the body and the outer frame, which can be measured by attached capacitive electrodes as a change in capacitance. The sensor is microfabricated out of an SOI wafer. The active elements, such as the movable body, the flexures and the capacitive electrodes, are etched out of the thin device layer, and the relatively thick handle layer is used for the fabrication of the outer frame, mechanically holding all these components together. Due to the symmetric design of this sensor, parallel motion of the movable body as it is deflected can be achieved, making this design superior to most of the cantilever-type sensors.

To increase the sensitivity of the sensor given by (2.13), not only should the sensor flexures have very low stiffness, but the gaps between the capacitive electrodes also should be minimized and their overlapping area maximized. Therefore, the minimum reliable gap width of 5 μm (Section 2.3) is used. To increase the overlapping area of the sensing capacitors, an array with n_C capacitive electrode pairs is attached to the sensor. A relative motion of the movable body will cause the gaps between these parallel plates to change, resulting in a change in capacitance. As demonstrated in Section 2.2 the capacity-force relationship is linearized by

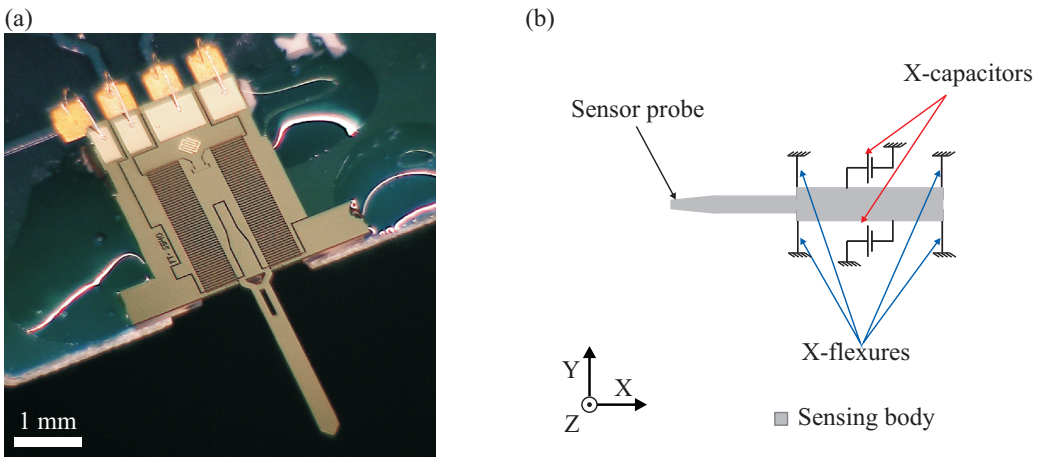

Fig. 8: (a) Photograph and (b) schematic of a single-axis MEMS-based capacitive microforce-sensing probe (the immovable outer frame is not shown).

measuring two capacitive changes with opposite signs differentially using a commercially available capacitance-to-voltage converter (MS3110, Irvine Sensors Inc.). For simplicity this relationship is described by (2.10) using the constant C_{CVC} and offset $Offset_{CVC}$. Details about the capacitance-to-voltage converters used for the different force-sensing tools are presented in Section 2.8.

$$V_{Out} = C_{CVC} \cdot (C_1 - C_2) + Offset_{CVC} \tag{2.10}$$

The theoretical transfer function (2.12) of the single-axis microforce sensor, describing the relationship between the output voltage of the sensor V_{Out} and the applied force F_{X} (in x), can be found using (2.4), C_{CVC} and $Offset_{CVC}$ and the stiffness of the sensor in the x-direction given by (2.11), where E_F is the Young's modulus, t_F the thickness, w_F the width and l_F the length of each of the four flexures. Additionally d_{c}, the gap between the capacitive electrodes, A_{c}, the overlapping area of the capacitive electrodes and ε_{c}, the permittivity of air, are needed.

$$k_X = 4 \cdot \frac{E_F \cdot t_F \cdot {w_F}^3}{{l_F}^3} \tag{2.11}$$

$$V_{Out} = C_{CVC} \cdot \frac{\varepsilon_c \cdot A_c \cdot {l_F}^3}{2 \cdot {d_c}^2 \cdot E_F \cdot t_F \cdot {w_F}^3} \cdot F_x + Offset_{CVC} \tag{2.12}$$

The sensitivity S_{x} of the microforce sensor to a force in the x-direction can be calculated as the derivative of the transfer function with respect to the applied force in x.

$$S_X = \frac{\partial V_{Out}}{\partial F_X} = C_{CVC} \cdot \frac{\varepsilon_c \cdot A_c \cdot {l_F}^3}{2 \cdot {d_c}^2 \cdot E_F \cdot t_F \cdot {w_F}^3} \tag{2.13}$$

Besides the parallel motion of the movable body, this four-flexure configuration greatly reduces the cross sensitivity to off-axis forces in the sensor plane, since forces in the y-direction will result in negligible displacements of the movable body (compression/tension of the flexures). Due to the planer MEMS fabrication process, a similar configuration cannot be realized for off-axis out-of-plane forces in the z-direction. A force in the z-direction will result in a displacement of the sensing body out of the sensor plane. To reduce this cross sensitivity, the stiffness to out-of-plane forces is increased by realizing high aspect ratio flexures. This is achieved by maximize the flexure thickness t_F. A flexure with a width of 10 µm and a thickness of 50 µm will result in a stiffness of the movable sensing body that is 125 times greater for out-of-plane forces than that for in-plane forces ((2.14), (2.15)). To confirm the reduced sensitivity

Table 1: Design parameters of the single-axis MEMS-based capacitive microforce-sensing probe

l_F	Flexure length	540	µm
w_F	Flexure width	10	µm
t_C, t_F	Capacitive electrode thickness, flexure thickness	50	µm
F_S	Design force range (for half d_1 displacement)	±540	µN
l_C	Capacitive electrode overlapping plate length	500	µm
d_1, d_2	Capacitive electrode gap spacing widths*	5, 20	µm
n_C	Number of electrode pairs per capacitor C1 and C2	50	
C	Capacitance at the maximum force	5	pF

* The two capacitive gaps are shown in Fig. 18

to off-axis forces, the cross sensitivity is quantitatively measured and presented in Section 3.4.

$$k_Z \sim t_F^3 \tag{2.14}$$

$$k_X \sim t_F \tag{2.15}$$

A large number of different single-axis sensing probes with flexure lengths ranging form 200 to 3,000 µm have been realized. But due to the unavailability of traceable reference standards and methodologies for the calculation of their uncertainties; none of these sensors have been fully characterized, making the estimation of their quality and their measurement accuracy impossible. Therefore, within the course of the next chapter the characterization of one of these sensors with the design parameters given in Table 1 is presented.

2.5 Multi-Axis MEMS-Based Capacitive Microforce-Sensing Probes

A force is a vector in three-dimensional space; therefore using a single-axis microforce-sensing probe is only justified to measure its magnitude when its sensitive direction is perfectly aligned with the direction of the force vector under investigation. In the case of microscopic samples, this alignment is often challenging, and can lead to faulty measurements. Different approaches for the simultaneous measurement of the complete force vector with its three components have been made based on either capacitive [23] or piezoresistive [4] sensing. However, none of these approaches resulted in the ability to measure submicronewton forces and involve either complex fabrication processes or the need for microassembly, both rendering large-scale fabrication of these devices impossible.

In a first step, the development of a two-axis (in-plane) microforce-sensing probe is presented, before introducing the approach for the simultaneous in- and out-of-plane full three-axis

microforce sensing. The basic working principle of a multi-axis capacitive microforce sensor is similar to the single-axis case. The sensor consists of a movable body suspended by flexures within an outer frame. A force applied to the probe results in a relative motion of the body and the frame, which can be measured by capacitive electrodes as a change in capacitance. By designing the flexures in such a way that they allow the body to move in multiple directions, and by using several of these capacitive displacement sensors, forces/displacements in multiple directions can be measured. For multi-axis microforce-sensing probes, it cannot entirely be avoided to induce rotational motion for the measurement of the off-axis force components. Exceptions, such as those shown in [39], where the force is applied in the center of the movable body and not onto a protruding sensing probe, do not qualify as microforce-sensing probes.

Fig. 9 shows the design of a two-axis microforce-sensing probe. The stiffness of the flexures in the x- and y-directions is used to design the force-sensing range along its two sensitive directions. The force range has been designed to be up to ±630 µN along both axes (correlating to displacement of half the capacitive gap width). To ensure equal sensitivity of the sensor along both axes, it has been modeled in a finite element model (FEM) environment (ANSYS Inc.). Using this model in an optimization loop, the dimensions of the flexure can be found that will result in the desired sensitivity along both directions. Table 2 presents the design parameters of the two-axis microforce-sensing probes.

In the case of the single-axis and two-axis sensing probes, only forces in the sensor plane are measured using a transversal capacitive electrode configuration. Measuring forces/displacements out of the sensor plane is more challenging. In [23] out-of-plane displacements are measured by bonding an additional silicon layer onto the substrate, thereby

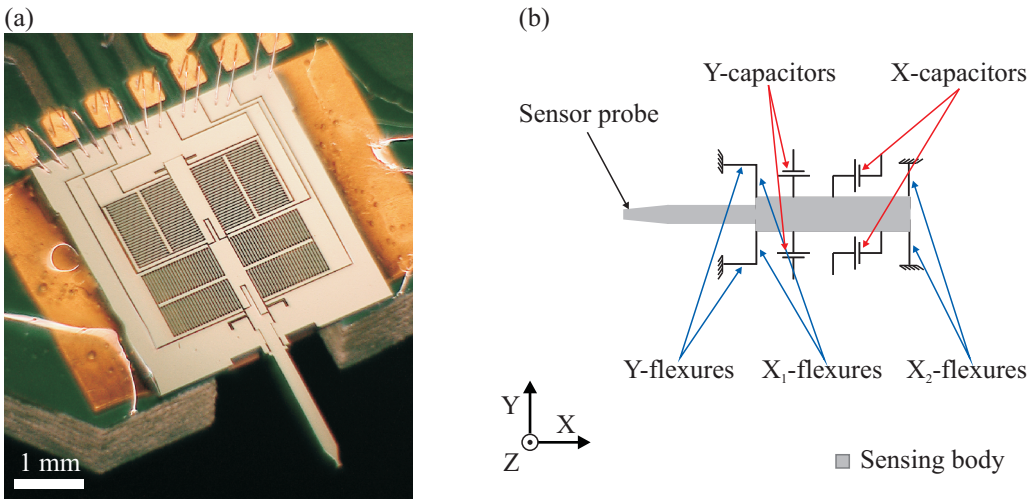

Fig. 9: (a) Photograph and (b) schematic of a two-axis MEMS-based capacitive microforce-sensing probe (the immovable outer frame is not shown).

Table 2: Design parameters of the two-axis MEMS-based capacitive microforce-sensing probe

$l_F x_1$	X_1-flexure length	300	µm
$l_F x_2$	X_2-flexure length	200	µm
$l_F y$	Y-flexure length	130	µm
w_F	Flexure width	5	µm
t_C, t_F	Capacitive electrode thickness, flexure thickness	50	µm
Fs	Designed force range (x & y) (for half d_1 displacement)	±630	µN
l_C	Capacitive electrode overlapping plate length	470	µm
d_1, d_2	Capacitive electrode gap spacing widths*	5, 20	µm
n_C	Number of electrode pairs per capacitor C_1 and C_2	50	

* The two capacitive gaps are shown in Fig. 18

enabling an out-of-plane parallel-plate capacitor configuration. Although the transversal out-of-plane displacement sensing achieved a high sensitivity, the high fabricational complexity resulted in a low yield and expensive fabrication. Therefore, a new approach based on lateral sensing was chosen to measure the out-of-plane forces. In this case, the variation of the capacitance is induced by a change of the vertical overlapping area of the parallel plates. The disadvantage of this approach is that it cannot be distinguished between positive or negative forces in the z-direction, since in both cases the overlapping area of the capacitive electrodes gets smaller, and therefore the capacitance gets smaller as well.

To overcome this problem, two layered capacitive electrodes are used; these are schematically shown in Fig. 10. This electrode configuration can be achieved by fabricating the sensor out of a double SOI wafer. The relatively thick silicon handle layer (H) forms the outer frame of the sensor, and the two thin silicon device layers (D) form the active elements and the movable body. All the layers are electrically isolated by an SiO_2 layer. The additional device layer enables the distinction between positive and negative forces in the z-direction. The differential capacitance ($C_1 - C_2$) is negative when the inner sensing body moves up ($z > 0$) and positive when it moves down ($z < 0$). Fig. 11 shows the schematic of the three-axis sensing probe utilizing this multilayer electrode configuration. Due to the unequal sensitivity of transversal in-plane sensing compared with lateral out-of-plane sensing, these degrees of freedom are divided

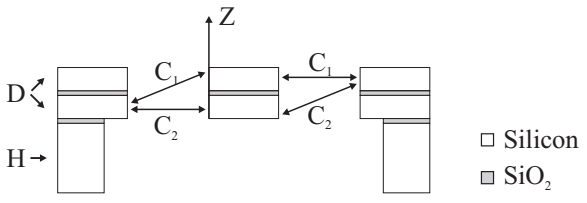

Fig. 10: Cross section of the sensing capacitor, visualizing the bidirectional out-of-plane sensing principle.

into two sensing bodies suspended within each other. The outer body measures displacements in the x- and y-directions (and, therefore, forces relative to them), while the inner sensing body measures forces/displacements relative to the outer sensing body in the z-direction. The stiffness of the flexures is used to design the force-sensing range. The sensor is designed to measure forces of up to ±200 μN in the x-, y- and z-directions. Multiple sensor configurations (position and geometry of flexures, capacitors and movable bodies) have been analytically compared. Besides the sensitivity criterion for each axis, the most important factor in multi-axis sensor design is the decomposability of the force components. To ensure a minimum cross coupling between the different axes, each capacitor pair is dedicated to a single force component and placed such that the main contribution to an output signal can be directly related to the force in the corresponding direction. Therefore, the x-capacitor is mainly sensitive to forces in the x-direction, the y-capacitor to forces in the y-direction and the z-capacitor to forces in the z-direction. Similar considerations have been made for the flexures, such that by changing the dimensions of the flexures the mechanical stiffness of the sensor can be independently adjusted for each axis.

Fig. 12 shows the mechanical response of the sensor to each force component. A force applied in the x-direction will result in a parallel movement of the sensing bodies and, therefore, only produces a change in the x-capacitance. Since one of the parallel-plate capacitor electrodes is always longer than the other, a parallel relative movement (as is the case for the y-capacitor) will not result in a change of the overlapping area and thus will not affect their capacitance, as

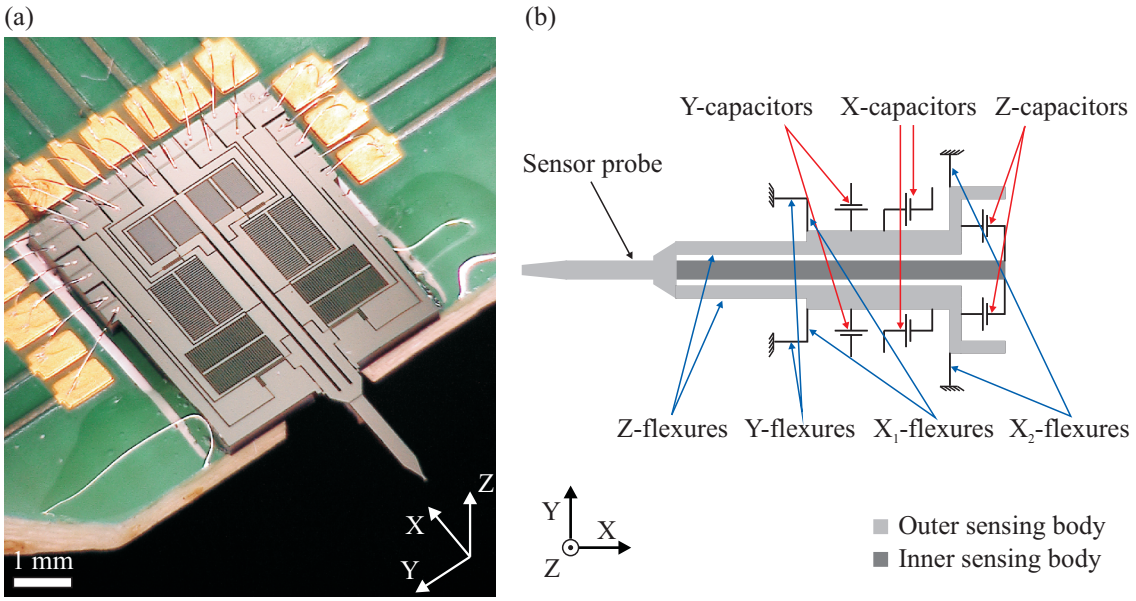

Fig. 11: (a) Photograph and (b) schematic of a three-axis MEMS-based capacitive microforce-sensing probe (the immovable outer frame is not shown).

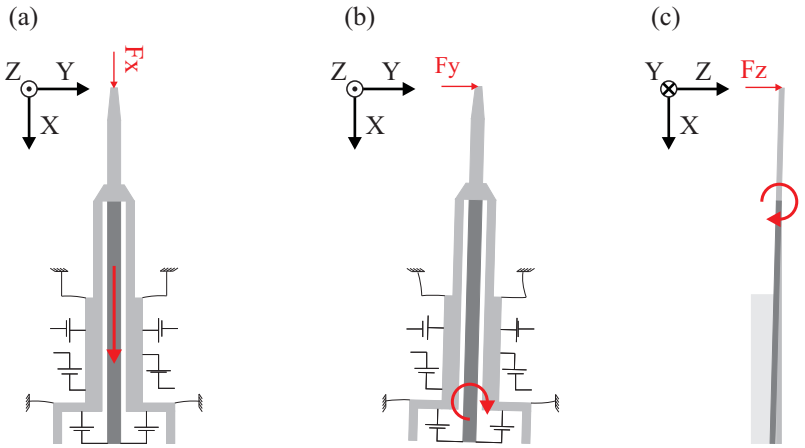

Fig. 12: Mechanical response of the three-axis MEMS-based capacitive microforce-sensing probe to an applied force in: (a) the x-direction, (b) the y-direction and (c) the z-direction.

shown in Fig. 12(a).

Forces in the y-direction result in a rotation of the two sensing bodies relative to the outer frame. To ensure high sensitivity to these rotations the y-capacitor pair is placed as far from the point of rotation as possible, as shown in Fig. 12(b). The absolute capacitances in the x-capacitors will change due to a force in y, but both of them will have equal signs, resulting in no change in the differential capacitance.

Due to the lower sensitivity of lateral sensing, forces in the z-direction need to produce a much larger deflection of the capacitor electrodes than forces in the x- or y-directions. Therefore, an amplification lever is integrated, as shown in Fig. 12(c), and the z-capacitor is

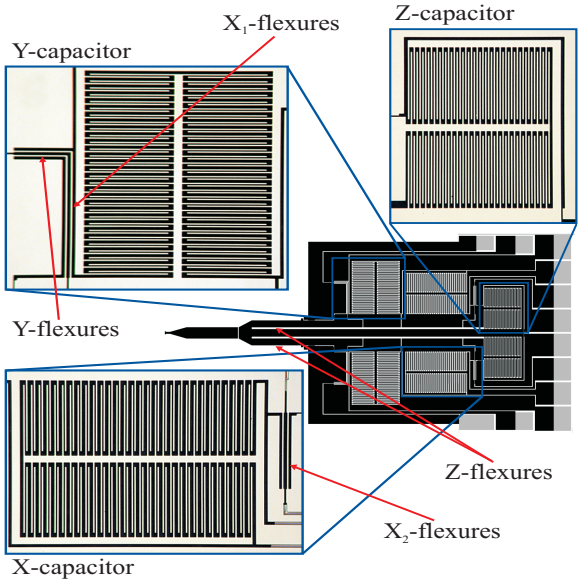

Fig. 13: Close-up views of the three-axis MEMS-based capacitive microforce-sensing probe.

placed as far from the sensor tip as possible to maximize its leverage effect. Using this method, the z-flexure stiffness does not need to be significantly reduced. Forces in the z-direction will only result in a signal in the z-capacitors, since due to the aspect ratio of the flexures in the x- and y-directions (which are much thicker than they are wide), the out-of-plane motion can be neglected. These design considerations for separating the three force components into the three sensing capacitor pairs are experimentally validated and presented in Section 3.8.

An FEM (ANSYS Inc.) has been created to calculate the quantitative mechanical response of the sensor to an applied force at its probe. This enables the optimization of the flexure geometry for a certain target sensitivity along the three axes. The deflections at the position of each capacitor and the corresponding differential signal change were used as the design criteria and the flexure dimensions as the design parameters. Using the FEM analysis in an optimization loop and starting with an initial estimate of the flexure dimensions, the difference from the target deformations in each capacitor and for each force direction were found. By scaling the flexure dimensions with these errors, the ideal flexure geometry could be found, which not only ensures the desired signal change at the target force in the corresponding capacitor pair, but also minimizes the signals in all the other capacitor pairs. The resulting flexures are shown in Fig. 13 and their dimensions in Table 3. Since all the capacitors need to have electrical contact to the outer frame, two flexures (A and B) at each point must be fabricated instead of one to produce the required electrical connections.

Table 3: Design parameters of the three-axis MEMS-based capacitive microforce-sensing probe

		A	B	
$l_F x_1$	X_1-flexure length	835	865	μm
$l_F x_2$	X_2-flexure length	537	537	μm
$l_F y$	Y-flexure length	314	344	μm
$l_F z$	Z-flexure length	1,900	1,900	μm
$w_F xy$	X,Y-flexure width	10	10	μm
$w_F z$	Z-flexure width	183	183	μm
t_F	Flexure thickness *	52	52	μm
Fs	Designed force range (x, y & z)		±200	μN
l_C	Capacitive electrode overlapping plate length		470	μm
$t_C xy$	X,Y-capacitive electrode thickness*		50	μm
$d_1 xy$, $d_2 xy$	X,Y-capacitive electrode gap spacing widths		7, 20	μm
$n_C xy$	Number of x,y-electrode pairs per capacitor C_1 and C_2		60	
$t_C xy$	Z-capacitive electrode thickness		25	μm
$d_1 z$, $d_2 z$	Z-capacitive electrode gap spacing widths		7, 7	μm
$n_C z$	Number of z-electrode pairs per capacitor C_1 and C_2		100	

* The active elements consist of two 25 μm thick silicon layers and one 2 μm thick SiO_2 layer

2.6 Monolithically Integrated MEMS-Based Microtensile Tester on a Chip

The microforce-sensing probes presented in the previous sections are only one component of a measurement system. Only the combination with micropositioners and position feedback sensors enable micromechanical or dimensional measurements. In this section, the combination of all the necessary components for a multi-axis microtensile-tester on a single chip are demonstrated, which enables the batch fabrication of such a complete system.

Tensile testers have been used by material scientists for decades to gather quantitative information on the mechanical properties of materials by stretching them while measuring the applied force. Increasing effort is being made to develop novel microtensile testers for the ever-smaller sample sizes being studied. With the advancement of MEMS technology, the development of novel electromechanical tools has become possible, enabling the integration of such systems into single measurement chips. The main components of a tensile tester chip are the displacement actuator, the force sensor and the position feedback sensor. These components enable the stretching of a sample while measuring its deformation and the applied force. For MEMS-based actuation, thermal actuators are most commonly used where high forces and small displacements are needed [40], [41]. Alternatively, electrostatic comb drive-based actuators are used where relatively low forces and large displacements are needed [42], [43]. For most microtensile testers, the deformation of the sample is visually observed through a high-resolution microscope, as shown in [40] – [42]. A different approach is demonstrated in [43], where the elongation of the sample is measured using a capacitive displacement sensor integrated into the actuator. For the measurement of the applied force, different approaches have also been used. In [40] a capacitive-based force sensor has been developed and in [41] and [43]

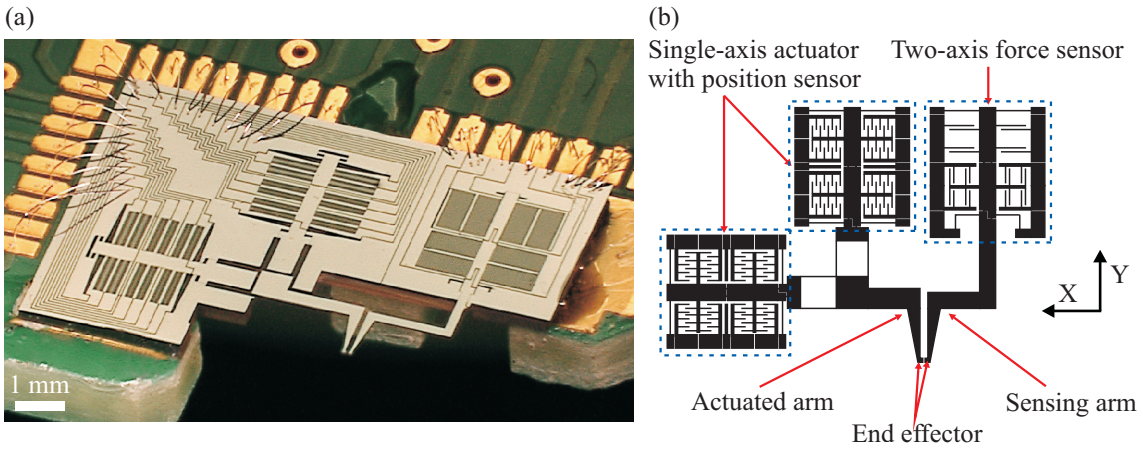

Fig. 14: (a) Photograph and (b) schematic of the monolithically integrated MEMS-based two-axis microtensile tester (the chip size is 7 mm by 10.8 mm).

the force has been calculated from the discrepancy between the expected and the measured displacement.

In this section the first fully integrated two-axis microtensile tester, shown in Fig. 14, is presented, allowing for compression, tensile testing, as well as shear testing of microscopic samples. It offers dedicated sensors for force and displacement measurements for each of its two axes as well as two independent actuators. This enables an optimal separation of the actuation and sensing elements, resulting in minimal cross sensitivity. Due to the complete integration of the tensile tester, visual feedback is not needed for the measurement of the sample deformation or the applied force. This full integration additionally allows for the tensile tester to be mounted on a micromanipulator as an end effector, greatly facilitating the alignment to the sample under investigation.

The microtensile tester can be subdivided as shown schematically in Fig. 14(b). The sample is measured between the tips of the two end effector arms. The right arm is connected to a two-axis capacitive microforce sensor as described in Section 2.5 with its characteristic design parameters presented in Table 2, allowing it to simultaneously measure forces and positions in the x- and y-directions. The left arm is connected to a platform suspended by flexures within two orthogonally attached electrostatic actuators. Both actuators can move along one axis and offer capacitive position feedback. Therefore, the platform can be actuated along two axes, and assuming a rigid body, the position of the end effector can be measured in both the x- and y-directions. To ensure a parallel rather than rotational movement, the platform is attached to the actuators by two parallel beams [44]. This is important to ensure linearity of the position feedback sensors. The schematic of the single-axis microactuator with position feedback sensor is shown in Fig. 15. Like the forces sensor, it is made up of a movable body suspended by flexures within an outer frame. In this case an electrostatic actuator and a capacitive displacement sensor are attached to the body. The actuating element is an array of parallel-plate electrodes (comb drive). For relatively large displacements of ±16 µm, a lateral movement

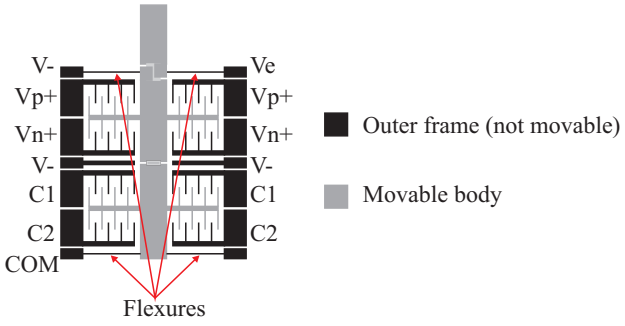

Fig. 15: Schematic of one single-axis electrostatic actuator with integrated capacitive position feedback sensor.

(rather than transversal) of the comb drive plates relative to each other is chosen. By applying a voltage difference between the central movable body (V-) and one of the outer comb drive electrodes (Vp+ or Vn+) the movable comb drive part gets pulled into the static one, resulting in a linear motion. The force F_{AC} acting on the central body as a function of the actuation voltage V_{AC} can be calculated by (2.16). Using the spring constant of the actuator flexures k_{AC} given by (2.17), the resulting displacement D_{AC} (2.18) can be found for each axis. To calculate the spring constant of the actuator, the spring constants of the four flexures in the linear actuator (described by the first term in (2.17)) and the two flexures of the platform (the second term) need to be taken into account.

$$F_{AC} = \frac{1}{2} \cdot {V_{AC}}^2 \cdot \varepsilon \cdot \frac{t}{d_{AC}} \cdot n_{AC} \tag{2.16}$$

$$k_{AC} = 4 \cdot \frac{E \cdot t \cdot {w_A}^3}{{l_{AC}}^3} + 2 \cdot \frac{E \cdot t \cdot {w_A}^3}{{l_{PF}}^3} \tag{2.17}$$

$$D_{AC} = \frac{F_{AC} - F_S}{k_{AC}} \tag{2.18}$$

The maximum designed deformation D_{AC} for the actuator is ±16 μm, at which it should still be possible to apply the maximum sensing force *Fs* of ±60 μN, to the sample (the sensing range has been electrically tuned, as described in Section 2.8, to use only a small percentage of the measurable displacement range, ensuring a higher linearity of the two-axis force sensor). Table

Table 4: Design parameters of the two-axis microtensile-tester's actuator and position feedback sensors

	Actuator		
V_{AC}	Actuation voltage	0 – 120	V
ε	Permittivity of air	$8.85 \cdot 10^{-12}$	F/m
d_{AC}	Actuator electrode gap spacing width	5	μm
n_{AC}	Number of electrode gaps per actuator	340	
E	Young's modulus of silicon	169	GPa
w_A	Flexure width	6	μm
L_{AC}	Actuator flexure length	1,200	μm
L_{PF}	Actuator platform flexure length	1,000	μm
t	Material thickness	50	μm
	Position feedback sensor		
l_{PS}	Initial capacitive electrode overlapping plate length	70	μm
d_{PS}	Capacitive electrode gap spacing widths	5	μm
n_{PS}	Number of capacitive electrode gap spacings	170	μm

4 lists the design parameters of these linear actuators. For the position feedback sensors, two additional comb drives are used to measure the displacement of the actuators as a change in capacitance. Due to the large displacements of the actuators, lateral sensing, rather than transverse sensing, had to be chosen. Since electrostatic actuation and capacitive sensing is performed on the MEMS device in very close proximity, an electric line is added between the sensor and the actuator for shielding.

A special feature of the tensile tester is the ability to electrically contact each of the end effector arms. This allows for the simultaneous electromechanical characterization of the samples under investigation.

2.7 Microfabrication Processes

For the fabrication of the presented MEMS-based microforce-sensing tools with features down to a few micrometers, a lithographic-based microfabrication process is used. This enables the large-scale fabrication of these devices in a batch on wafer level. Two different process sequences are used. One sequence for the fabrication of devices with only in-plane sensing and actuating and another sequence for devices that incorporate in- as well as out-of-plane sensing. Both of these sequences involve only a combination of photolithography and dry etching steps, greatly facilitating the development of the microforce-sensing tools.

The microforce-sensing tools involving only in-plane sensing or actuation are fabricated using a bulk silicon microfabrication process described in [45]. It is based on a SOI wafer, out of which the devices are etched by DRIE only incorporating two photolithographic masks. The detailed microfabrication process flow is depicted in Fig. 16 and described hereafter.

A: A 100 mm diameter SOI wafer is used as the substrate material, with a handle layer thickness of 400 μm, device layers thickness of 50 μm and an intermediate SiO_2 layer with a thickness of 2 μm. Both silicon layers have a <100> orientation and are highly p-doped.

B: The handle layer is etched with DRIE where the SiO_2 acts as an etch stop and is removed subsequently with RIE. This will form the outer frame of the sensors. Since the sensors feature a probe overhanging the rest of the device, dicing cannot be performed to separate the individual dies. Therefore, a cavity surrounding each sensor is etched into the wafer in this step.

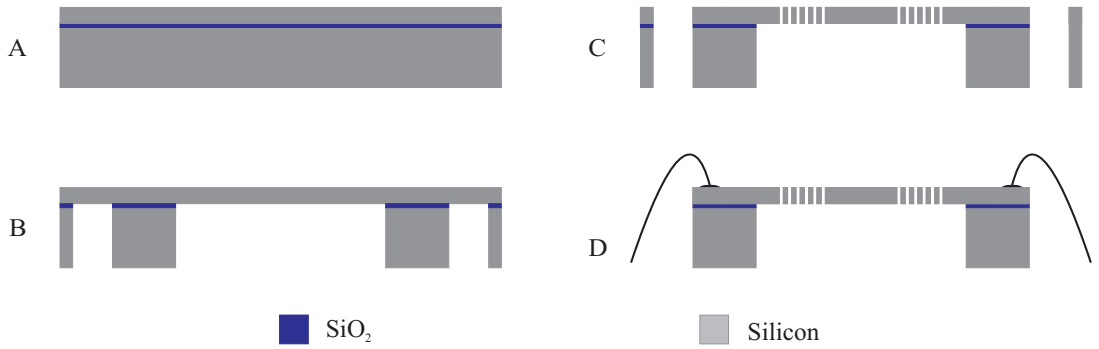

Fig. 16: Schematic of the SOI-based microfabrication process for in-plane sensing and actuation.

C: The wafer is mounted onto a support wafer using heat conductive grease (Cool grease, AI Technology Inc.), and the device layer is etched with DRIE to form the active parts of the sensors such as comb drives, flexures and the movable bodies.

D: In the last step the remaining photoresist is stripped in oxygen plasma and the sensors are glued onto printed circuit boards and wire bonded.

For the microfabrication of MEMS-based devices incorporating three-axis (in- and out-of-plane) sensing and actuation, only relative complex process flows are published, such as those presented in [4] and [23] involving a large number of masks, wafer bonding or microassembly steps. A novel microfabrication process, similar in complexity to the SOI process, has thus been developed, greatly facilitating the fabrication of three-axis sensors and actuators. It is based on a double SOI substrate with sequential etching of the two device layers using dry etching. Although commercially available double SOI substrates are more expensive, the reduction of photomasks (only three mask necessary) and fabrication steps results in a higher yield rate and, therefore, in a more economical fabrication. The fabrication process is depicted in Fig. 17. The photoresist layers are only shown in the steps involved in the sequential etching of the two device layers (D-F).

A: A 100 mm diameter double SOI wafer is used as a substrate, with a handle layer thickness of 400 µm, along with two device layers with a thickness of 25 µm and three SiO_2 layers with a thickness of 2 µm. All silicon layers have a <100> orientation and are highly p-doped.

B: The SiO_2 on the top device layer is structured with RIE to form an etch mask in the regions, where in the last step, wires are bonded to the lower device layer.

C: The handle layer is etched with DRIE where the SiO_2 acts as an etch stop and is removed subsequently with RIE. This will form the outer frame of the sensors. Since the sensors feature a probe overhanging the rest of the device, dicing cannot be performed to separate the individual dies. Therefore, a cavity surrounding each sensor is etched into the wafer.

D: The photoresist (AZ 4562) is applied with a thickness of 5 µm and structured to form a second etch mask on the top device layer. This defines the active parts of the sensors such as comb drives, flexures and the movable bodies.

E: The wafer is mounted onto a support wafer using heat conductive grease (Cool grease, AI Technology Inc.), and the top device layer is etched with DRIE. Subsequently the underlying SiO_2 is etched with RIE. The SiO_2 etch mask, formed in A, is removed during this step as well.

F: The lower silicon device layer is structured with DRIE with the same photoresist mask completely releasing the devices. At the same time the top device layer is etched in the regions where the SiO_2 mask was removed in step E.

G: The SiO_2 on the lower bonding regions is removed with RIE and the remaining photoresist is stripped in oxygen plasma.

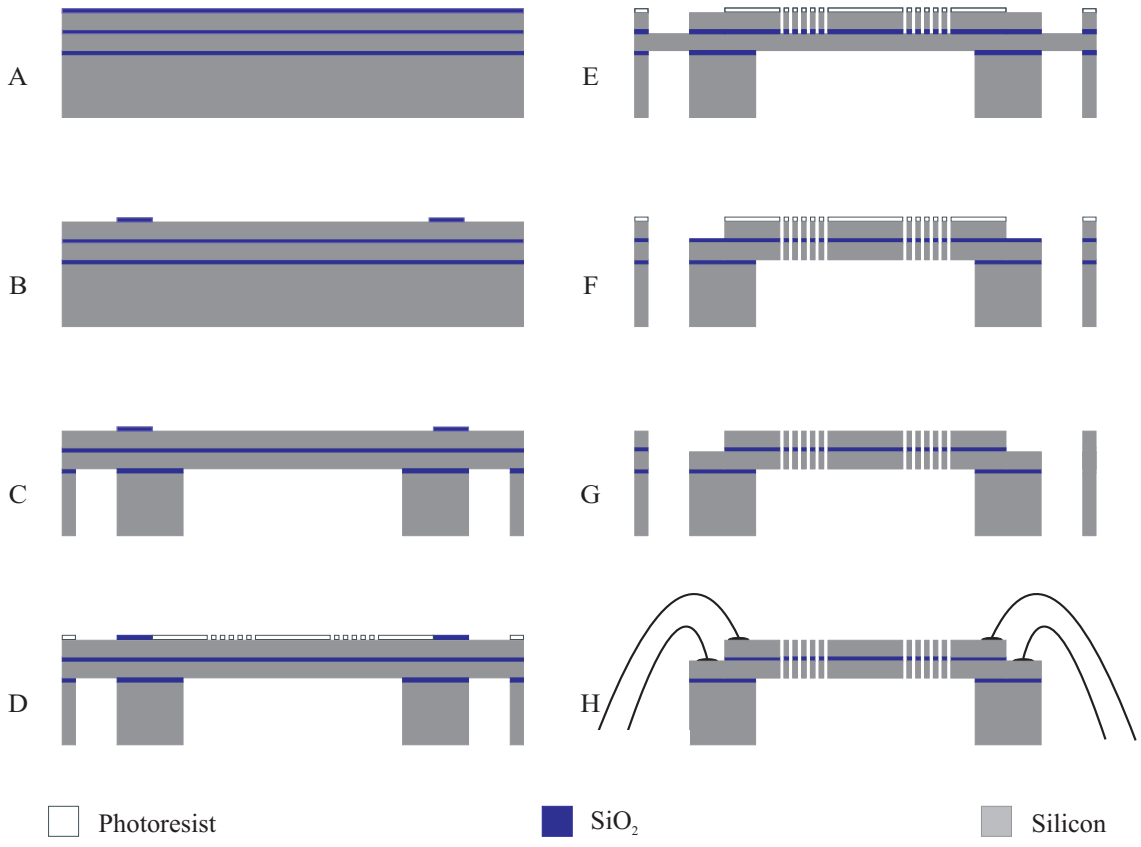

Fig. 17: Schematic of the double SOI-based microfabrication process for in- and out-of-plane sensing.

H: In the last step the sensors are glued onto printed circuit boards and wire bonded.

This three-mask fabrication process is not limited to the development of three-axis microforce sensors. The process could be utilized for the development of any kind of three-axis sensor or actuator with a major reduction in fabrication complexity.

2.8 Capacity-to-Voltage Conversion

The microforce-sensing tools convert an applied force to a displacement, which causes the capacitance of the attached electrodes to change. To measure this change in capacitance, it is converted to an analog voltage using commercially available capacitance-to-voltage (CVC) converter integrated circuits (ICs).

Two different CVC ICs are used: The universal capacitive readout MS3110 (Irvine Sensors Inc.) and the capacity-to-voltage-converter CVC1.1 (GEMAC Chemnitz GmbH [46]). The working principle of both readout ICs is based on the impedance relation measurement, where two periodic 180° phase-shifted excitation signals are applied to a capacitor pair (C_1 and C_2) as shown in Fig. 18. The demodulated response of the common (COM) electrode is then proportional to the ratio of the two capacities. The analog part of the block diagram of these mixed-signal ICs is shown in Fig. 19. It consist of a charge integrator with integration capacitance C_{int}, a sample hold cell, a low-pass filter where the cutoff frequency has been set to 5 kHz, and an amplifier stage with an additional gain (*Gain*) that can be set by a serial interface. The transfer function of the MS3110 CVC is shown in (2.19), where *V2P25* is the excitation voltage and V_{REF} is the offset voltage (both set to 2.25 V). Due to fabricational imperfections or parasitic capacitances the C_1 and C_2 capacitors on the sensor will not be exactly equal. They can, however, be trimmed to an equal value using the serial interface of the IC, so that the

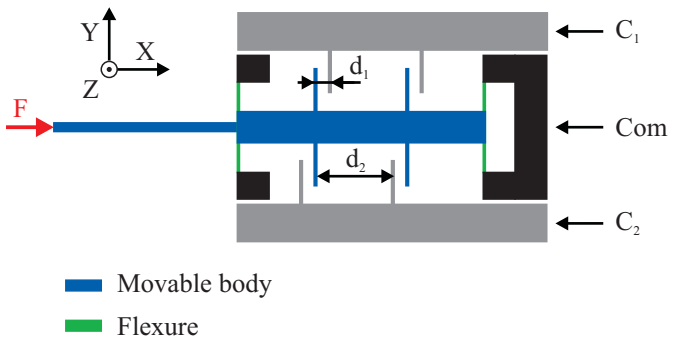

Fig. 18: Schematic of the electrical connections from a single-axis capacitive microforce-sensing probe to the capacity-to-voltage converter.

output signal of the CVC is equal to V_{REF} when no load is applied. All the settings are stored in an integrated electrically erasable programmable read-only memory (EEPROM) cell. The serial interface and the analog voltage readout have been realized using Labview (National Instruments Corp.) and a data acquisition card (NI PCI-6259, National Instruments Corp.).

$$V_{Out} = Gain \cdot V2P25 \cdot 1.14 \cdot \frac{C_{1T} - C_{2T}}{C_{Int}} + V_{REF} \tag{2.19}$$

$$C_{1T} = C_1 + C_{Trim1} \tag{2.20}$$

$$C_{2T} = C_2 + C_{Trim2} \tag{2.21}$$

A special feature of this readout is the ability to tune the electrical sensitivity of each capacitive sensor by changing C_{int} and *Gain*, as shown in (2.19), using the serial interface. This feature is used in the calibration step for tuning the sensitivity of the sensors to the desired value. In the microforce-sensing probes the stiffness of the flexures are designed such that they will deflect the half capacitive spacing by applying the maximum design force. C_{int} and *Gain* can be used to define the gain of the displacement to voltage conversion as shown in (2.12). Depending on these settings, the maximum reachable output voltage may occur at much smaller displacements than the half capacitive width, resulting in a smaller force range but a higher linearity of the sensor as shown in Fig. 5. These tuning parameters can therefore be used to adjust the sensing range and with that the sensor's characteristics, enabling the utilization of the devices for a different application with different force ranges. More details about the tuning of these sensing tools are presented in Section 3.8.

The MS3110 CVC is used for single-axis sensing probes, where only a single output channel is required. For multi-axis sensing tools multiple output channels are needed. Multiple MS3110 CVCs cannot be used to read out multiple capacitor pairs on a single sensing chip, since the

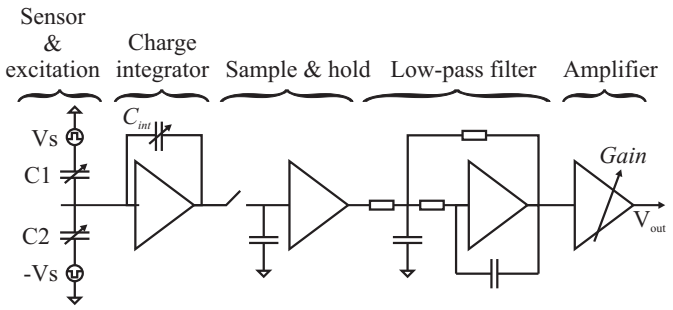

Fig. 19: Block diagram of the capacity-to-voltage converter IC (MS3110 and CVC 1.1).

excitation voltages cannot be synchronized, leading to cross coupling of the excitation signals from the different CVCs onto the common electrodes. Therefore for multi-axis sensing tools the CVC1.1 is used. Compared with the MS3110, it offers a smaller signal-to-noise ratio as demonstrated in Section 3.8, but allows for synchronization of multiple ICs for multichannel capacity-to-voltage conversion. The exact transfer function of the CVC is not known, but the output voltage is again proportional to the capacitive change as shown in (2.22). This IC also allows for capacitance trimming and sensor tuning using a serial interface. With synchronization capability, a dedicated capacitive-to-voltage converter IC is used for each of the capacitive sensors of the force-sensing tools (up to four on the microtensile tester).

$$V_{Out} \propto Gain \cdot \frac{C_1 - C_2}{C_{Int}} \tag{2.22}$$

Besides the capacitance-to-voltage converter, a digital humidity and temperature sensor (SHT75, Sensirion AG) is integrated into the printed circuit boards of some of the sensing tools, enabling the measurement of the environmental conditions.

2.9 Summary

Driven by the need for high-resolution and multi-axis sensing probes for micromechanical and microdimensional metrology, a variety of novel capacitive-based microforce-sensing tools have been developed. A three-axis microforce-sensing probe capable of measuring forces from nanonewton to micronewton as well as an integrated two-axis microtensile tester allowing for compression, tensile, as well as shear testing of microscopic samples have been realized. Great effort has been invested in obtaining the optimal design of these tools, ensuring a best possible separation of the different outputs, which enables a minimal measurement uncertainty in their results. Based on a novel microfabrication process, utilizing a double silicon-on-insulator substrate, a parallelized, large-scale fabrication of multi-axis sensors with a major reduction in fabrication complexity could be achieved. To convert the capacitive changes of these sensing tools to a measurable output signal a readout electronic based on a commercial capacity-to-voltage converter has been developed allowing for multichannel readouts as well as range tuning of the force-sensing tools.

In the next step, the exact relationship between the applied force and the resulting sensor output needs to be found by calibration, laying the basis for accurate measurements of forces in the micronewton to nanonewton range.

3 Sensor Calibration and Uncertainties Analysis

For the measurement of a force or a displacement, the sensing tools provide a related output voltage. But, since the exact relationship of the output voltage and the force/displacement is not precisely known, the only way to achieve accurate measurements is to initially calibrate the sensing tools. Analytical as well as FEM models of the sensors have been used for their design, but cannot be used to predict the forces/displacements from their outputs, since their accuracy is not known. The main reason for this limitation is the lack of knowledge of the exact geometry of the active elements, such as the flexures, due to imperfections in the microfabrication processes.

In this chapter, the calibration of the force as well as the displacement sensors used for these sensing tools is presented, along with the methodology to estimate the accuracy of their results. Therefore a short introduction to the current status and the challenges in the field of small-force metrology, the handling and estimation of measurement uncertainties as well as the definitions of the most relevant sensor characteristics are given.

3.1 Small-Force Metrology: Current Status and Challenges

Precise calibration of microforce sensors is difficult for several reasons, such as the lack of an accurate reference-force standard, the lack of standardized calibration procedures and the need to apply known force vectors at precise positions and orientations on these small and fragile microdevices. The most commonly used microforce sensor, the AFM, has led to the development of a large number of methods for calibrating forces in the micronewton and nanonewton range [47]. However, the accuracy of these methods is unknown since most of them are based on a model of the sensor and are therefore not SI-traceable, resulting in nonquantitative measurement results. Measurement results reported in literature, such as those in Table 5, for the same samples, e.g., the value for Young's modulus of materials can differ up to two orders of magnitude [48].

SI-traceable calibration requires that each calibration step is a comparison back to the primary

Table 5: Young's modulus measurements of the same silicon specimen with different AFM cantilevers [48]

Elasticity		**Sensing cantilever stiffness**	
0.7 – 0.96	MPa	0.06	N/m
10.5	MPa	0.95	N/m
183 – 299	MPa	40	N/m

standard, and that the uncertainty associated with its propagation from one device to the next is evaluated at each step in order to place bounds on the actual value of the unit after its propagation through this chain [31].

Force is a derived unit. The 11th General Conference on Weights and Measures (1960) has adopted the Newton as the unit of force in the International System of Units (SI) derived from the basic units of mass, length, and time as its primary standards. One Newton is the force required to accelerate a mass of 1 kg to 1 m/s^2. And with the kilogram remaining the only SI base unit defined by a material artifact, it is constantly in danger of being damaged or destroyed. The value of one kilogram is equal to the mass of the International Prototype Kilogram (IPK), a cylindrical body made of 90% platinum and 10% iridium alloy in 1878. The Bureau International des Poids et Mesures (BIPM) is responsible for the worldwide dissemination of the unit of mass, which is achieved via official copies of the IPK, known as national prototypes. Since the existence of the prototypes, there have been three periodic verifications. Each time the national copies are returned to the BIPM they are cleaned and washed and compared with the IPK. The third, latest periodic verification took place between 1988 and 1992. The results demonstrate a long-term instability of the unit of mass on the order of approximately 30 μg/kg over the last century [49] corresponding to a variation in the definition of 1 N by approximately 30 nN. This instability is attributed to surface effects of the IPK that are not yet fully understood and demonstrated the urgent need to redefine the kilogram using physical properties rather than a material artifact.

A number of scientific laboratories and National Metrology Institutes (NMIs), such as the National Institute of Standards and Technology (NIST), Physikalisch-Technische Bundesanstalt (PTB) and National Physical Laboratory (NPL) are currently investigating different approaches for a novel primary realization of the kilogram. The most promising solutions are the "Watt balance project" and the "Avogadro project."

The watt balance was developed at NPL by Dr. Bryan Kibble in 1975. It is based on the force between two current-carrying coils. By measuring the current necessary to support one kilogram, it can be redefined using the unit of ampere. The Avogadro project relates the kilogram to the mass of a fixed number of atoms by measuring the number of atoms in a perfect

(a) (b)

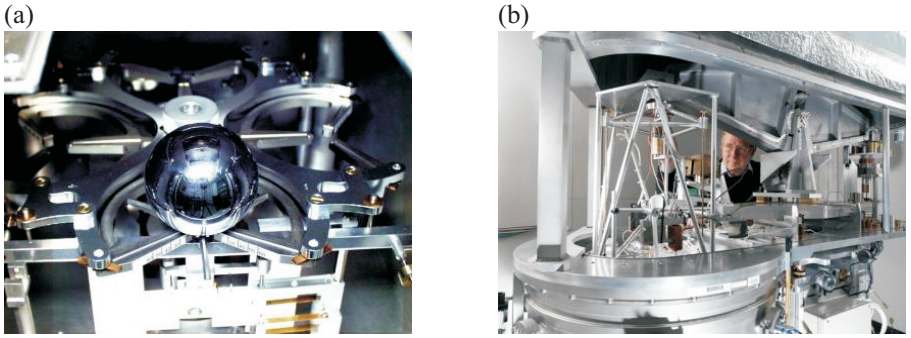

Fig. 20: Redefining the primary standard of the kilogram: (a) The avogadro project by NPL [50], (b) The watt balance project by NPL [50].

sphere of silicon. To date, there are still discrepancies between these two approaches. Until they have been resolved the kilogram remains the only SI base unit defined by a material artifact. Therefore, for the SI-traceable calibration of a force sensor, it must be compared back to its primary standard, the IPK, and is currently subjected to all its variations over time demonstrating an additional challenge in the calibration of small forces.

Macroscopic force sensors are calibrated using force standard machines, which apply a variety of SI-traceable mass artifacts combined with a suitably accurate estimate of the local gravitational acceleration while recording the resulting output signal of the sensor under investigation. The lowest SI-traceable mass artifact available on the market is 1 mg (corresponding to approximately 10 μN) [7]. Thus calibrating sensors down to approximately 10 μN is relatively simple. Currently efforts are being made to fabricate smaller SI-traceable calibration weights. The Korea Research Institute of Standards and Science (KRISS) has developed and calibrated a microweight set consisting of 0.05 mg, 0.1 mg, 0.2 mg and 0.5 mg artifacts for the calibration of AFM cantilevers [51]. However, there are limitations with this approach, since with smaller weights, their dimensions reach the resolving power of the human eye, making their handling increasingly challenging. Due to the mostly microscopic dimensions of the microforce sensor's probes, the application of deadweights is often not possible. For these reasons a new method for the calibration of micronewton and nanonewton forces needs to be found. Multiple NMIs have working groups focusing on the development of such systems; first and foremost NIST, NPL, KRISS and PTB. The most promising approach for the SI-traceable realization of small forces is based on the utilization of the electrostatic force between two electrodes, forming a capacitor. Both NIST [31] and NPL [52] are currently developing such electrostatic force balances (EFBs). This primary realization of a force avoids the use of the IPK and the related fluctuations as well as the need for microscopic mass artifacts. The electrostatic

force F_e between these electrodes can be calculated using (3.1). One of the two electrodes is fixed and the other is attached to a compliant mechanism, e.g., a flexure, allowing it to move along only a single axis. The gradient of the capacitance along this axis is *dC*/*ds*, where *ds* is the differential displacement of the moving electrode along the axis, *dC* the differential change in capacitance, and *V* the Voltage between the two electrodes. Measuring or generating a force can then be accomplished by measuring a capacitance gradient and the voltage necessary to counterbalance this force.

$$F_e = \frac{1}{2} \cdot \frac{dC}{ds} \cdot V^2 \tag{3.1}$$

The differential displacement can be traceably measured using a calibrated laser interferometer, and the capacitance gradient using a capacitance bridge with a traceable reference capacitor. The applied voltage may be traceably measured using a calibrated voltmeter. Currently, there are still unresolved challenges in reaching the expected accuracy with these EFBs, mainly related to the relatively complex mechanisms involved. But the results demonstrate this to be a promising approach for a primary realization of forces below 10 μN. Due to the relatively large size of these systems and complexity in their fabrication, both NIST and NPL are currently also working on a MEMS-based version of their EFB [52], [53].

In addition to a primary realization of small SI-traceable forces, a suitable transfer artifact that allows the dissemination of this primary standard to the industrial standards or instruments also needs to be found. Direct transfer of the primary force standard to the target instruments would in most cases be inappropriate due to the immobility of the primary standard or the target instruments [31]. An ideal microforce transfer artifact would require providing repeatable outputs during its entire lifetime, be insensitive to changes in its environment (or be held at the same conditions as during its initial calibration), have a well-defined loading point, be insensitive to off-axis loadings and be self-contained, meaning it would contain the majority of the electronics and signal processing onboard. Additionally it must be small enough to fit into the calibration equipment used for its initial calibration and for the calibration of the target equipment, and needs to be mobile and compatible in terms of shipping for its dissemination. All these restrictions make the development of a suitable transfer artifact a challenging task [7].

Commonly used transfer artifacts are electromagnetic compensation balances, or mass comparators. Actually designed for the measurement of mass, but in combination with the precise knowledge of earth's gravitational acceleration and a precision positioning stage, which is used to push a target sensor onto the balance, it can be used for the calibration of forces down

to the nanonewton. This approach has been successfully demonstrated by KRISS [54], which took advantage of the reliable, well-developed commercial weighing instruments. The major drawback of using these systems originates from their compensation method. The weight pan maintains its original position by counterbalancing the applied force. As a result, its observed stiffness is very high. When calibrating force sensors with a high stiffness such as those described in the preceding chapter, where the full range of force corresponds to a displacement of only a couple of micrometers (e.g., 2 μm), a minor drift of the micropositioner (e.g., 20 nm) used for the calibration will impose a relatively large drift of the force sensor's output (1% of the full-scale output), resulting in large uncertainties in the calibration data. To make matters worse, typical microbalances have relatively low readout frequencies (one output in 3 s for the XS205DU, Mettler-Toledo International Inc.), allowing more time for the positioner to drift in its position.

Other promising transfer artifacts are stiffness references. These are passive artifacts, such as elastic flexures with no onboard readout electronics. Their stiffness is calibrated by, e.g., an NMI, using their primary standard. Multiple different designs of such stiffness references from microfabricated reference cantilever arrays at NIST [55] to more complex helical springs called microfabricated arrays of reference springs (MARS) developed by NPL [56] have been demonstrated. The main disadvantage of this approach is the need for an accurate displacement measuring system for the initial calibration as well as during the calibration of the target system. The most promising approach for a reliable transfer artifact is rather the use of fully integrated microforce sensors that offer an integrated readout, delivering their output as a function of the applied force. PTB [57], NIST [58] as well as KRISS [59] have developed different designs of microforce transfer sensors, which rely on a cantilever design with piezoresistive deflection detection. They provide onboard sensing and readout circuits. Even though these piezoresistive cantilevers have been developed successfully, the devices are still far from the ideal transfer standard. Cantilever-based sensors are sensitive to off-axis loads and induce lateral motions when they are deflected, inducing slippage in the worst case.

Thus the utilization of the single-axis capacitive microforce sensors presented in Section 2.4 is proposed as a first in literature as the ideal microforce transfer standard. To date, none of the NMIs in the field of small-force metrology have persuaded the use of capacitive, microfabricated microforce sensors in the four-flexure configuration as transfer standards although this sensing principle has the potential to fulfill all the requirements of an ideal microforce transfer standard that were presented earlier in this section. They offer a parallel motion when deflected, integrated readout electronics, small dimensions, a well-defined tip for

the application of the force and are relatively insensitive to changes in environmental conditions and off-axis forces as demonstrated in Section 3.5. However, their primary calibration remains a challenging unresolved problem.

Since none of the NMI's approaches to realizing a primary small-force reference standard has matured enough to be utilized, a different approach for the calibration of these sensors (or transfer standards) has been developed. A combination of the highly accurate, compensated SI-traceable semi-microbalance (XS205DU, Mettler-Toledo International Inc.), deadweights and the macroscale reference-force sensor presented in Section 2.2 is used. The goal of this combination is to profit from the advantages of the mature microbalance technology while eliminating their disadvantages. Deadweights are used as a primary transfer artifact calibrated on a high-precision microbalance before each force-sensor calibration. This step takes advantage of the precision balance's high accuracy, but avoids the issue of its slow reaction time and its influence on the calibration uncertainty due to drifting of the sensor's signal. At the same time, it eliminates the effects of deadweight degradation and contamination, since they are recalibrated before each sensor calibration. In the second step, the calibrated deadweights are used to calibrate the microforce sensors. But due to the small geometry of the MEMS-based sensing probes, the additional macroscale reference-force sensor (as presented in Section 2.2) is introduced into the calibration chain, which can be calibrated by applying these deadweights. Finally, the MEMS-based sensors are pushed against this reference-force sensor using a micropositioner, while recording both signals. Since the reference-force sensor does not incorporate active force compensation and offers a fast readout (up to 10 kHz), the limitations of the microbalance are successfully avoided while still taking advantage of its high accuracy.

3.2 Uncertainty Analysis

The result of a measurement or calibration is only an approximation of the value of the measurand and, thus, is complete only when accompanied by a statement of the uncertainty of that estimate [60]. The measurement uncertainty is a parameter associated with the results of a measurement that characterizes the dispersions of the values that could reasonably be attributed to the measurand [61]. Therefore, for SI-traceability, besides the measurement result, its uncertainty also needs to be measured and propagated throughout the entire calibration chain, starting with the primary reference standard and its uncertainty.

The joint committee for guides in metrology (JCGM) of the BIPM has a working group responsible for the expression of uncertainty in measurements. They have published the

Table 6: Terms and definitions in the uncertainty analysis [60]

u	Standard uncertainty	Uncertainty of the result of a measurement expressed as a standard deviation
u_c	Combined standard uncertainty	Standard uncertainty of the result of a measurement when that result is obtained from the values of a number of other quantities
U	Expanded uncertainty	Quantity defining an interval (coverage intervals) about the result of a measurement that may be expected to encompass a large fraction p of the probability distribution of a measurement result
p	Level of confidence or coverage probability	The fraction of the probability distribution of a result contained within the bounds given by the expanded uncertainty
k_p	Coverage factor	Numerical factor used as a multiplier of the standard uncertainty in order to obtain the expanded uncertainty for a given level of confidence

International Organization for Standardization's (ISO) Guide to the Expression of Uncertainties in Measurements (GUM) [60], which has become the internationally accepted master document for the evaluation and combination of these uncertainties. In the GUM a deterministic method based on the law of propagation of uncertainties is described. It is based on the characterization of the uncertainties of all the measured input quantities by either normal or student's t-distribution, allowing the calculation of coverage intervals for the output quantities. For a better understanding of the terminology used in the uncertainty analysis, a few definitions and terms are presented in Table 6, as they are presented by the GUM [60].

In general a measurand y is not measured directly, but is determined from N other quantities x_i through a functional relationship f (3.2).

$$y = f(x_1, x_2, \cdots x_N) \tag{3.2}$$

The combined standard uncertainty $u_c(y)$ of the measurand y (in case of a reasonably linear functional relationship f) is given by (3.3), where $u(x_i)$ is the standard uncertainty of x_i. For a significant nonlinearity in f, higher-order Taylor series expansion coefficients need to be included.

$$u^2{}_c(y) = \sum_{i=1}^{N} \left(\frac{\partial f}{\partial x_i} \right)^2 \cdot u^2\left(x_i\right) + 2 \cdot \sum_{i=1}^{N-1} \sum_{j=i+1}^{N} \frac{\partial f}{\partial x_i} \cdot \frac{\partial f}{\partial x_j} \cdot u\left(x_i, x_j\right) \tag{3.3}$$

The second term in (3.3) only becomes relevant in the case of correlated input quantities. In the event of multiple measurements m of the input quantities, the combined standard uncertainty $u(x_i,x_j)$ can be expressed using the correlation coefficient $r(x_i,x_j)$ given by (3.5).

$$u\left(x_i, x_j\right) = r\left(x_i, x_j\right) \cdot u\left(x_i\right) \cdot u\left(x_j\right) \tag{3.4}$$

$$r\left(x_i, x_j\right) \approx \frac{\frac{1}{m-1} \cdot \sum_{l=1}^{m}\left(x_{i,l} - \overline{x_i}\right) \cdot \left(x_{j,l} - \overline{x_j}\right)}{\sqrt{\frac{1}{m-1} \cdot \sum_{l=1}^{m}\left(x_{i,l} - \overline{x_i}\right)^2} \cdot \sqrt{\frac{1}{m-1} \cdot \sum_{l=1}^{m}\left(x_{j,l} - \overline{x_j}\right)^2}} \tag{3.5}$$

The expanded combined uncertainty $U_c(y)$ for a given level of confidence p is given by (3.6) defining an upper and lower bound around the best estimate of a measurement within which the real result will lie, with the probability p.

$$U_c(y) = k_p \cdot u_c(y) \tag{3.6}$$

To deal with problems that are not linear or involve probability density functions (PDFs) other than the normal- or the student's t-distribution, the supplement one has been added to the GUM describing the Monte Carlo method (MCM) [62]. The uncertainty in a measurement is a result of several uncertainties. They can be categorized into two groups depending on how their values are estimated. The type A uncertainties are those that are evaluated by statistical methods and can often be described using a normal- or student's t-distribution. The type B uncertainties are those that are evaluated by other means, such as a prior knowledge of the system or specifications of the equipment, e.g., given by an upper and lower bound, defining a rectangular PDF. Both types of uncertainties can be incorporated into the analysis using the MCM.

The MCM evaluates the propagation of distributions by performing random sampling from the PDFs of all input quantities to predict the PDF of the output. And in the latest supplement

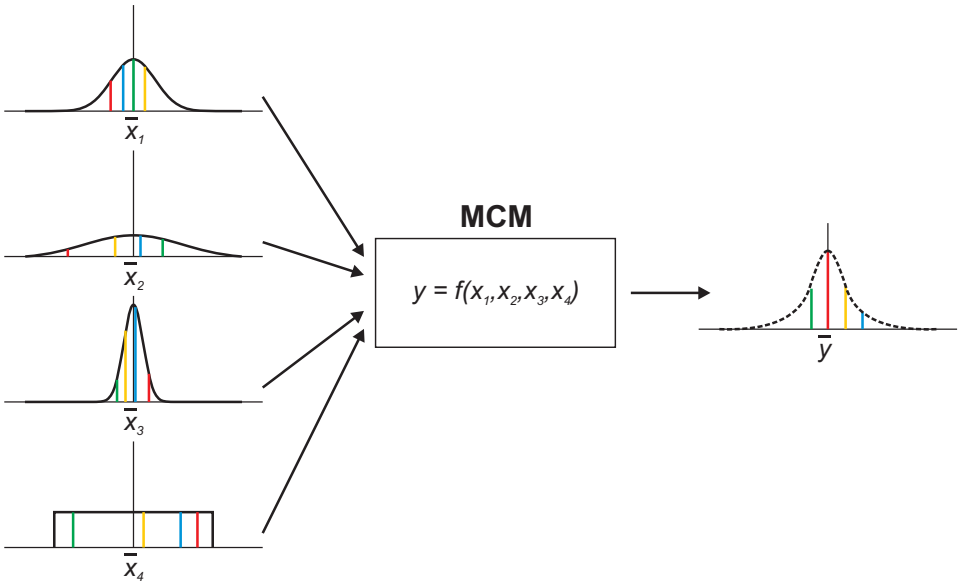

Fig. 21: Schematic of the Monte Carlo method (MCM).

two, these methods have been extended to multivariate problems with any number of output quantities. For the calculation of the uncertainty in the calibration coefficients as well as in force predications of microforce-sensing probes, the multivariate adaptive MCM is used. For comprehensive reasons a short introduction to the method depicted schematically in Fig. 21 is given here, and the complete description can be found in [63] or in the following sections, where it is applied for the calculation of the measurement uncertainties of the various sensing tools.

A number of M random samples are drawn from the PDFs of all input quantities of the transfer function f under investigation (e.g., ordinary least squares). Using the transfer function f, M multivariate model results can be calculated giving a discreet representation of the distribution function of the results. These M model results can then be used to calculate the best estimate of the results (e.g., the calibration coefficients), as well as their covariance and expansion coefficients. The effectiveness of the MCM depends on an adequately large value for the number of M Monte Carlo trials. Therefore, in the adaptive MCM an increasing number of Monte Carlo trials are carried out until the standard deviation of the results has stabilized in a statistical sense. In Section 3.4 the MCM is applied in each step of the calibration chain for the calibration of the microforce-sensing tools, shown with the cause and effect diagram in Fig. 22, in which the most relevant sources of uncertainty are listed. Additional sources of uncertainty (not shown in Fig. 22) and the estimation for their magnitude are listed in the Appendix (Section 8.1).

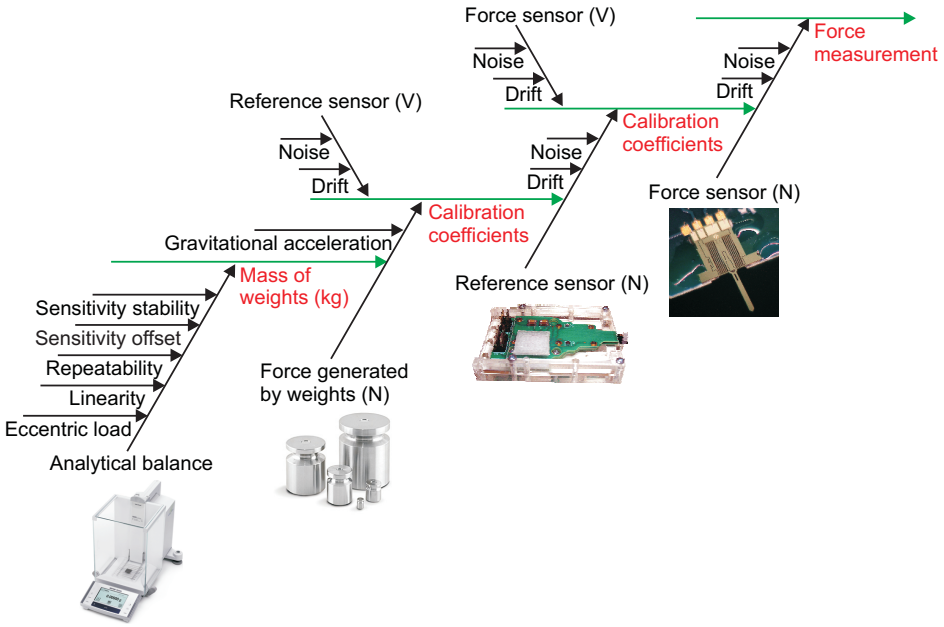

Fig. 22: Cause and effect diagram for the propagation of the diverse sources of uncertainty in the calibration chain.

3.3 Sensor Characteristics

A sensor is a device that converts a physical quantity (force) to an electrical quantity (voltage). A mathematical relationship is used to calculate the applied force from its output making a prediction of the applied force. A number of characteristic variables can be used to describe the quality of this conversion, enabling the estimation of the accuracy of a force prediction as well as the classification and comparison of such sensors. On the following pages the definitions of the most important characteristics of a force sensor are given. For some characteristics, multiple accepted definitions exist in the literature. The terms and definitions presented here have been found most suitable and are referred to within this thesis.

Differential measurement: A variety of forces are acting on a sample and the force sensor before coming in contact, such as the gravitational force. But as the sample is mechanically tested, the only force of interest is the interaction force of the sensor with the sample, e.g., the force response of the sample to the mechanical deformation caused by the sensing probe. So, to subtract all the other forces acting on the force sensor, differential force measurements must be made. This is accomplished by measuring the difference between the voltage signal of the sensor (proportional to the applied forces) before and during the sample interaction. Therefore, the characteristic parameters of the force sensors are not defined in terms of the absolute force or absolute output voltage, but rather in terms of their differential values, the applied force $F = (F_{measure} - F_{zero})$ and the output voltage change $V = (V_{measure} - V_{zero})$.

Input range: The interval between the maximum acceptable applied force (input full scale [FS]) and minimum acceptable applied force without causing an unacceptably large inaccuracy. The input range is also in general referred to as the range of the sensor.

Output range: The interval between the maximum reachable output voltage change (full-scale output [FSO]) and minimum reachable output voltage change of the sensor.

Ideal transfer function: Describes the ideal relationship between the applied force and the output voltage change of the force sensor, given by a mathematical equation such as (2.12).

Real transfer function: The actual transfer function of the force sensor, which differs from the ideal transfer function due to, e.g., parasitic effects or imperfections in the sensor fabrication. It cannot be measured exactly, due to the involved measurement uncertainties.

Calibration curve: The approximation of the real transfer function of the force sensor measured during the calibration process which is determined by comparing the sensor with a well-known reference standard. The calibration curve is most commonly given by a series of calibration points or a mathematical approximation of the calibration curve with, e.g., a polynomial function, which is used to make force predictions from the sensor's output voltage.

Calibration coefficient: The coefficients used to describe the calibration curve by, e.g., a polynomial approximation of the calibration data.

Sensitivity: The rate of change in the sensor's output voltage corresponding to the rate of change in the primary input, e.g., $\partial V/\partial F_x$.

Sensor gain: In the case of a linear sensor, the inverse of the sensitivity, referred to as the sensor gain, is used to make force predictions.

Cross sensitivity: The rate of change in the sensor's output voltage corresponding to the rate of change of parasitic input values, e.g., an off-axis force in the y-direction, $\partial V/\partial F_y$.

Selectivity: The sensor's ability to distinguish the primary input from a parasitic input, such as, e.g., the selectivity to an off-axis force in the y-direction in the case of a single axis sensor, designed to measure in the x-direction (3.7).

$$Sel_{x,y} = \frac{\frac{\partial V}{\partial F_x}}{\frac{\partial V}{\partial F_y}} \tag{3.7}$$

Resolution: The smallest incremental change in the input force that can be detected in the output voltage signal. This value is given by the noise level of the senor, a level of confidence and a measurement bandwidth. The resolution defines an upper and lower bound between which a measured signal will lie with a certain probability. (Assuming a normal distribution the 1σ–, 2σ– and 3σ–resolutions define an upper and a lower limit with an approximate level of confidence of 68%, 95% and 99%). Further details can be found in the definition of the noise level in Section 3.4.

Drift: Sensor output signal drift is defined as the uncertainty in a measurement due to the slow random fluctuation of the sensor's output over time without changing any inputs to the sensor. Further details can be found in the definition of uncertainty due to drift in Section 3.4.

Nonlinearity: An additional source of uncertainty is introduced in force predictions when the sensor's transfer function is approximated using a linear approach. The uncertainty due to non-linearity for a certain output voltage is given by the difference between the real transfer function of the sensor and the linear approximation. Since the real transfer function is not known, it is approximated using the calibration data and a polynomial function higher order (e.g., 3rd order). The nonlinearity can be described by different characteristic numbers, such as the maximum deviation of the linear to the higher-order approximation (max. nonlinearity) or as an additional uncertainty in the calibration coefficients with a rectangular PDF defined by the maximum nonlinearity per output voltage change as demonstrated in Section 3.7.

Repeatability: The uncertainty related to the difference between the results of successive measurements of the same measurand carried out under the same conditions of measurement. This is often referred to as the precision of a measurement and is a result of imperfections in the entire measurement system, rather than in just the sensor itself, whose repeatability generally is very good. Therefore the uncertainty related to the repeatability is given for a specific measurement system, or a calibration but not for a sensor it self. The standard uncertainty due to repeatability is characterized by the student's t-distribution, with N-1 degrees of freedom where N is the number of repeatable measurements made.

Force prediction: This is the result of using the calibration curve with the output voltage of the sensor, to estimate (predict) the corresponding applied force.

Static measurement: Measurements of static or slow varying forces, where the dynamics of the sensor do not need to be taken into account. Measurements are considered static up to a frequency smaller than 0.1 times the resonance frequency of the sensor.

Accuracy: The term “accuracy” is used commonly in the literature to describe the closeness between the measurement and the true value of the measured quantity. Since (most commonly) there is no a priori knowledge of the true value of the measured quantity, this term should not be used together with a quantitative value. The term “accuracy” generally refers to the “expanded combined uncertainty,” which gives an upper and lower bound around the best estimate between which the true value of the measured quantity will lie with a certain level of confidence.

Initial stabilization time: After the sensor is powered up, a large signal drift can be observed, as shown in Fig. 23. The major part of this appears within the first 5 min after powering up the sensor. Consequently measurements are performed after an initial stabilization time of at least 5 min. In general, an initial stabilization time of 12 h is used.

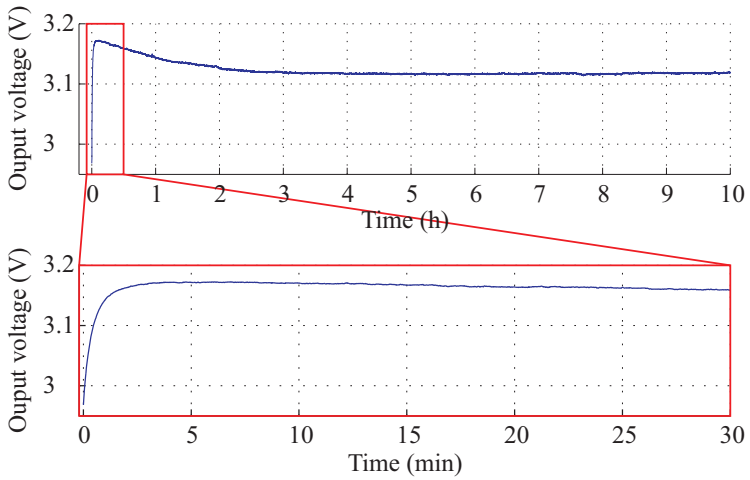

Fig. 23: Initial stabilization characteristic of a microforce-sensing probe based on the MS3110 CVC.

3.4 Calibration of the Single-Axis Reference-Force Sensor

Due to the lack of an accurate reference standard for the calibration of forces below 10 µN, an SI-traceable compensated semi-microbalance (XS205DU, Mettler-Toledo International Inc.) is used as a primary reference, which is precalibrated by the manufacturer with a given uncertainty. To transfer this reference standard to the different MEMS-based microforce-sensing tools, a combination of deadweights and the macroscale reference-force sensor, presented in Section 2.2, is used. This combination benefits from the high accuracy and very mature technology of the precision balance while eliminating the disadvantage of the slow reaction time and its influence on the calibration uncertainty due to drift of the sensor's signal when directly used as a reference, pushing the target sensor against it using a micropositioner.

First, the semi-microbalance is used to determine the weight of 10 different steel deadweights. These deadweights, as the primary transfer standard, are used to calibrate the reference-force sensor by applying them multiple times onto the sensing probe while recording the output voltage change. To determine the corresponding force acting on the sensor due to these applied masses, the local gravitational acceleration g [64] is used. The calibration data is shown in Fig.

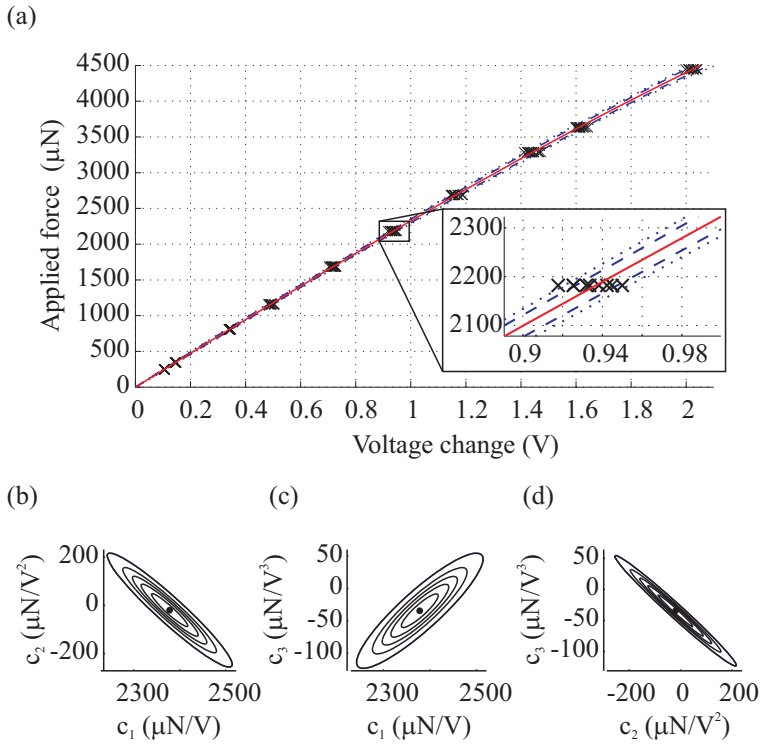

Fig. 24: Calibration results of the single-axis reference-force sensor consisting of (a) the calibration data (x) as well as the best estimate (-), the 68% (--), and the 95% (..) coverage intervals of the calibration curve, (b) – (d) contour lines of the multivariate PDF of the calibration coefficients for coverage probabilities of 10%, 30%, 50%, 70% and 90%, projected onto the calibration coefficient plane of (b) c_1 and c_2 (c) c_1 and c_3 (d) c_2 and c_3.

24. To eliminate the effect of deadweight degradation and contamination, the weights are recalibrated before each sensor calibration.

The uncertainty of the calibration is calculated using the multivariate adaptive MCM as described in [63]. The uncertainties in the calibration force are only related to the uncertainties of the semi-microbalance and the uncertainty due to repeated application of the weights onto the balance as well as the force sensor during calibration. The uncertainty in g as well as in the pressure, humidity and temperature can be neglected, since their contributions are undetectable within the significant digits used in this analysis (the detail confirming these assumptions can be found in the Appendix in Section 8.1). The PDFs, which corresponds to all the sources of uncertainty in the calibration force, are shown in Table 7.

For the calibration output voltage of the reference sensor, two effects mainly contribute to the uncertainty in the signal – noise and drift. These uncertainties are measured before the sensor is calibrated by sampling the output voltage over 10 minutes at the same frequency as during the calibration (10 Hz). Before the sensor is used an initial stabilization time of 12 h is allowed.

The standard uncertainty due to drift (u_{Drift}) is defined as the uncertainty in a measurement due to the slow, random fluctuations of the sensor's output voltage over time without changing any inputs to the sensor. Since signal drift has amplitudes that vary randomly with time, it can only be specified by a PDF. The uncertainty due to drift is measured before the sensor is used by sampling the output voltage over a certain time period, e.g., 10 min at 10 Hz. To filter out the effect of signal noise on the output voltage, a moving average filter with a sample size of 50 is applied first, as shown in Fig. 25(a). The uncertainty due to drift depends on the measuring time and, therefore, needs to be measured for all possible time intervals, e.g., from t = 0.1 s to t = 30 s in increments of 0.1 s. The standard uncertainty due to drift is calculated from the filtered voltage data V_{MA} according to (3.8).

$$u(t)^2_{Drift} = \frac{1}{n_d - 1} \cdot \sum_{j=0}^{n_d} \left[\max\left([V_{MA,j}, V_{MA,j+t\cdot\Delta t}] \right) - \min\left([V_{MA,j}, V_{MA,j+t\cdot\Delta t}] \right) \right]^2 \tag{3.8}$$

With a measurement time of 10 min and a measurement frequency of 10 Hz (Δt = 10) the number of drift measurements is n_d = 5,700 (t_{max} = 30 s). Using the central limit theorem a normal distribution can be assumed. The standard uncertainty due to drift is shown in Fig. 5(b) as a function of the time interval length. It increases with the measurement time interval t = $t_{meassure}$ - t_{zero}. In a differential voltage measurement V = ($V_{measure}$ - V_{zero}), only V_{zero} is subjected to the signal drift.

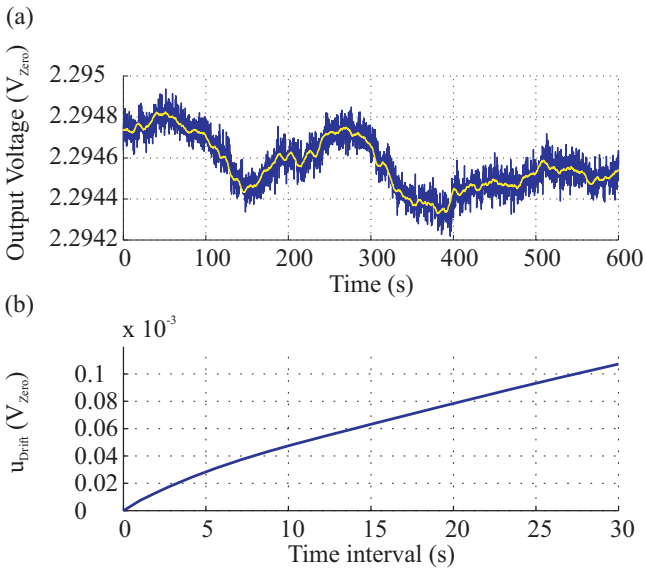

Fig. 25: (a) Sensor output voltage V_j and the moving average filter output voltage $V_{MA,j}$; (b) standard uncertainty due to the sensor output signal drift as a function of the time interval, extracted from the data in (a).

The standard uncertainty due to noise (u_{Noise}), also referred to as the 1σ-resolution, is defined as the uncertainty in a measurement due to the fast random fluctuations of the sensor's output voltage. Since signal noise has amplitudes that vary randomly with time, it can only be specified by a PDF. The standard uncertainty due to noise is given by the standard deviation of the sensor's output voltage given by (3.10), which is measured before the sensor is used by sampling its output voltage over a certain time period, e.g., 10 min at 10 Hz (same frequency as during the calibration/measurement). To filter out the uncertainty due to drift, the moving average filtered data V_{MA} is first subtracted from the output voltage V_j (3.9).

$$V_{N,j} = V_j - V_{MA,j} \tag{3.9}$$

$$u^2{}_{Noise} = \frac{1}{n_n - 1} \cdot \sum_{j=0}^{n_n} \left(V_{N,j} - \bar{V}_N \right)^2 \tag{3.10}$$

With a measurement time of 10 min and Δt = 10, the number of noise measurements is n_n = 5,950, justifying the utilization of a normal distribution to describe this uncertainty. Depending on the necessary measurement frequency, this data can be averaged, resulting in a reduction of the noise by a factor of approximately $n^{-0.5}$, where n is the number of samples averaged over. The standard (1σ) uncertainty due to noise is given as an amplitude with the corresponding frequency up to which measurements must be taken (or per square root of the frequency bandwidth).

Table 7: Uncertainties in the single-axis reference-force sensor calibration

Source of uncertainty	Number of measurements	Probability density function
Uncertainties given by the specifications of semi-microbalance (given as upper and lower limits)	-	Rectangular
Uncertainties given by the specifications of semi-microbalance (given as standard deviation)	-	Normal
Repeatability of mass measurements of the reference steel weights	5	Student's t
Repeatability of weight applications onto the single-axis reference sensor	5	Student's t
Noise in the sensor output voltages	5,950	Normal
Drift of the sensor output voltages	5,700	Normal

All the PDFs from the different sources of uncertainty shown in Table 7 are used to create one joint PDF for each applied force and for each output voltage change in the calibration data. By randomly sampling from these joint PDFs and using the method of ordinary least squares, a third-order polynomial function as shown in (3.11) is fit into the calibration data for each of the $M = 10^4$ Monte Carlo trials, minimizing the residual $\boldsymbol{r_i}$. These M sets of the calibration coefficients (c_1, c_2, c_3) give a discrete representation of the multivariate PDF of the result. From this PDF the best estimate, its standard uncertainties as well as the correlation and expansion coefficient of the calibration coefficients can be calculated.

$$\boldsymbol{F}_i = \left(\boldsymbol{V}_i \quad \boldsymbol{V}_i^2 \quad \boldsymbol{V}_i^3\right) \cdot \left(c_{1,i} \quad c_{2,i} \quad c_{3,i}\right)^{\mathrm{T}} + \boldsymbol{r}_i \qquad \text{for } i = 1 - M \qquad (3.11)$$

The MCM is carried out multiple times, until the results have stabilized as shown in Fig. 26. This occurs when twice the standard deviation of all the calibration characteristics is smaller than the numerical tolerance, as defined by the number of relevant significant digits [63]. The final results of the adaptive MCM are calculated taking the entire $h \cdot M$ realization of the calibration coefficients (with h the number of Monte Carlo iterations) into account and are shown in Table 8. For this resulting multivariate PDF (third order), no coverage interval with only an upper and a lower bound – as is the case for only one variable – can be defined. For three outputs, a coverage volume (ellipsoid) is needed whose contour lines for coverage probabilities of 10%, 30%, 50%, 70% and 90%, are shown in Fig. 24 as projections onto the calibration coefficient plane. By using this multivariate PDF as input for the uncertainty calculation of the force predictions made with this sensor, the correlation between the coefficients is adequately taken into account. In Fig. 24(a) the calibration data and the best estimate from the $h \cdot M$ least squares fits, as well as the coverage interval for the two coverage probabilities $p_1 = 68\%$ and $p_2 = 95\%$ are shown.

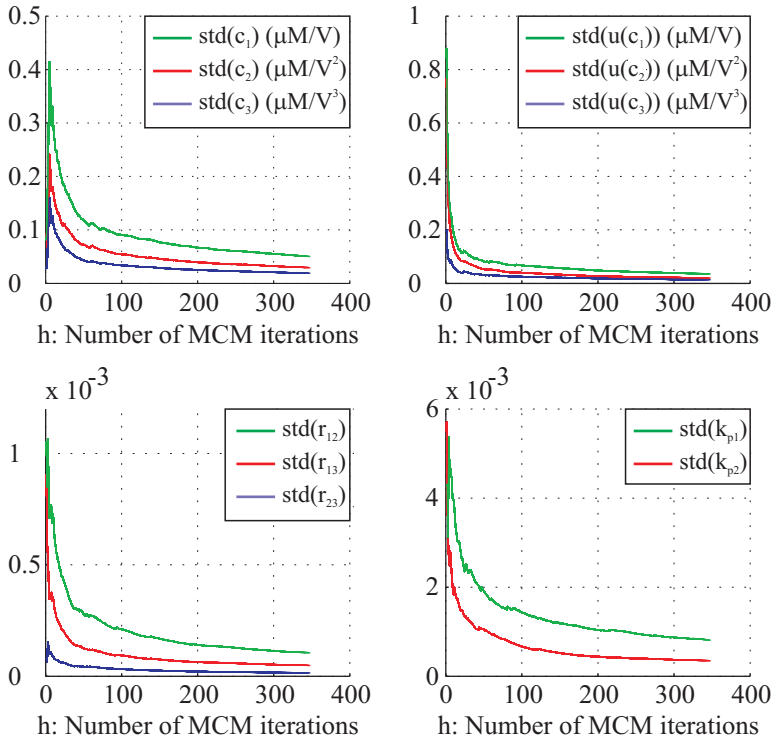

Fig. 26: Numerical stabilization of the MCM with the increasing number of iterations for the standard deviation of (a) the calibration coefficients, (b) the uncertainty in the calibration coefficients, (c) the correlation coefficients and (d) the expansion coefficients.

Table 8: Calibration and uncertainty analysis results: single-axis reference-force sensor

Input range (μN)	4,800
Output range (V)	2.25 – 4.5
Calibration coefficients ($\mu N/V\ \mu N/V^2\ \mu N/V^3)^T$	$(2{,}378.2\ -19.7\ -34.4)^T$
Standard uncertainties ($\mu N/V\ \mu N/V^2\ \mu N/V^3)^T$	$(53.8\ 93.8\ 35.3)^T$
Correlation coefficients	
r_{12}	-0.952
r_{13}	-0.895
r_{23}	-0.986
Expansion coefficient k_p for	
$p1 = 0.68$	1.84
$p2 = 0.95$	2.86
# MCM iterations: $h \cdot M$	$3.49 \cdot 10^6$
u_{Noise} at 10 Hz (μN) PDF: normal	0.11
u_{Drift} (t = 30s) (μN) PDF: normal	0.25
C_{int} MS3110 (pF)	5
Gain MS3110	4

3.5 Calibration of Single-Axis MEMS-Based Microforce-Sensing Probes

In this section the calibration as well as the complete characterization of the single-axis MEMS-based microforce-sensing probes as presented in Section 2.4 are described. The calibration and extraction of the parameters needed to make force predictions and calculate their uncertainties, the measurement of the cross sensitivity to off-axis forces, as well as the influence of variations in the environmental conditions, such as the temperature and humidity are presented.

Due to the microscopic dimensions of the sensing probe of MEMS-based microforce sensors, it is not possible to calibrate them by applying deadweights. The reference-force sensor (presented in Section 2.2) is thus used as a transfer standard for which the relationship between its voltage change and the applied force is known, since it has been precalibrated, as shown in the previous section. By pushing this reference stepwise against the MEMS-based sensor using a motorized linear stage (MT1-Z6, Thorlabs Inc.) and recording the voltage change from both sensors, the calibration curve of these microfabricated-sensing probes can be recorded as shown in Fig. 27. For accurate positional and rotational alignment of the two sensors, the MEMS-based sensor is mounted on a three-axis micropositioner (MP-285, Sutter Instrument Co.) and the entire setup is fixed under a high-resolution microscope (A-ZOOM, Signatone Corp.). A

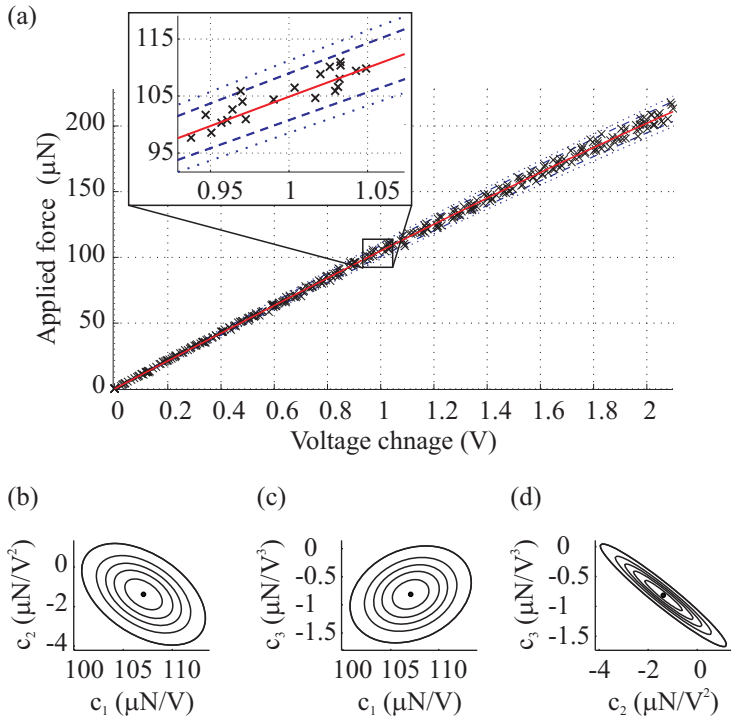

Fig. 27: Calibration results of the single-axis MEMS-based microforce-sensing probe consisting of (a) the calibration data (x) as well as the best estimate (-), the 68% (--), and the 95% (..) coverage interval of the calibration curve, (b) – (d) contour lines of the multivariate PDF of the calibration coefficients for coverage probabilities of 10%, 30%, 50%, 70% and 90%, projected onto the calibration coefficient plane of (b) c_1 and c_2 (c) c_1 and c_3 (d) c_2 and c_3.

schematic of the calibration setup is shown in the Appendix in Section 8.5.

The sensor is calibrated 10 times and the entire data set is used to calculate its calibration coefficients. A third-order polynomial function is used for the approximation of the calibration curve, eliminating additional uncertainties due to nonlinearity. For the adaptive multivariate MCM, the uncertainties due to noise and drift of both sensors are taken into account as described in (3.8) and (3.10), and are represented by normal distributions. The repeatability is characterized by the mean square error between the recorded calibration data and the least squares fit and is represented by a normal distribution. The uncertainty in the calibration coefficient of the reference-force sensor, described by its multivariate PDF shown in Fig. 24 (b) – (d), is accounted for by random sampling with equal probability from the $h \cdot M$ result of its MCM. The results of the single-axis MEMS-based sensor calibration and its adaptive MCM are shown in Table 9. Due to the symmetric design of the sensor and the inherent challenge of calibrating tension forces, a symmetric characteristic of the sensor for positive as for negative forces is assumed.

To characterize the fabrication process of these sensors and demonstrate the fact that the analytical (or FEM) model cannot be utilized for the prediction of the sensor's transfer function, a total number of 371 sensors of the same type have been calibrated. The results depicted in Fig. 28 show a variation of the input range, from ±94 µN to ±243 µN, as shown by its distribution function, whereas by using the analytical model of the sensing probe a range of ±220 µN is expected. This variation is assumed to be related to fabricational imperfections such as an overexposure or underexposure of the photoresist or overetching of the active elements such as the flexures and the capacitor plates during microfabrication. Through the introduction of an *overetch* variable this effect is taken into account in the analytical sensor model enabling the

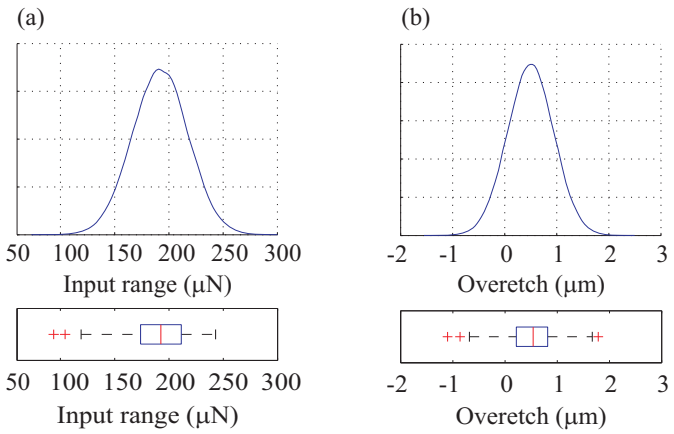

Fig. 28: The probability density function of (a) the input range and (b) the resulting dimensional *overetch*, extracted from the calibration of 371 single-axis MEMS-based microforce-sensing probes.

calculation of the difference between the fabricated and the designed dimensions. Thinner flexures (positive *overetch*) or thicker flexures (negative *overetch*) will result in a change of the sensor stiffness ($k \sim w^3$) and variation in the capacitor gaps. By solving this extended analytical model for each of the calibrated sensors, the *overetch* for each device can be found. The resulting distribution density function of the *overetch* is shown in Fig. 28(b), indicating a thinning of the flexure and a widening of the capacitor gaps of 2 ± 1.8 (two times the *overetch*).

Besides the calibration of these single-axis sensing probes along their sensitive direction, its sensitivity to parasitic inputs (cross sensitivity), such as off-axis forces or changes in the environmental conditions, need to be measured to estimate their influence on the uncertainty of a force prediction. The cross sensitivity of the sensing probes to off-axis forces is measured by calibrating the sensor along the two off-axis directions (the y- and z-directions). The resulting measurement data as well at the best estimate and standard uncertainty of the cross sensitivity is shown in Fig. 29. Due to the rotational motion that the movable body of the sensor undergoes, slippage between the two probes occurs, leading to a strong fluctuation in their outputs. For the cross sensitivity to forces in the y-direction under the same conditions, positive as well as negative output voltage responses were detected, indicating a near to perfect angular alignment during the cross sensitivity measurement and a negligible cross sensitivity to forces in the y-direction. In the z-direction, the results demonstrate a selectivity of the single-axis sensing probe of 26 ± 5. When utilizing these sensing probes to measure a force, together with an estimate of the angular misalignment between the force and the sensor's sensitive axis, the selectivity results can be used to estimate the resulting additional measurement uncertainty in a force prediction. At an angular misalignment of, e.g., 1° in the z-direction and a force measurement of 200 µN, the actual force would be (when perfectly aligned) 200.03 µN. The off-axis force

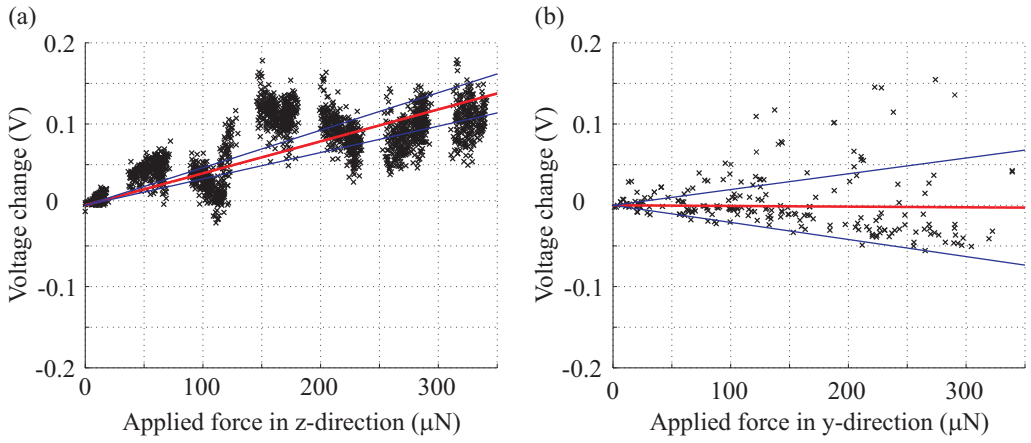

Fig. 29: Cross sensitivity measurement data (x) as well as the best estimate (-) and its standard uncertainty (-) for the applied force (a) in the z-direction and (b) in the y-direction

component corresponds to 3.5 µN, which will result in a parasitic input in the z-direction causing an additional uncertainty of 0.13, µN resulting in a total measurement uncertainty of 0.14 µN due to an estimated angular uncertainty of 1°.

Because of the full integration of these microforce-sensing probes, their compact size, the highly parallel motion of the movable body when deflected and their relatively small cross sensitivity to off-axis forces, these sensors are promising candidates for an ideal transfer standard for the calibration of forces in the micronewton to nanonewton range.

An additional prerequisite for the utilization as a transfer standard is a low sensitivity to changes in environmental conditions such as temperature and humidity. These conditions can vary significantly from the initial calibration of the sensor to its utilization in the calibration laboratory. The three main contributions are expected to be variations of the dielectric constant, thermal material expansion, and the influence of the temperature on the CVC. Using an analytical approach it can be found that the temperature, humidity and pressure will not have a significant influence on the dielectric constant (more details on this are presented in the Appendix, Section 8.1). But since estimating the influence of temperature variations is difficult, an experimental setup was developed, allowing for the measurement of the sensor output voltage as well as its sensitivity (or sensor gain) as a function of the temperature and humidity. By rotating the sensor around its out-of-plane axis aligned horizontally (z) (rotating the sensor from pointing upwards to downwards) the output voltage signal undergoes a sinusoidal fluctuation. The difference between the maximum and minimum output voltage corresponds to

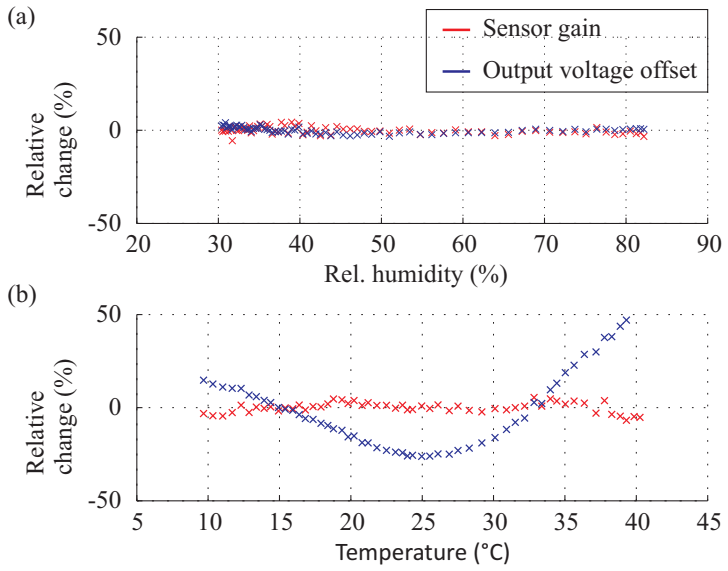

Fig. 30: Influence of (a) the relative humidity change from 82% RH to 18% RH (at 25.2 ± 0.9 °C) and (b) the environmental temperature change from 10 °C to 40 °C (at 59 ± 19% RH) on the sensor's output voltage offset and sensing gain.

twice the mass of the movable-sensing body, which, since the movable mass does not change, is proportional to the sensitivity of the sensor. The mean of the maximum and minimum output voltage corresponds to the zero-load offset. The exact knowledge of the sensor mass is not needed, since only the relative variation of these values as a function of the temperature and humidity are of interest.

The measurement setup is mounted into an environmental chamber (YTH-90Z-H, Welltech Instruments Co. Ltd.) allowing for variation in temperature and humidity, which are measured using a temperature/humidity sensor (SHT75, Sensirion AG) in close proximity to the microforce sensor. To enable a large output signal change due to the small mass of the sensor a different sensor design with much longer flexure length (flexure dimensions: length 2,000 μm, width 5 μm and thickness 50 μm) is used, resulting in an approximate voltage signal of 0.8V (output voltage change caused by rotating the force sensor from pointing upwards to pointing downwards). While measuring the sensitivity as well as the output voltage offset, the relative humidity (RH) of the air inside the chamber was first varied from 82% RH to 18% RH at a temperature of 25.2 ± 0.9 °C (within a time of 10 min). The result shown in Fig. 30(a) indicates a negligible correlation between the sensor gain and the humidity (correlation coefficient r_H = 0.0665). In a second measurement, the temperature of the air inside the chamber was varied from 10 °C to 40 °C (within a time of 8.5 min). Since it was intended to perform this

Table 9: Calibration and uncertainty analysis results: single-axis MEMS-based microforce-sensing probe

Input range *Fx* (μN)	±230
Output range (V)	0 – 4.5
Calibration coefficients (μN/V μN/V^2 μN/V^3)^T	$(107.07\ -1.38\ -0.81)^T$
Standard uncertainties (μN/V μN/V^2 μN/V^3)^T	$(2.52\ 1.02\ 0.34)^T$
Correlation coefficients	
r_{12}	-0.468
r_{13}	0.247
r_{23}	-0.960
Expansion coefficient k_p for	
$p1$ = 0.68	1.86
$p2$ = 0.95	2.80
# MCM iterations: $h \cdot M$	$2.88 \cdot 10^6$
u_{Noise} at 10 Hz (μN) PDF: normal	0.02
u_{Drift} (t = 30s) (μN) PDF: normal	0.07
Selectivity of Fx to Fy	∞
Selectivity of Fx to |Fz|	26 ± 5
C_{int} MS3110 (pF)	4
Gain MS3110	4

measurement in moist air, the resulting relative humidity (RH) could not be held constant, resulting in 59 ± 19 % RH. The result shown in Fig. 30 indicates a negligible correlation between the sensor gain and the temperature (correlation coefficient $r_T = 0.0256$). However, there is a relation between the temperature and the output voltage offset of the sensor. But due to the differential force measurement principle, only changes in the sensor gain are relevant since the variations in the environmental conditions during a single force measurement are neglected, because they occur slowly and microforce measurements are taken in time intervals of less than 30 s.

The characterization of the single-axis MEMS-based microforce sensors have indicated that the model-based approach for the estimation of the transfer function of microforce sensors is not suitable for accurate force predictions. Further, it has been demonstrated that capacitive microforce sensors in the four-flexure configuration are close to being ideal candidates for a transfer standard, enabling the accurate dissemination of the primary standard from the NMI.

3.6 Calibration of Multi-Axis MEMS-Based Microforce-Sensing Probes

A multi-axis microforce sensor requires the calibration along all its sensitive directions. In the case of a linear sensor it is sufficient to sequentially calibrate the sensor along its different sensitive directions while no load is applied to the other directions, and to use the principle of linear superposition to predict its output as a combination of forces from multiple directions are applied simultaneously. A linear sensor also allows for the representation of its multidimensional transfer function by a calibration matrix enabling the prediction of the applied force magnitude and direction from the output voltage signals (vector) of the sensor.

The outstanding characteristics of the single-axis microforce-sensing probe presented in the previous section suggest its application as a transfer standard for the calibration of the multi-axis sensing probes. To enable the precise alignment of the two sensors with each other, the multi-axis sensor is mounted onto a three-axis micropositioner (MP-285, Sutter Instrument Co.) under a high-resolution microscope (A-ZOOM, Signatone Corp.), and for the straight-lined approach of the two sensors the single-axis reference sensor is mounted on a linear stage (MT1-Z6, Thorlabs Inc.). A schematic of the calibration setup is shown in the Appendix in Section 8.5. By pushing the reference sensor sequentially against all the sensitive directions of the multi-axis sensor and measuring all the output voltages of the two sensors, the calibration curves can be found. This data can then be used (in the case of a linear sensor), to extract the calibration matrix $\boldsymbol{A}$, describing the relationship between any combination of output voltages of the sensor

and the corresponding applied force. The calibration curves of the two-axis microforce sensor presented in Section 2.5, integrated into the microtensile tester (Section 2.6), are shown in Fig. 31. Due to the linear relationship, the system can be represented by a calibration matrix $\boldsymbol{A}^{2x2}$, describing the relationship between the two output voltages of the two-axis force sensor and the applied forces in the x- and y-directions acting on its end effector.

The uncertainties in the calibration matrix are calculated using the adaptive multivariate MCM. The influence of the sensor signal drift and noise of both sensors is described by (3.8) and (3.10) utilizing normal distributions. The uncertainty given by the root mean square error between the calibration data and the linear fit is also introduced using a normal distribution. The uncertainty in the applied force given by the reference-force sensor calibration is accounted for by sampling from its distribution function. All the PDFs defined by the different sources of uncertainty are combined into a joint PDF for each of the calibration data points. By taking $M = 10^4$ random samples from all the joint PDFs, M calibration data sets (3.12) and (3.13) are created, where Vc_i is the voltage from the two-axis force sensor of the tensile tester and Fc_i is the applied force, given by the reference-force sensor with i from 1 to M. Using the ordinary least squares method (3.15), M calibration matrices can be calculated. This MCM is carried out

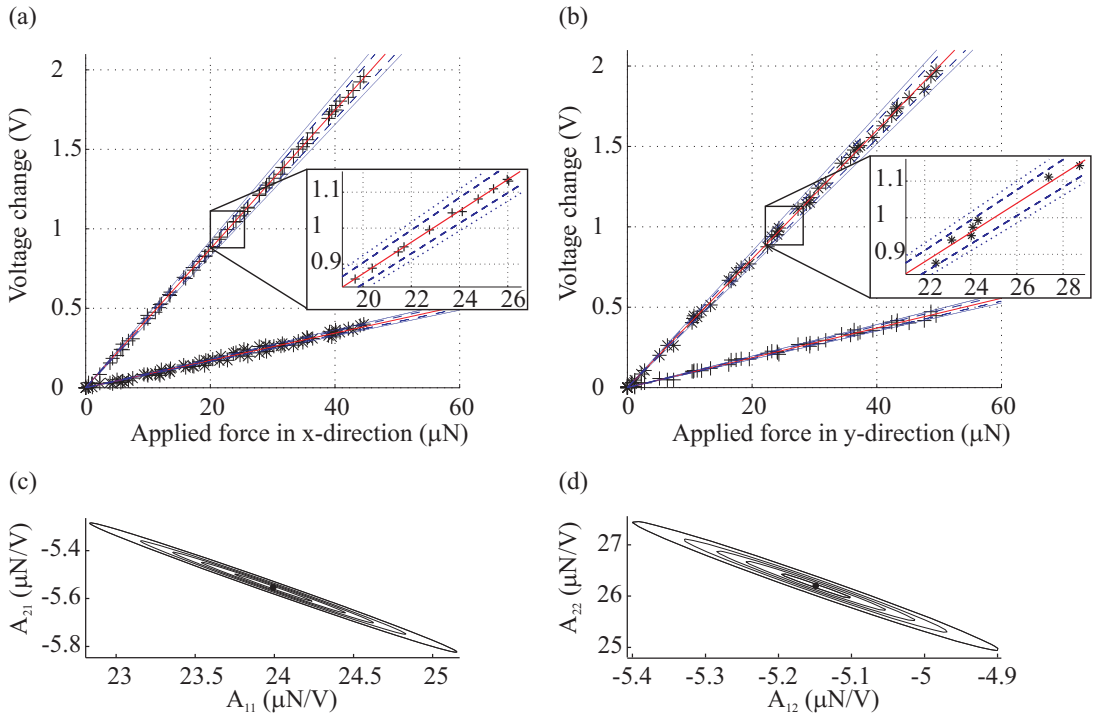

Fig. 31: Calibration results of the two-axis MEMS-based microforce sensor (tensile tester) consisting of the calibration data (+,*) as well as the best fit (-), 68% (--), and 95% (..) coverage intervals of the calibration curve in (a) the x-direction and (b) the y-direction, and contour lines of the multivariate PDF of the calibration coefficients in (c) $\boldsymbol{A}_x$ and (d) $\boldsymbol{A}_y$ for coverage probabilities of 10%, 30%, 50%, 70% and 90%.

multiple times (h) until all the results have stabilized as described in Section 3.4.

$$\boldsymbol{Fc}_i = \begin{bmatrix} Fx_{1,i} & \cdots & Fx_{N,i} & 0 & \cdots & 0 \\ 0 & \cdots & 0 & Fy_{N+1,i} & \cdots & Fy_{2\cdot N,i} \end{bmatrix}^T \tag{3.12}$$

$$\boldsymbol{Vc}_i = \begin{bmatrix} Vx_{1,i} & \cdots & Vx_{N,i} & Vx_{N+1,i} & \cdots & Vx_{2\cdot N,i} \\ Vy_{1,i} & \cdots & Vy_{N,i} & Vy_{N+1,i} & \cdots & Vy_{2\cdot N,i} \end{bmatrix}^T \tag{3.13}$$

$$\boldsymbol{Fc}_i = \boldsymbol{Vc}_i \cdot \hat{\boldsymbol{A}}^{2x2} + \boldsymbol{r}_{i,\min} = \boldsymbol{Vc}_i \cdot \left[\hat{\boldsymbol{A}}_x^{\,2x1} \quad \hat{\boldsymbol{A}}_y^{\,2x1} \right] + \boldsymbol{r}_{i,\min} \tag{3.14}$$

$$\hat{\boldsymbol{A}}_i^{2x2} = \left(\boldsymbol{Vc}_i^{\,T} \cdot \boldsymbol{Vc}_i \right)^{-1} \cdot \boldsymbol{Vc}_i^{\,T} \cdot \boldsymbol{Fc}_i \tag{3.15}$$

The best estimate of the calibration matrix (from all the $h \cdot M$ realizations), the standard uncertainties, the correlation coefficients (no correlation between $\hat{\boldsymbol{A}}_x$ and $\hat{\boldsymbol{A}}_y$) and the expansion coefficients are shown in Table 10 and the contour lines of the multivariate PDF of the calibration coefficients are shown in Fig. 31(c) and (d).

Table 10: Calibration and uncertainty analysis results: two-axis MEMS-based microforce sensor (tensile tester)

Input range (μN)	
Fx	±66.5
Fy	±70.5
Output range (V)	
Vx & *Vy*	0 – 4.5
Calibration matrix $\hat{\boldsymbol{A}}$ (μN/V)	$\begin{pmatrix} 23.99 & -5.15 \\ -5.55 & 26.20 \end{pmatrix}$
Standard uncertainty $u(\hat{\boldsymbol{A}})$ (μN/V)	$\begin{pmatrix} 0.54 & 0.12 \\ 0.13 & 0.59 \end{pmatrix}$
Correlation coefficients	
$r_{11\text{-}21}$	-0.995
$r_{21\text{-}22}$	-0.989
Expansion coefficient k_p for	
$p1 = 0.68$	1.50
$p2 = 0.95$	2.46
# MCM iterations: $h \cdot M$	$4.14 \cdot 10^6$
u_{Noise} at 10 Hz (μN)	
PDF: normal	
Fx	0.06
Fy	0.1
u_{Drift} (t = 30s) (μN)	
PDF: normal	
Fx	0.04
Fy	0.05
C_{int} MS3110 (pF) (x & y)	2
Gain MS3110 (x & y)	2

For the calibration of the full three-axis microforce sensor presented in Section 2.5, the same approach is used, where the reference force is applied sequentially along all the three sensitive directions while recording the output voltages. The results of the three-axis sensor calibration are presented together with its tuning capabilities in Section 3.8.

3.7 Calibration of the Multi-Axis Position Feedback Sensors

The relationchip between the output voltages and the position of the end effector arms of the tensile tester is also unknown, and must be found by calibration. For the actuated arm a position feedbeck sensor is integrated into each of the two orthogonally alinged acutuators, whereas in the force-sensing arm, the ouput of the force sensor can be correlated with the movments of its end effector. In order to calibrate the position feedback sensors of the actuated as well as the force-sensing end effector arms, their positions need to be measured by other means and compared with their output voltage signals. A microscope (A-ZOOM, Signatone Corp.) with an attached camera (A622f, Basler AG) which has been precalibrated using an optical target (1951 USAF Resolution Targets, Edmund Optics Inc.), is used to visually measure the position changes of the end effectors. High magnification pictures are taken at each calibration step and are analyzed using a visual rigid body tracker to extract the relative movement of the end effector arms.

The rigid body tracker is based on the fitting of a geometrical model of each of the end effector arms onto the images taken during the calibration using the least squares method, as shown in Fig. 32. The position of each of the end effector tips can be extracted from each image. The results are correlated with the output voltages measured at the instant in which the corresponding picture was taken. More details about the visual rigid body tracker can be found in [65]. A prerequisite for the accurate tracking of the end effectors is knowledge of the pixel size in the image of the camera. Thus multiple pictures of a visual target are taken prior to calibration. By measuring the distance between the lines of the optical grid over the entire field of view, the pixel size can be measured. Thousands of measurements of the pixel size were taken (horizontally and vertically), justifying the use of a normal distribution to describe its uncertainty.

For the calibration of the actuated end effector arm, the relationship between the output voltages of the actuator feedback sensors and the position of the end effector is calibrated by subsequent actuation in the x- and y-direction. Voltage ramps from 0 – 120 V and vice versa are applied, first to the positive and the then to the negative actuation direction electrodes (Vp+ or

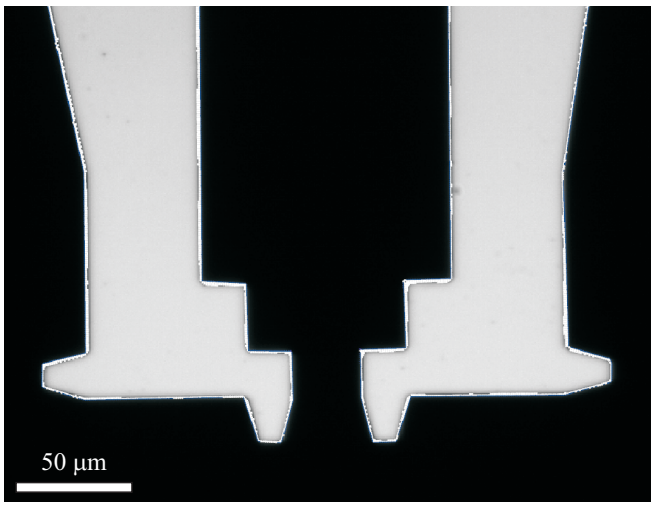

Fig. 32: Microscope picture of the tensile tester's end effectors with the geometrical model fitted to its outline, used for the visual rigid body tracking.

Vn+) in each axis. The output voltages of the two feedback sensors as well as the position given by the visual tracker are recorded and shown in Fig. 33(a) and (c) for the actuator calibration in the x-direction and in Fig. 33(b) and (d) for the y-direction. Clearly there is no significant hysteresis observable in the actuator's characteristics, since the increasing and decreasing positions during the actuator calibration cycles overlap. Similar relationships are found for the force-sensing end effector arm calibration. In the case of the force sensor position feedback calibration, the movements are induced by the reference-force sensor during force calibration (Section 3.6).

To calculate the calibration matrix and its uncertainties, the adaptive MCM described in the previous section is used. For the position sensor calibration the uncertainty due to drift and noise in the sensor output voltages, as defined by (3.8) and (3.10), as well as the uncertainties related to the root mean square error between the calibration data and the linear fit, are represented by normal distributions. Additionally, uncertainties related to the visual position measurement of the end effectors by the rigid body tracker need to be considered. These uncertainties can be separated into uncertainties from the visual tracker and the pixel size measurement (shown earlier). By sampling the position given by the visual tracker without moving the end effectors, the uncertainties due to the visual tracker can be separated into drift and noise described by (3.8) and (3.10) and are characterized by normal distributions. The PDFs of all sources of uncertainty are again combined to a joint PDF for each calibration data point out of which – during the adaptive multivariate MCM – $h \cdot M$ calibration data sets are created by random sampling. As described by (3.12) – (3.15), $h \cdot M$ sets of the calibration matrices can be calculated, out of

which the best estimate as well as the other results describing its uncertainty and the correlation can be found. The results for the calibration of the actuator are shown in Table 11 as well as in Fig. 33.

The nondiagonal entries in the calibration matrix are almost zero, indicating almost

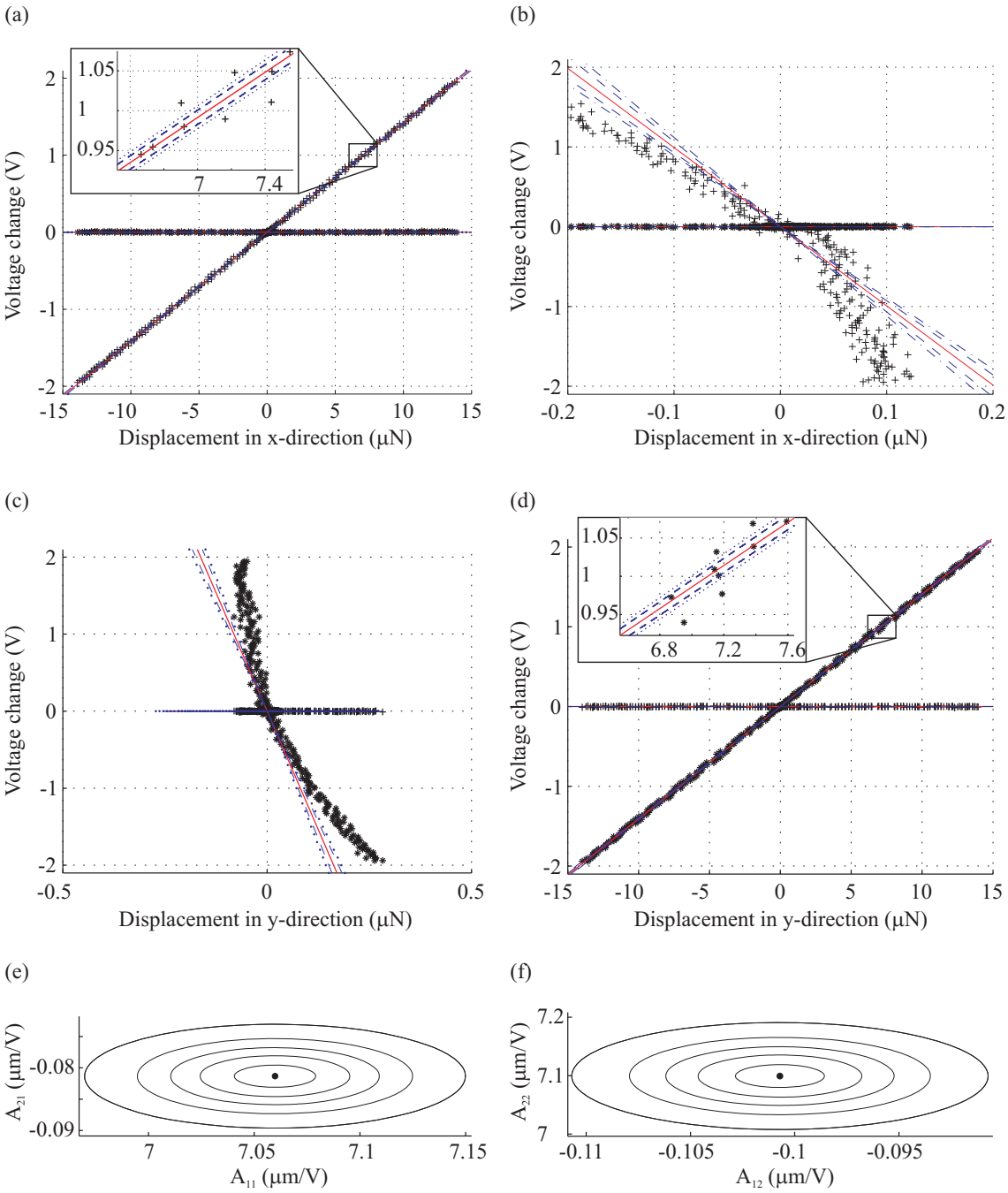

Fig. 33: Calibration results of the tensile tester's two-axis position feedback sensor in the actuated arm consisting of the calibration data (+,*) as well as the best fit (-), 68% (--), and 95% (..) coverage intervals of the calibration curve (a, c) in the x-direction and (b, d) in the y-direction, contour lines of the multivariate PDF of the calibration coefficients in (e) $\boldsymbol{A}_x$ and (f) $\boldsymbol{A}_y$ for coverage probabilities of 10%, 30%, 50%, 70% and 90%.

completely independent movement in the x- and y-directions. However, as can be seen in Fig. 33(b) and (c), a significant nonlinearity in the nondiagonal components of the calibration matrix can be detected. The error due to this nonlinearity is characterized by an additional uncertainty with a rectangular distribution, defined by a lower and upper limit.

The results of the actuator position feedback and the force sensor position feedback calibration are summarized in Table 11. Together with the results presented in Table 10, these characteristics can be used to make force as well as position predictions along two axes from the four output voltages of the tensile tester. To calculate the uncertainties of the position and force predictions, the uncertainties in the calibration matrices and in the output voltages (as well as the nonlinearity) need to be taken into account.

Table 11: Calibration and uncertainty analysis results: two-axis position feedback sensors in the microtensile tester

Sensor type	Position feedback on force sensor	Position feedback on actuator
Input range (μm)		
Dx	±2.2	±16.1
Dy	±1.1	±16.2
Output range (V)		
Vx & *Vy*	0 – 4.5	0 – 4.5
Calibration matrix $\hat{\boldsymbol{A}}$ (μm/V)	$\begin{pmatrix} 0.93 & 0.12 \\ -0.03 & 0.36 \end{pmatrix}$	$\begin{pmatrix} 7.06 & -0.10 \\ -0.08 & 7.10 \end{pmatrix}$
Standard uncertainty $u(\hat{\boldsymbol{A}})$ (μm/V)	$\begin{pmatrix} 0.02 & 0.01 \\ 0.02 & 0.01 \end{pmatrix}$	$\begin{pmatrix} 0.04 & 0.01 \\ 0.01 & 0.04 \end{pmatrix}$
Correlation coefficients		
$r_{11\text{-}21}$	-0.412	-0.001
$r_{21\text{-}22}$	-0.408	-0.001
Expansion coefficient k_p for		
$p1 = 0.68$	1.50	1.51
$p2 = 0.95$	2.45	2.45
# MCM iterations: $h \cdot M$	$4.14 \cdot 10^6$	$3.64 \cdot 10^6$
u_{Noise} at 10 Hz (μm)		
PDF: normal		
Dx	0.003	0.02
Dy	0.001	0.02
u_{Drift} (t = 30s) (μm)		
PDF: normal		
Dx	0.003	0.02
Dy	0.001	0.02
C_{int} MS3110 (pF) (x & y)	2	2
Gain MS3110 (x & y)	2	2
$u_{non\ linearity}$ (μm/V) PDF: rectangular	-	$\begin{pmatrix} 0 & 0.06 \\ 0.06 & 0 \end{pmatrix}$

3.8 Range Tunable Microforce Sensing

For most applications that require the measurements of microscale forces, it is challenging and often not intuitive to estimate the magnitude of the expected force range before actually measuring it. This is because, as the characteristic dimensions of a sample get smaller, the dominant forces acting on it change as shown in Fig. 34, rendering any experience in the estimation of forces useless. Therefore, designing a force sensor for a specific application is often an iterative and time-consuming process, since after the first measurement with such a sensor, it often needs to be redesigned for a different force range or used within only a percentage of its input range. For this reason, it would be desirable to have a force sensor, that

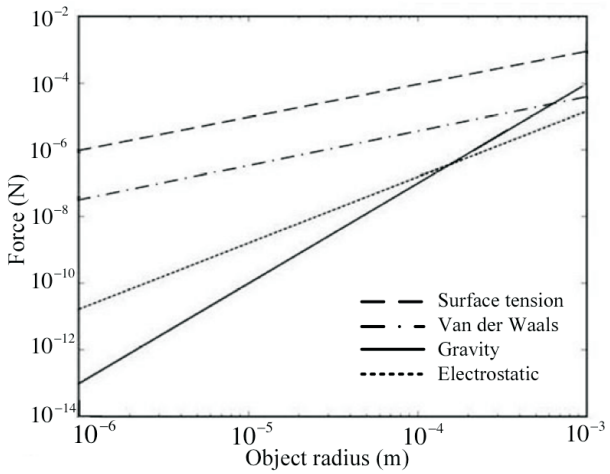

Fig. 34: Gravitational, electric, Van-der-Waals, and surface tension attractive forces between a sphere and a plane as a function of the their characteristic dimension [66].

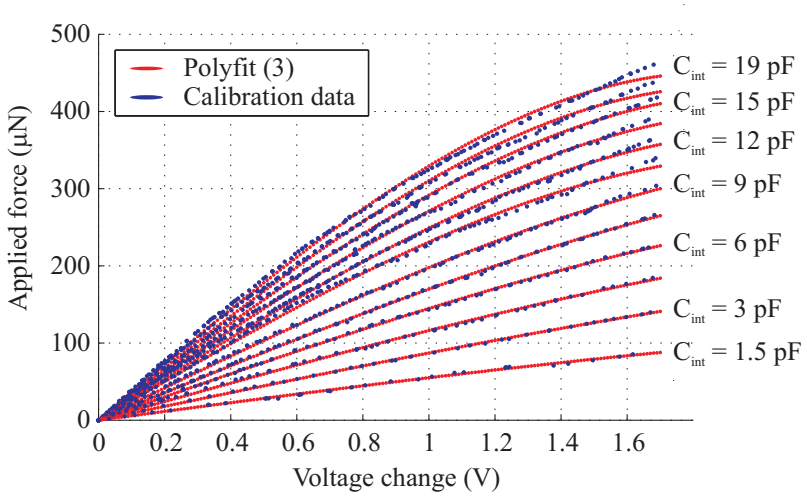

Fig. 35: Calibration curves for the single-axis MEMS-based capacitive microforce-sensing probe for varying C_{int}.

allows the tuning of its measurement range for a specific application while the measurements are taken, enabling a best possible signal-to-noise ratio.

As presented in Section 2.8, the capacity-to-voltage converter incorporates capabilities for the variation of some of its characteristic parameters, such as the integrator feedback capacitor C_{int} and the output amplifier gain *Gain* using a serial interface. The effect of varying C_{int} can be seen in Fig. 35 for the case of the single-axis capacitive microforce sensor presented in Section 2.4. As C_{int} is increased, the input range of the sensor increases, enabling the measurement of larger forces. The drawback of this approach is a decreasing linearity as the input range gets larger; this is related to the decreasing linearity of the differential capacitive measurement principle with the increasing displacement range as described in Section 2.2.

Not only do the input range, the calibration coefficients and the linearity of the sensor vary as C_{int} changes, but its characteristic uncertainties also vary with a changing C_{int}, such as the

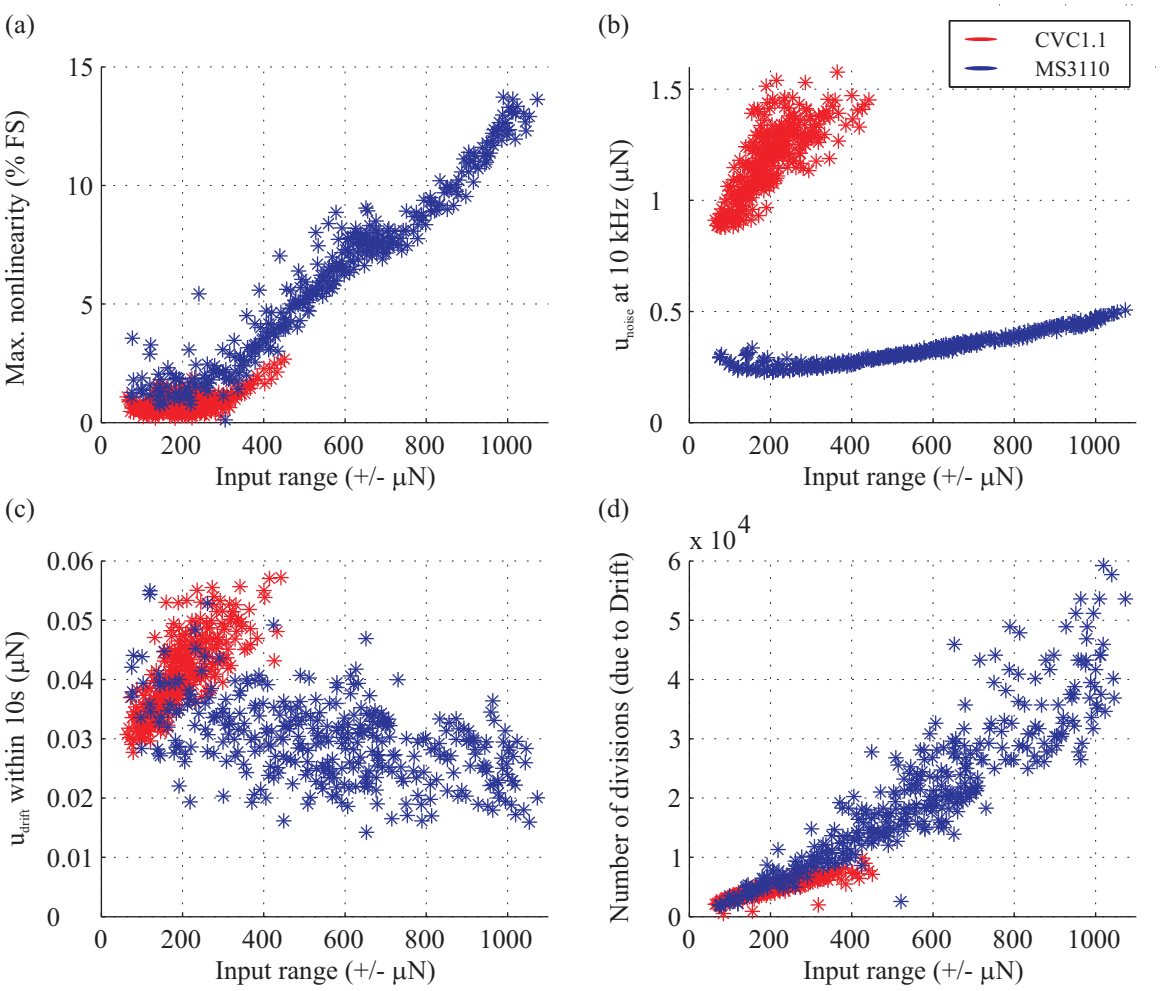

Fig. 36: Sensor characteristics for the single-axis MEMS-based capacitive microforce-sensing probe for varying C_{int} and *Gain*.

uncertainty due to signal noise (u_{noise}) and drift (u_{drift}). In Fig. 36 the results of the single-axis sensor characterization for varying C_{int} and *Gain* are presented. The results are shown for both capacity-to-voltage converters under investigation. For the MS3110, C_{int} has been varied from 1.5 pF to 19 pF in increments of 0.5 pF (C_{int} range [0, 20]) and the amplifier gain has been set to 2 or 4 (*Gain* range 2 or 4); for the CVC1.1, C_{int} has been varied from 1.6 pF to 5 pF in increments of 0.2 pF (C_{int} range [0, 6]) and the amplifier gain from 1.8 to 4 in increments of 0.2 (*Gain* range [1, 8]). For each combination of these two parameters the sensor has been calibrated five times, and the sensor's characteristic parameters have been recorded.

As the sensor's input range gets bigger, the nonlinearity increases as does the noise level of the sensor. For low frequency measurements (below ~100 Hz), the noise level can be reduced by averaging over a large number of samples; however, the uncertainty due to signal drift cannot be filtered out. To estimate the minimum detectable force change that can be measured,

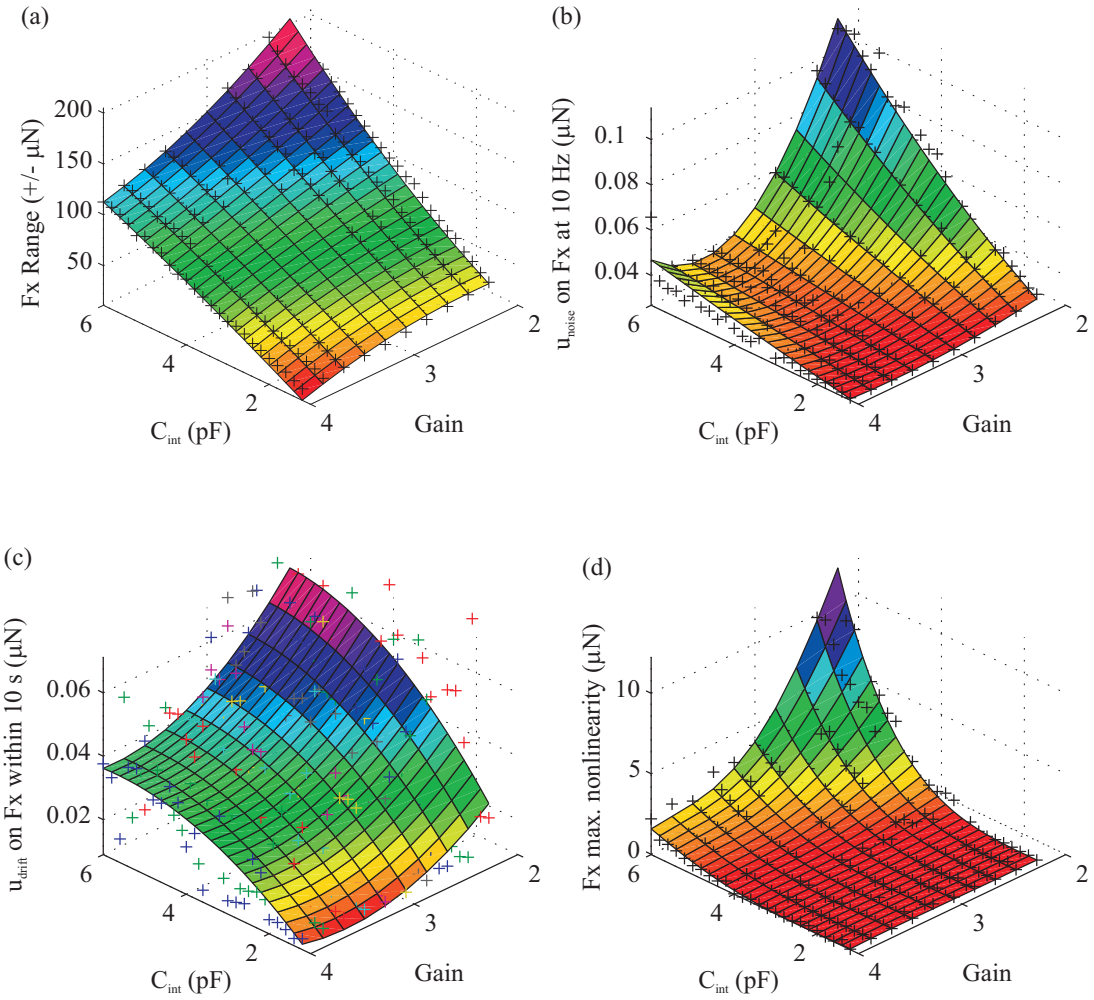

Fig. 37: Sensor characteristics for the three-axis MEMS-based capacitive microforce-sensing probe for varying C_{int} and *Gain*.

the uncertainty due to drift is the most relevant parameter. As shown in Fig. 36(d), the number of divisions of the sensing range increases with the range of the sensor, but at the same time results in greater nonlinearity. A compromise between acceptable nonlinearity and number of divisions needs to be made. Depending on the application of the sensor, a specific working point can be chosen. In cases where higher frequency forces (>100 Hz) must be measured, the influence of signal drift loses its dominance and the signal noise is the most relevant parameter. In this case, the smaller the input range of the sensor, the smaller the smallest detectable force. Comparing the two different CVCs, the MS3110 and the CVC1.1 (Fig. 36), it can be seen that the MS3110 converter offers a superior signal-to-noise ratio compared with the CVC1.1, making it the better choice for signal-axis microforce-sensing devices. For multi-axis sensing probes, however, only the CVC1.1 can be used, since multiple CVCs can be synchronized, enabling a multichannel capacitive readout.

The effect of sensor tuning on the sensor's characteristics in the case of the three-axis microforce-sensing probe presented in Section 2.5 is shown in Fig. 37. The sensor is

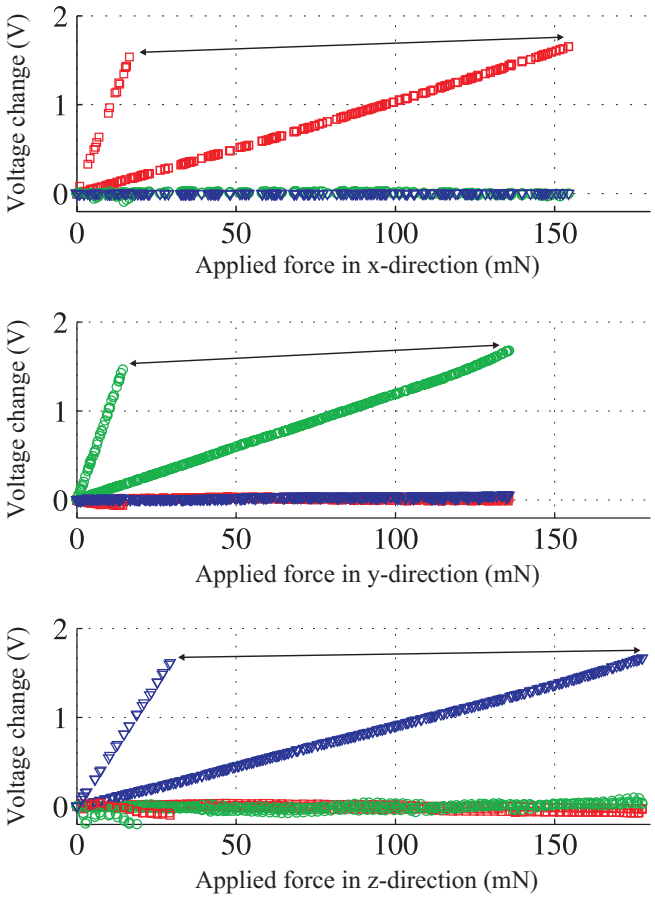

Fig. 38: The calibration curves of the three-axis MEMS-based microforce-sensing probe for the two different CVC settings indicated in Table 12 (squares indicate the raw calibration data V_x, circles V_y and triangles V_z).

characterized for 250 different settings of the capacity-to-voltage converter. The integrator capacitance C_{int} has been varied from 1.2 pF to 6.0 pF in increments of 0.2 pF and the amplifier gain *Gain* from 2.2 to 4.0 in increments of 0.2. For each combination of these two parameters the sensor was calibrated five times along each of its sensitive axes (x, y, z), the sensor characteristics were recorded, and the corresponding measurement uncertainties calculated. The resulting data sets for the x-direction – from a total of 3,750 calibrations – are shown in Fig. 37. The raw characterization data are shown as +, and the surface plots show a fit using a second-order polynomial in two variables, fitted using a least squares algorithm. The input range of the sensing probe can be changed from approximately ±20 μN to ±200μN with a corresponding resolution from 30 nN to 110 nN.

The calibration curves for the minimum and maximum sensor range are shown in Fig. 38. The arrows between the main components, which correlate to the diagonal elements in the calibration matrix, indicate the range in which the calibration curves can be adjusted. The corresponding characteristics are shown in Table 12. The nondiagonal entries in the calibration matrix are approximately zero, which can be verified in the calibration plots. This is an

Table 12: Three-axis MEMS-based capacitive microforce-sensing probe characteristics at two different CVC settings

Input range (μN)		
Fx	±22	±192
Fy	±20	±176
Fz	±31	±222
Output range (V)		
Vx, Vy, Vz	0 – 4.5	0 – 4.5
Calibration matrix $\hat{\boldsymbol{A}}$ (μN/V)	$\begin{pmatrix} 10.80 & 0.39 & -2.12 \\ 0.24 & 9.89 & 0.80 \\ -0.04 & -0.24 & 18.44 \end{pmatrix}$	$\begin{pmatrix} 95.61 & -0.42 & -0.20 \\ -1.11 & 83.43 & -3.50 \\ -2.12 & -0.02 & 109.18 \end{pmatrix}$
u_{Noise} at 10 Hz (μN)		
PDF: normal		
Fx	0.03	0.11
Fy	0.03	0.07
Fz	0.05	0.12
u_{Drift} (t = 10 s) (μN)		
PDF: normal		
Fx	0.01	0.04
Fy	0.01	0.04
Fz	0.02	0.07
Max. nonlinearity (μN)		
Fx	0	10.52
Fy	0.99	4.54
Fz	0	6.96
C_{int} (pF) (X, Y & Y)	1.2	6
Gain (X, Y & Y)	4	2.2
Mechanical resonant frequency (lowest) (Hz)	1,570	1,570

indication that the goal of mechanically decomposing the forces has been successfully realized. The results further indicate that the lower the input range of the sensor is tuned the smaller the forces that can be measured. Consequently, instead of redesigning the sensor, or using only a fraction of its input range, it can be tuned to the requirements of an application, which will result in an optimal signal-to-noise ratio and minimum nonlinearity. Since the sensor has been precalibrated for all the different settings of the CVC, it can be tuned as the measurements are taken without requiring recalibration.

3.9 Summary

Precise calibration of microforce-sensing tools is difficult for several reasons, including the lack of an accurate reference-force standard in the nanonewton range, lack of standardized calibration procedures and the need to apply known force vectors at precise positions and orientations on small and fragile microdevices.

In this chapter a methodology for the calibration of microforce sensors has been developed, which, in combination with the implementation of the latest advancement in the field of multivariate uncertainty analysis using an MCM, allows for SI-traceable force measurements in the nanonewton to micronewton range. By applying this methodology, the complete characterization of the microforce-sensing tools, which were introduced in the previous chapter, has been done, demonstrating the outstanding capabilities of these novel devices. Utilizing the range-tuning capabilities of the capacity-to-voltage converter, the simultaneous measurement of forces along three axes from tens of nanonewtons to hundreds of micronewtons with a single measuring probe could be achieved.

Next, the sensing tools are integrated into a complete measurement system, allowing for the automated micromechanical and microdimensional measurement of microscopic samples, which are presented in Chapter 5.

4 System Integration: Microcoordinate and Property Measuring Machine

With the advancement of MEMS technology new possibilities for the development of microfabricated tools, as presented in Chapter 2, have become possible, facilitating the mechanical investigation of microscopic samples by measuring their response to the localized application of small forces. At the same time, micropositioners with high-precision position feedback have reached a level of maturity to become commercially available in a variety of configurations and specifications. Together with a high-resolution microscope, the appropriate control electronics and software, these elements can be combined to create systems for automated micromechanical and dimensional metrology.

The configuration of such a system strongly depends on the application (compression, tensile, shear, indentation, scratchtesting, etc.) and the properties of the sample under investigation (stiffness, size, aspect ratio, breaking strength, etc.) as well as the environment in which these measurements take place (air, liquid, vacuum, etc.). In Fig. 39(a) a prototype of a microcoordinate and property measuring machine (μCPMM) is shown. It enables the simultaneous measurement of high aspect ratio, three-dimensional geometries of samples and their stiffness by performing compression tests. In Fig. 39(b) a micromechanical testing system is presented on an inverted microscope, enabling the high-resolution visualization of samples as

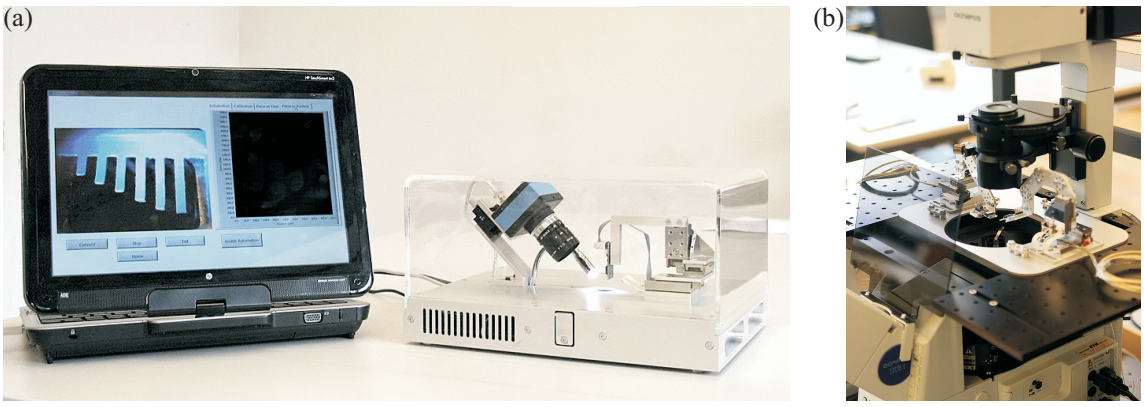

Fig. 39: (a) Microcoordinate and property measuring machine (μCPMM); (b) micromechanical testing system on inverted microscope.

they are investigated in liquids. Even in spite of the vast number of different applications imposing different requirements on the configuration of such a system, they typically consist of the five following modules:

End effector: The mechanical tool that physically interacts with the object under investigation, such as the capacitive microforce-sensing probes, including a first level of signal preconditioning and amplification, such as the capacity-to-voltage converter.

Micropositioner: A device to position the end effector or the sample within very fine limits. Generally a motorized micropositioner with submicrometer-resolution position feedback with multiple degrees of freedom is used. This enables an accurate positioning of the end effector on the sample as well as the automated measurement of the applied force as a function of the sample deformation.

Visualization system: Since the typical size of the samples under investigation is in the micrometer to millimeter range, the resolution of the human eye is not sufficient for an accurate positioning of the end effector to the measurement location on the sample. In addition, it is often desirable to visually observe the response of the sample as the measurement is performed. Depending on the sample size and the required environment (liquid, air, vacuum), different visualization systems are required, such as an optical microscope, inverted optical microscope or scanning electron microscope (SEM).

Electronics: For the control of the micropositioner, and the readout of its position feedback sensors as well as the end effector data, the appropriate control electronics and data acquisition hardware are required.

Software: A software interface allowing the user to control the measurement process, automating the lower level control of the micropositioner, data acquisition and visualization. Besides a higher achievable repeatability, system automation enables the measurement of larger amounts of data, which allows for a statistical treatment of the results.

Although the main focus of this thesis lies in the development of novel end effectors, their characterization and the assessment of measurement uncertainties, an introduction to one configuration of such a measurement system is presented.

The microcoordinate and property measuring machine (μCPMM) shown in Fig. 39(a) is

intended to perform fully automated micromechanical and dimensional measurements of samples up to 10 mm by 10 mm by 10 mm in size. It performs compression tests of the sample by approaching it vertically from the top, while measuring the force acting on the end effector's probe tip and measuring its position. By repeating this at regularly spaced locations over the sample the resulting data can be used to extract the topographical and the stiffness maps of the sample. The system consists of a three-axis micropositioner with optical position encoder (SL-2040, SmarAct GmbH), a CMOS camera (DFK 22BUC03, The Imaging Source LLC) with attached lens (C1614-MCKP, PENTAX Imaging Systems GmbH), a data acquisition card (NI 6009, National Instruments Corp.), a LED light source, and a Plexiglas enclosure, and is used on a vibration isolation table (Technical Manufacturing Corp.). A personal computer (TouchSmart tm2, Hewlett-Packard Co.) is used to interface and control the different components. Because the sample cannot be observed from the top since the sensor would obstruct the view, it is visualized under an angle of 45°. The technical specifications of the system are shown in Table 13. To enable the fully automated measurement of mechanical properties (stiffness) and sample topography, a control software with a graphical user interface has been developed (Labview 2009, National Instruments Corp.).

The most time consuming step in micromechanical measurements – incorporating the highest risk of damaging the fragile sensing probes – is the initial alignment to the sample. But by implementing the transformation from the two-dimensional camera image to the three-

Table 13: Technical specifications of the microcoordinate and property measuring machine (μCPMM)

Maximum sample dimensions	10 x 10 x 10	mm
Systems dimensions	225 x 275 x 155	mm
Camera		
Camera resolution	744 x 480	pixels
Maximum frame rate	60	fps
Field of view	10 x 10	mm
Angle of observation	45	°
Micropositioner		
Velocity (max.)	5	mm/s
Step width	50 – 500	nm
Displacement resolution	1	nm
Microforce-sensing probe		
(Single-axis capacitive microforce-sensing probe as presented in 2.4.)		
Force range	±230	μN
Force resolution	0.02	μN
Position resolution	0.07	nm
Stiffness	281	N/m

dimensional object space with the micropositioner's coordinate system, the initial sensor-sample alignment can be automated and controlled by selecting the area of interest on the camera image.

In addition to the 2-D image from the camera, further information for this transformation needs to be extracted using the sensing probe by performing an initial calibration. Assuming an approximately flat sample (with vertical dimension variations of less than, e.g., 300 µm), this 3-D transformation reduces to a 2-D transformation from the image plane to the object plane, which can be solved by a direct linear transformation (DLT) [67] described by (4.1) and (4.2), where u and v are the coordinates in the camera image plane (given in pixels) and x, y and z are coordinates in the object plane. The parameters L_1 through L_{11} are the parameters that describe the transformation and must be measured during a calibration step.

$$u = \frac{L_1 \cdot x + L_2 \cdot y + L_3 \cdot z + L_4}{L_9 \cdot x + L_{10} \cdot y + L_{11} \cdot z + 1} \tag{4.1}$$

$$v = \frac{L_5 \cdot x + L_6 \cdot y + L_7 \cdot z + L_8}{L_9 \cdot x + L_{10} \cdot y + L_{11} \cdot z + 1} \tag{4.2}$$

The coordinate system of the object plane, given by the coordinate system of the micropositioner, is zeroed on the height of the object plane, which is found by using the sensing probe on the micropositioner. Since a flat surface is assumed at z = 0, the transformation ((4.1) and (4.2)) can be simplified as L_3, L_7 and L_{11} do not need to be calculated. The remaining eight unknowns are now determined by driving the sensing probe to four calibration points (all of them at z = 0) and recording their real-world position given by the encoders of the

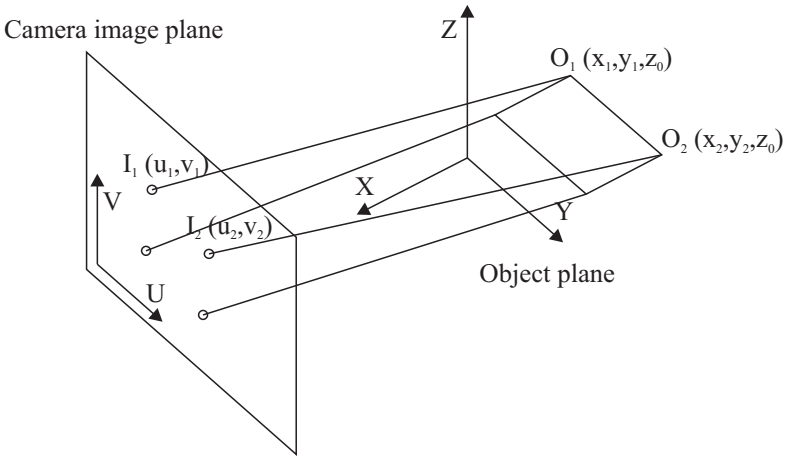

Fig. 40: Schematic of the direct linear transformation (DLT) from the camera image plane to the object plane.

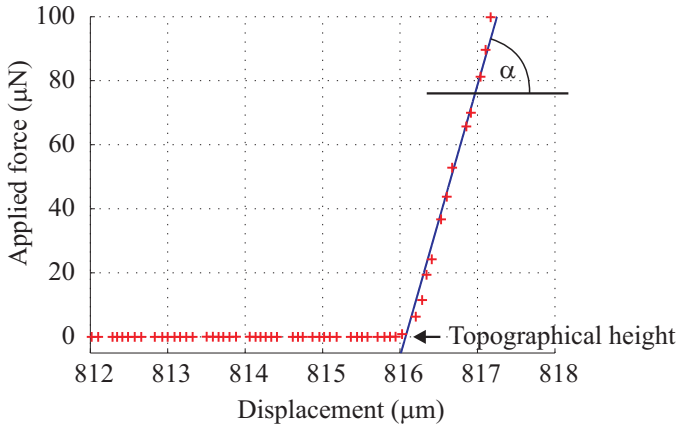

Fig. 41: Force versus position measurement data at a single sample location and its linear extrapolation to extract the topographical height and stiffness α of the sample at the current location.

micropositioner. The corresponding camera image coordinates of these calibration points are determined by selecting the location of the probe tip on the camera image for each of these four points. After u, v, x and y have been recorded for four points, the resulting system of equations can be solved for the unknown L_i. Using these transformations, the points that correspond to each of the pixels on the camera image on the object plane can be found and the sensing probe can be moved automatically to its desired location. To account for the maximum height variations of 300 µm, the sensing probe is moved and aligned at a search height of 300 µm from the z = 0 plane.

For the measurement of the topographical height and the stiffness of the sample at any location the sensing probe is vertically moved step wise toward the sample, while recording the position from the encoders of the micropositioner as well as the force from the sensing probe. Once the sensing probe touches the sample an increase in the force can be observed such as shown in Fig. 41. For a first-order approximation of the topography, the z-position of the first measurement point with a non-zero force can be used, introducing an uncertainty in the order of the step size used during the approach. For a more exact topographical measurement, the force versus position curve can be linearly extrapolated (only for linear elastic samples) to zero force as shown in Fig. 41. This allows for topographical measurement with virtually zero contact force and smaller measurement uncertainty than the step size, which is important for the accurate dimensional measurement of flexible samples. The stiffness of the sample can be simultaneously extracted from this measurement curve, given by the slope α of the linear approximation. By selecting a large number of measurement locations, which are defined by a grid laid over the entire sample, the automated measurement of both the sample topography and the stiffness map is possible.

In the next chapter the application of the different sensing tools in combination with different configurations of such a system are demonstrated to perform micromechanical or dimensional measurements on a variety of samples, such as the topography measurement of complex optical lenses and the stiffness versus cell-size relation of individual plant cells in their living states.

5 Measurement Applications

To illustrate the diverse range of uses of microforce-sensing tools, systems and methodologies for micromechanical and dimensional metrology, four different measurement applications are presented within this chapter.

The measurement of the complex, nonspherical topography of an optical lens with large inclination angles is demonstrated using the microforce sensor as a touch probe. The micromechanical characterization of biological samples such as a protein fiber is presented, and the utilization of the sensing probes to feel the interaction force with microorganisms is also addressed. Further is the combined micromechanical and dimensional measurement of individual plant cells in their living state – attached to the plant – demonstrated using the microtensile tester introduced in Section 2.6. To demonstrate the methodology used to perform SI-traceable measurements and to calculate the measurement uncertainties, the complete uncertainty analysis for the results obtained for the plant cell characterization is presented. For each of the applications a short explanation of its importance as well as a description of the measurement system configuration is given followed by the presentation of the results.

5.1 Topographical Measurements of Optical Lenses

The measurement of the three-dimensional topography of critical and complex components is an important step in the development and fabrication of various miniature, high-precision products. Optical or laser-based systems can quickly measure small visible features, but are limited to relatively flat surfaces and are incapable of measuring inside deep narrow holes or around feature edges such as undercuts. This is where touch probes integrated into a coordinate measuring machine (CMM) are the technology of choice. These typically large-scale systems are used to determine the geometry of complex objects by pushing the touch probe against the object, thereby detecting the location of contact.

Industrial systems are available such as the F25 (Fig. 2) by Carl Zeiss AG capable of measuring the geometry of three-dimensional objects with a minimum contact force of 500 μN

and a probe tip size as small as 50 µm. On the other side there are the AFMs, which allow for the measurement of dimensions way below single nanometers, but are limited to relatively flat surfaces with small step heights.

The three-axis microforce-sensing probe, introduced in Section 2.5 as the first microforce-sensing probe to measure submicronewton forces along three axes, is the key for the measurement of smaller three-dimensional geometries with a higher resolution than any other system. The reason for this higher dimensional resolution is linked to the relation between the force resolution of the sensing probe and the smallest possible probe tip size, since the smaller the probe tip, the higher the risk of damaging (e.g., penetrating) the sample at an equal contact force. By reducing this contact force, the probe tip size also can be made smaller without the risk of damaging the sample, and therefore allowing for a higher lateral, dimensional resolution.

Do demonstrate the utilization of the sensing probes for dimensional metrology, the system presented in Chapter 4 with an integrated single-axis microforce-sensing probe with attached tungsten wire with a tip radius of approximately 100 nm as shown in Fig. 42(a) is used. The three-dimensional topography of a complex, nonspherical optical lens is measured by laying a grid of 90 times 90 measurement points over the lens (resulting in 8,100 measurement locations). The resulting topographical map shown in Fig. 42(b) demonstrates the successful measurement of the three-dimensional geometry even on its steep sidewalls.

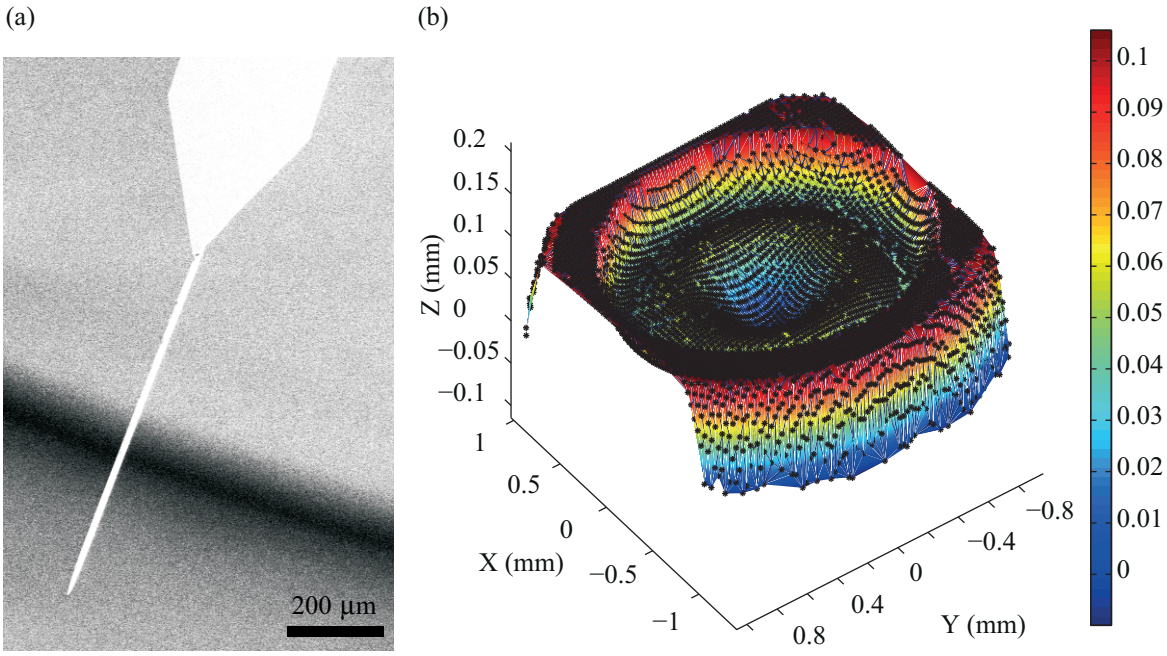

Fig. 42: (a) Photograph of the sensing probe used for coordinate measuring applications, realized by attaching a tungsten wire with tip radius of approximately 100 nm; (b) topographical map of an optical lens obtained using the µCPMM presented in Chapter 4.

5.2 The Stress-Versus-Strain Curves of Single Fibronectin Fibers

The mechanical properties of biological materials are tightly coupled with their physiological functions [68]. Therefore, the measurement of the mechanical properties can give insight into the functionalities of these materials. Silk fibers from web-spinning spiders, for example, perform optimally in air. They extend up to 3.7 times their unloaded length and contract with considerable hysteresis [69], allowing spiders to catch their prey. Fibrin fibers play an important role in early wound repair and likewise are reported to extend up to 4.3 [70] with an elastic modulus of 1 – 15 MPa [71]. Biological fibers designed to absorb mechanical stress are typically composed of large proteins. The mechanical stability of many fiber-forming proteins is controlled by a cluster of force-bearing backbone hydrogen bonds that stabilize their secondary structure, as for example in the case of fibronectin (Fn). Such modules rapidly unravel into extended peptide chains once a critical set of hydrogen bonds is broken [72], [73], [74].

The mechanical characterization of native Fn fibers, which are found in the extra cellular matrix (ECM) of cells and connective tissue, is difficult due to the interwoven nature of the fibrillar ECM and the considerable heterogeneity of fiber diameters. Fn fibrillogenesis can be activated by force, independent of whether the force originates from cell-generated tension [75], [76], [77] or is applied by other external means [78], [79], [80]. As an alternative to using native ECM fibers, Fn fibers with a more homogeneous diameter can be pulled with a needle from a droplet of concentrated Fn and deposited onto a substrate. As revealed by fluorescence resonance energy transfer (FRET), manually deposited and externally stretched Fn fibers are physiologically relevant models [80].

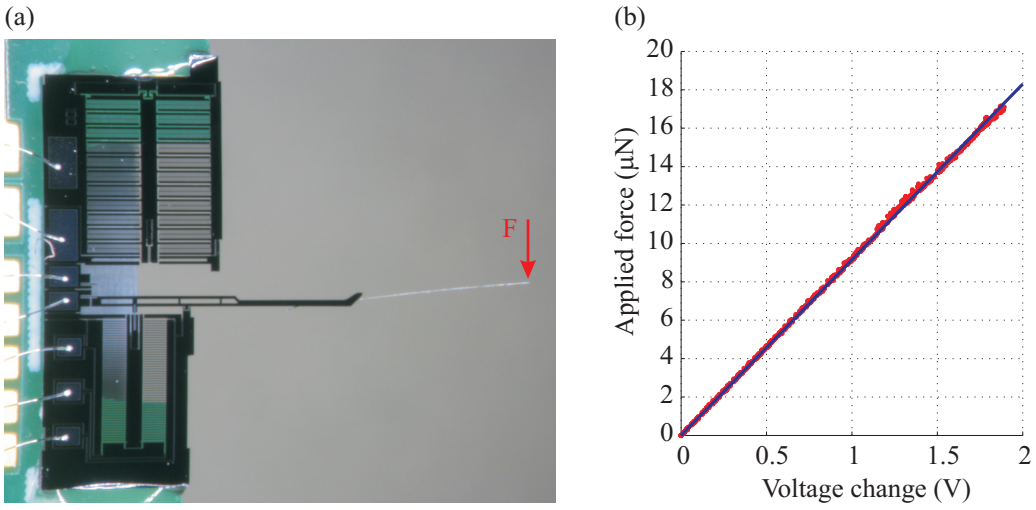

Fig. 43: Photograph of the single-axis MEMS-based microforce-sensing probe with attached tungsten wire, capable of measuring forces lateral to its probe and (b) its calibration data and linear fit.

For the mechanical characterization of the Fn fibers, the fibers were deposited across the trenches of a microfabricated PDMS grid and, before the subsequent measurements, rehydrated in PBS buffer. For the visualization of the fibers in the buffer, the measurement setup is mounted on an inverted microscope (FV1000, Olympus Corp.). The Fn fibers are stretched using a microforce-sensing probe, mounted on a motorized micropositioner (MP-285, Sutter Instrument Co.). Due to the lack of position encoders, the extension of the fiber, as it is being stretched is measured optically by post-processing the pictures from the microscope. For this application a sensor with a very sharp probe is required that enables the measurement of forces perpendicular to the sensing probe as indicated in Fig. 43. Thus a microforce-sensing probe similar in the design to the two-axis microforce sensor presented in Section 2.5, offering measurement capabilities in the direction perpendicular to the probe, is used. The force-sensing arm of a microgripper with force feedback as presented in [45] is used, where the actuated arm has been removed. To enable a very sharp sensing probe, a tungsten wire with probe diameter of 10 µm and tip radius of approximately 100 nm was glued to the force-sensing arm using UV-curable glue as shown in Fig. 43(a). For the calibration of the output voltage change of the

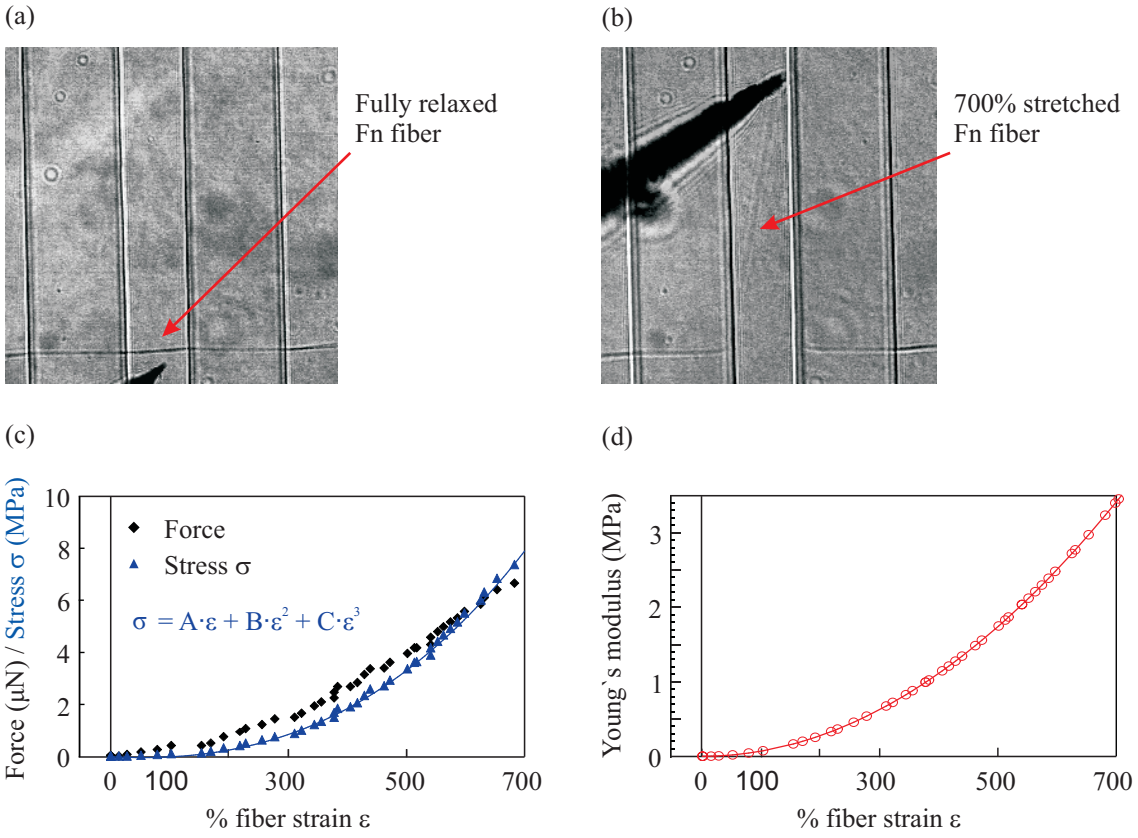

Fig. 44: (a), (b) Photographs and (c), (d) results of the stress-versus-strain curve measurement of a single Fn fiber with a diameter of 3.5 ± 0.2 µm suspended over a trench with a width of 30 µm.

sensor and the force applied to the tip of the tungsten wire, the setup for multi-axis force-sensor calibration as described in Section 3.6 is used. The single-axis microforce sensor as presented in Section 2.4 is used as a reference standard. The resulting calibration curve is shown in Fig. 43(b). The input range of the sensor is ±20.6 µN with a 1σ-resolution at 10 Hz of 15 nN.

For the measurement of the stress-versus-strain curves of the single Fn fibers, the sensing probe tip was first brought into contact with the Fn fiber and then displaced along the trenches (Fig. 44(a), (b)). The tensile force applied to strain the fiber, the calculated stress (force per unit cross sectional area of the Fn fiber), and the instantaneous Young's modulus (slope of the stress-versus-strain curve) are given as functions of the optically measured fiber extension for one representative fiber as shown in Fig. 44(c) and (d). To determine the cross-sectional area, the diameters of the fibers were measured optically at zero strain. When stretching the fibers, it was assumed that the fibers maintained constant volume and a uniform, circular diameter. The Young's modulus of single Fn fibers, shown in Fig. 44(d), is not constant as expected for linearly elastic materials. Instead, the stress-versus-strain curves are highly nonlinear, being soft (compliant) first, and turning rigid at high extensions. Young's modulus exhibited a small

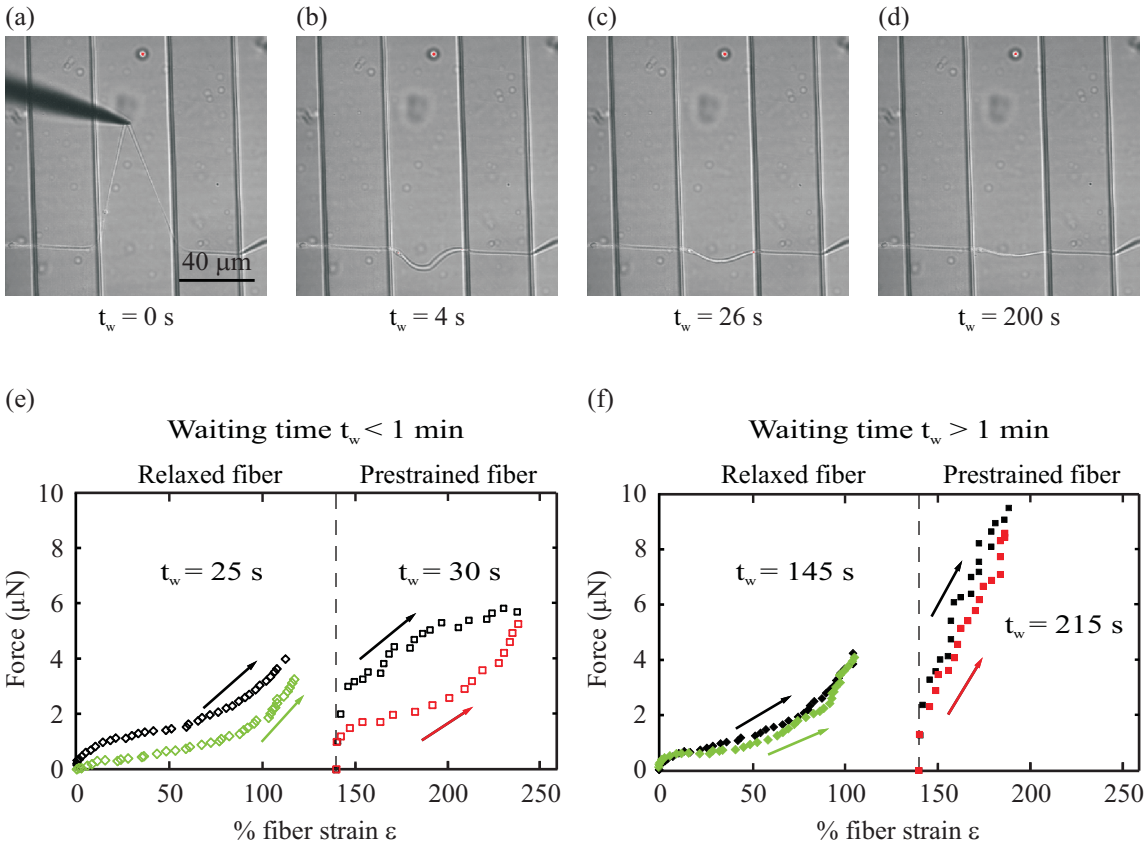

Fig. 45: (a) – (d) Photograph of a Fn fiber during its recovery from the extended state, (e), (f) results from the investigation of the mechanical property recovery after variable recovery periods t_w.

increase in the low strain regime, while increasing considerably once the fiber extension exceeded about 150% strain. Note that Young's modulus of single fibers changes orders of magnitude, from less than 100 kPa to several MPa from relaxed to highly stretched fiber.

As the tensile force is released, it appears, that fiber contraction and module refolding occurs. Therefore, measurements were made to investigate whether the fibers returned to their original lengths after stress release, and if so, how rapidly. Many materials deform plastically before failure; such plastic deformations involve irreversible slippage of molecules with respect to each other. The contour length of the fibers was measured multiple times after the fibers were released from the sensing probe tip. Immediately after release, the fibers have a sinuous appearance and then contract back to their original length as time progresses, as shown in Fig. 45(a) – (d). All investigated fibers returned back to their starting lengths after a recovery period of a few minutes, regardless of the state of extension. To determine whether a complete recovery of the mechanical properties occurred as well, the force versus strain curves of the same fibers were remeasured after a variable waiting period between each mechanical test, as shown in Fig. 45(c) and (d). When the waiting time between consecutive pulls was shorter than 1 min, the force versus strain curves showed considerable hysteresis, indicating, that the second fiber extension required significantly lower force to reach a given strain relative to the first pull. This occurred for both initially relaxed as well as prestrained fibers. Right after the fibers started to contract, they were initially more compliant than the original fibers. However, waiting for 1 min or more resulted in a recovery of their initial mechanical properties. This is a significant observation, since mechanical unfolding of Fn modules requires that clusters of force-bearing backbone hydrogen bonds are broken. A complete recovery of the mechanical strength of the fibers therefore implies that these critical hydrogen bonds can reform.

The mechanical investigation of single Fn fibers has been conducted in close collaboration with the Laboratory for Biologically Oriented Materials at ETH. Creation of the measurement system and software, calibration of the sensing probe as well as the preliminary testing on Fn fibers has been carried out as part of this work, while the measurement results presented here has been performed by Enrico Klotzsch from the Laboratory for Biologically Oriented Materials [81].

5.3 Measuring the Touch Sensitivity of Microorganisms

Touch sensation is one of our least understood senses, yet is vital for many biological processes such as locomotion and embryonic development. More generally, the conversion of mechanical

forces to an electrochemical signal is necessary for many functions, such as hearing and blood pressure regulation.

Microforce-sensing probes can be utilized for the quantitative measurement of the touch sensitivity of microorganisms, by measuring the force needed to result in a positive behavior response. Caenorhabditis elegans is an organism widely used to study the molecular basis of mechanotransduction and is therefore used for the purpose of this application. A micromechanical measurement setup similar to that used for the measurements of the stress-versus-strain curves of single fibronectin fibers presented, in Section 5.2, is used. The setup involves an inverted microscope (IX81, Olympus Corp.), a micropositioner (MP-285, Sutter Instrument Co.) and the lateral sensing probes with attached tungsten wire, as shown in Fig. 43. Four different strains of C. elegans have been investigated for their touch sensitivity – two strains with normal mechanosensitivity (N2 wild-type and HA1134) and two strains with reduced touch sensitivity (osm-9 and ocr-2). The worms were synchronized and grown at room temperature to obtain L4 animals, which were placed on an agar pad. The agar pad was placed on the motorized stage of the inverted microscope, enabling manual control of the pad with respect to the force probe, which was mounted on the micropositioner.

By placing the force sensor in the path of a worm, the threshold force for a behavioral response, indicated by the worm moving in the opposite direction, could be measured. Synchronized video and data were recorded. Every contact between the worm and probe was scored (response, no response) and the timestamp was recorded. The timestamps were used to automatically find the force values for the corresponding interaction. The results of 200

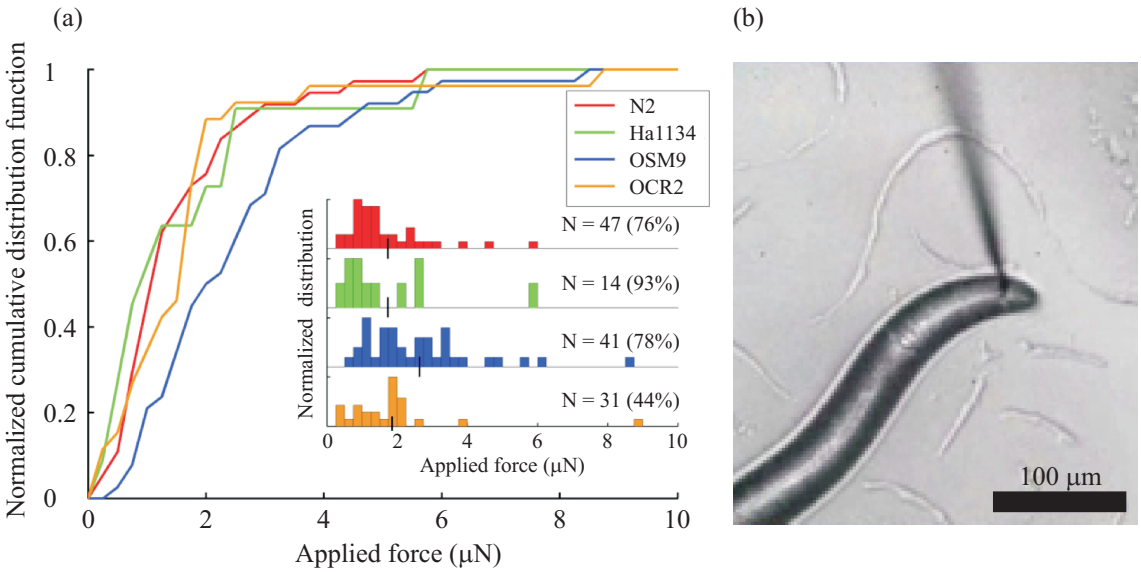

Fig. 46: (a) Results and (b) photograph of the touch sensitivity measurements on different C. elegans strains.

interactions with a total of 21 worms are presented in Fig. 46. The discreet cumulative force distribution and normalized discreet force distribution (inset) for events that yielded a positive behavioral response for each strain are depicted in Fig. 46(a). The mean force is noted by the black line in the inset figure. The number of positive responses measured and the positive response rates for each strain are noted in the histogram. Six, four, five and six animals were tested for N2, HA1134, osm-9 and ocr-2, respectively. The mean threshold force for the osm-9 animals (2.61 μN) was slightly greater than that of the other three strains. No significant difference was measured between the N2 wild type (1.70 μN), HA1134 (1.70 μN) and ocr-2 (1.83 μN) strains.

This application demonstrated the successful use of a microforce-sensing probe for measuring the threshold for touch sensation on microorganisms, providing a novel approach for the quantitative investigation of mechanotransduction.

The measurement of the touch sensation of C. elegans was conducted at ETH Zurich in close collaboration with Joey Doll from the Stanford Microsystems Lab. Development of the measurement system, software and the sensing probe calibration has been carried out as part of this work, while the measurement results presented here have been performed by Joey Doll [82].

5.4 Stiffness Measurement of Individual Petunia Trichome Cells

As the world's primary producer of food and energy, photosynthetic organisms are of vital importance to human society. Making up over 99% of the earth's biomass, photosynthetic organisms also have a major impact on the global climate. Consequently, understanding how plants grow is of fundamental importance. Numerous studies and models of plant growth have been made based on limited and mainly quantitative knowledge of their mechanical properties.

During the past few years, the focus in plant development biology has shifted from studying the organization of the whole body or individual organs toward the behavior of the smallest unit of the organism, the single cell [3]. Cell expansive growth is a mechanical process that balances internal and external stresses with the compliance to allow expansion. Various models to predict cell growth have been made, but to supply mathematical models with relevant and accurate input, quantitative values for a number of physical parameters need to be provided. Since educated guesses are often the only recourse [83], the aim of this application is to demonstrate the capabilities of the microtensile tester to quantitatively measure these properties in plant cells in their living states. This has the potential to provide the information needed to construct a new generation of mechanical models that are based on actual, measured properties.

The microtensile tester presented in Section 2.6 can be utilized for a wide range of applications in different fields, such as material science or mechanobiology. One of the key features of this device is its ability to be used as a compression tester. Much like the human hand, the gripper-like end effector design allows it to simply grasp an object, e.g., a cell in its living state, and “feel” its properties, such as its stiffness or size. The attachment of the sample without any degeneration is one of the biggest challenges in microtensile tests. This feature is demonstrated by measuring the mechanical properties of plant hairs (trichomes). These elongated epidermal plant cells are mechanically characterized while they are still attached to the living plant. The trichomes serve as an excellent model system to study various aspects of plant differentiation at the individual cell level, and are easily accessible because of their epidermal origin [3]. The glandular, non-branched multicellular trichomes from the wild type petunia (W115) plant, as shown in Fig. 47 and Fig. 49(a), are chosen as a sample. The goal is to measure the cell stiffness along one of the long inclining cells to find the relationship between the cell stiffness and its radial diameter. The tensile tester is mounted on a three-axis micropositioner with position encoders (SL-2040, SmarAct GmbH). The proper alignment of the tensile tester with the trichome cell is critical. Prior to the measurements, the end effectors are visually aligned at three locations along the cell. By interpolating between these locations, the trajectory along which the micropositioner will move the tensile tester during the automated measurement can be determined.

The stiffness of the trichome cell is measured by compressing the cell while measuring the force and the deformation, given by the sum of the displacements of the sensing and the actuating end effector. This is done in a fully automated fashion along the trichome cell over a length of 180 µm in 20 µm steps. At each measurement location the cell is compressed 10 times repeatedly. In Fig. 48, the 10 measurement curves from one of the nine measurement locations

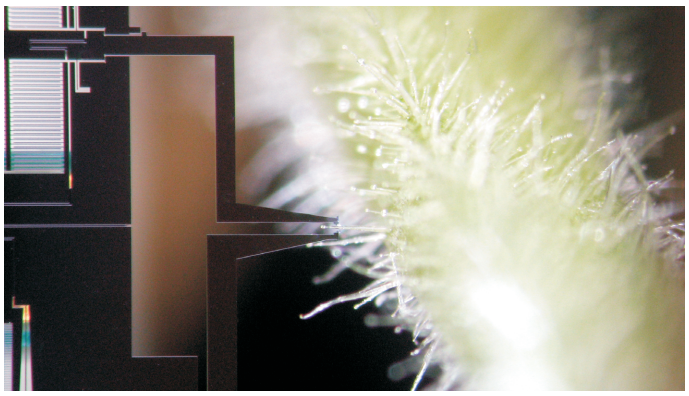

Fig. 47: Photography of the two-axis microtensile tester aligned with a trichome of the petunia plant (W115).

are shown. The measurements begin with the fully opened end effectors (right side in Fig. 48). Then they are slowly closed at an average speed of 0.5 µm/s until the force sensor is saturated (upper curve in Fig. 48). Subsequently they are opened again to their initial position, shown in the lower curve in Fig. 48. The large negative force on the lower curve is the adhesion force of the cell to the end effectors during the opening and indicates that the cell is under tension. The slow decrease of the adhesion force as the end effectors are separated is assumed to be related to the sticky secretion with which these glandular trichomes are covered. The extensive interpretation of the measurement data and the description of the material model are not within the scope of this work. However, in order to give an overview of the results, a simplified description of the cell using a linear model is shown in Fig. 48 and Fig. 49.

Between an upper and a lower limit of the force, shown in Fig. 48, the force-versus-end-effector opening can be reasonably approximated using a liner model, shown with a least squares fit (black dashed lines). The cell stiffness is defined as the slope of these curves. Defining the cell's radial diameter is difficult since it is not clear where the first contact with the cell occurred. This is suspected to be related to the adhesion forces generated by the secretion on the cell. Therefore, pseudo radial cell diameters D^+ and D^- are defined by linearly extrapolating the linear regime of the force-versus-end-effector opening curve to zero force (D^+ for the compression and D^- for the release of the cell). An overview of the measurement results is shown in Fig. 49(b) and (c). The best estimate for the stiffness and cell diameter from a single measurement is indicated by x. The cross in each measurement point shows the standard

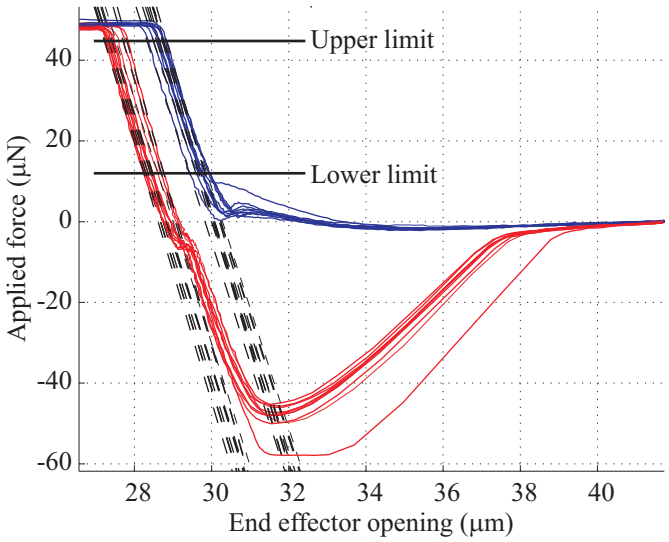

Fig. 48: All 10 measurement curves on one of the nine measurement locations on the trichome cell: The upper curves are the results from compressing and the lower curves are the results from releasing the cell. The dashed lines are linear fits to the data between the upper and the lower limit.

uncertainty for the stiffness as well as for the cell diameter calculated using the MCM with $M = 4.02 \cdot 10^5$ Monte Carlo trials. The solid line through all the data indicates the best estimate of the least squares fit, describing the relationship between the cell stiffness and the pseudo radial cell diameter. The dashed and dotted lines are the 68% and 95% coverage intervals.

For the purposes of this thesis, the scope of this application was to demonstrate the

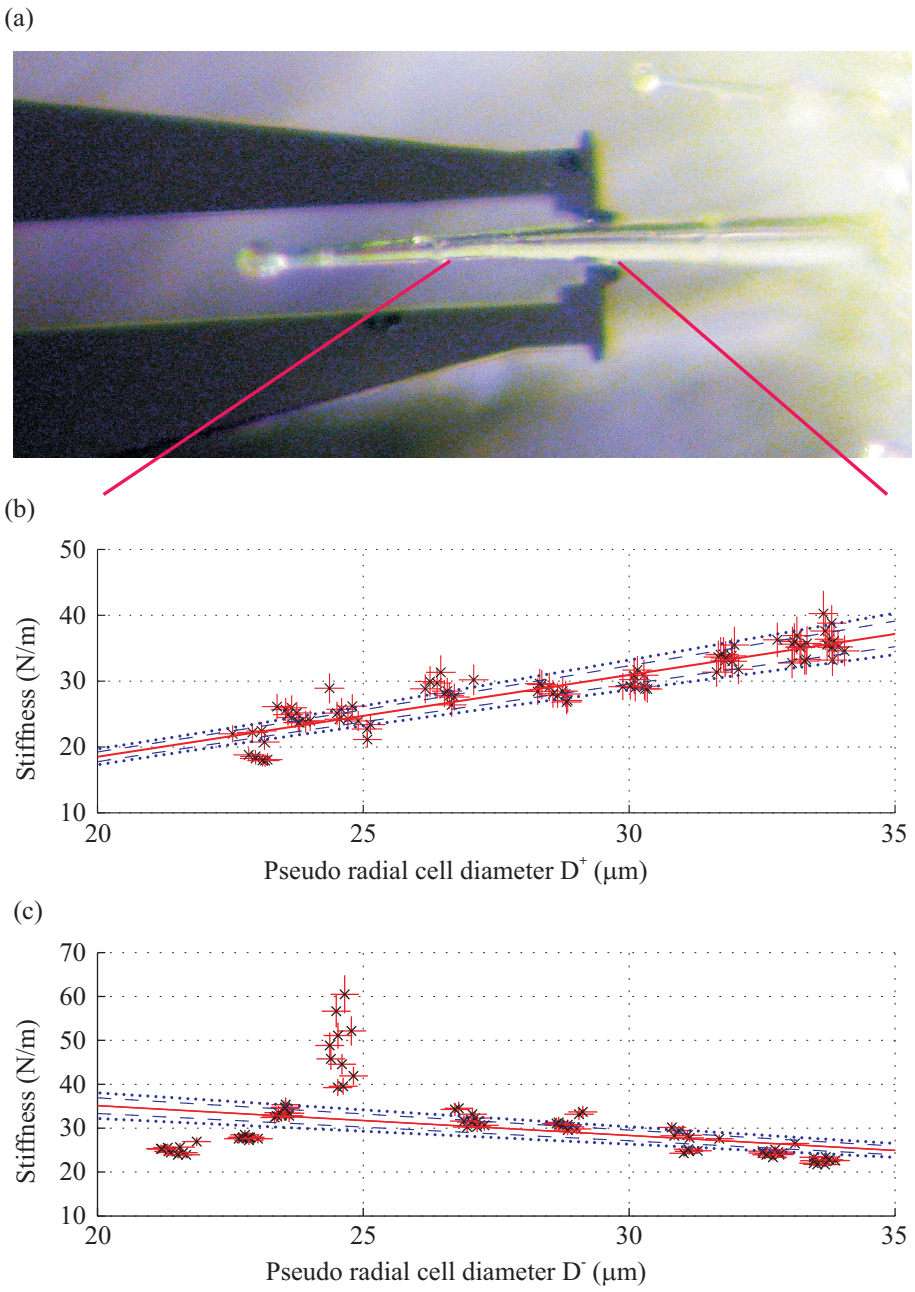

Fig. 49: Measurement results of the trichome cell characterization: (a) The microtensile tester's end effectors aligned with the trichome indicating the region of the stiffness measurements, (b) results of the stiffness-versus-cell-diameter measurement for the compression of the cell, (c) results of the stiffness-versus-cell-diameter measurement for the releasing of the cell.

performance of the tensile/compression tester. The interpretation of the results, especially the discrepancy between the compression and the relaxing characteristics, must be further investigated with more measurements and a variety of different material models.

This application demonstrates the ability of the microtensile tester to perform micromechanical measurement as well as dimensional measurement on a sample, attached to a living organism, by simply grasping it.

5.5 Summary

The application of the microforce-sensing tools and methodologies presented in this chapter should demonstrate how they can help to investigate the properties and the functionalities of microscopic samples.

The measurement of the stress-versus-strain curves of single Fibronectin fibers has indicated the mechanical unfolding of Fibronectin modules and the breaking of their force-bearing hydrogen bonds. With the complete recovery of their mechanical strength, evidence for the reversible reforming of these critical hydrogen bonds is given.

Touch sensation – the conversion of mechanical forces to electrochemical signals – is one of our least understood senses. It has been demonstrated that microforce-sensing probes can be used for the measurement of the threshold for touch sensation on microorganisms, providing a novel approach for the quantitative investigation of mechanotransduction.

Using the microtensile tester, the micromechanical and dimensional measurement of plant cells in their living state, attached to the plant, has been demonstrated by simply grasping an individual cell. This approach can be used to measure the mechanical properties of cells in their living states, necessary for the construction of a new generation of mechanical models that are based on actual, measured properties.

Beyond the numerous research applications for these microforce-sensing tools, there is great potential for industrial applications such as quality control of microfabricated structures. This has been demonstrated through their use as high-resolution touch probes, for the measurement of the three-dimensional topography of an optical lens.

These four applications demonstrate, how microforce-sensing tools and methodologies developed in this thesis will have a great impact on various fields of research and industrial markets.

6 Summary and Contributions

The increasing interest in ever-smaller samples and the industrial trend toward miniaturization has created a need for novel, high-precision metrological tools for their investigation and testing. Measuring the mechanical characteristics of samples by applying a force can give insights into its structure or functionalities since, e.g., the mechanical properties of biological materials are tightly coupled to their physiological functions. For the investigation of micrometer-sized samples, forces in the nanonewton to micronewton range need to be measured. With the advancement of MEMS technology, new opportunities for the development of microfabricated force sensors that can overcome the limitations of current solutions have become possible, such as the lateral motions of cantilever-based systems due to their bending characteristics or the limitation to single-axis measurements in the nanonewton range.

Despite the need for novel metrological tools, no standardized methodologies for the calibration of these tools and the calculation of their measurement uncertainty exist, as an SI-traceable reference standard in the nanonewton range, such as miniature weights, are unavailable. The smallest available SI-traceable mass artifact in the market is 1 mg, which corresponds to approximately 10 μN. Typically microforce sensors, such as AFMs, are therefore calibrated based on a model of the sensor, having the disadvantage of unknown accuracy, since the results are not traceable back to SI units.

Given these limitations, numerous applications in research and industry are not accessible for quantitative measurements and educated guesses are often the only recourse. Motivated by this problem, the work within this thesis has been focused and its contributions can be subdivided into following three main areas.

Microforce-Sensing Tools

The limiting factor for the development of standardized micromechanical testing systems or microcoordinate measuring machines is the unavailability of microforce-sensing probes that can measure forces down to the nanonewton level along multiple axes. Thus the first three-axis microforce-sensing probe was designed, fabricated and characterized, enabling the measurement of forces up to ±200 μN along all its sensitive directions with a resolution as low as 30 nN. And

by combining capacitive sensing as well as electrostatic actuation elements on a single chip, the first monolithically integrated, two-axis MEMS-based microtensile tester has been developed, allowing the direct measurement of the mechanical as well as electrical properties of a sample in two directions. Due to the gripper-like design and the symmetrical force and displacement range, the tensile tester also can be used as a compression tester, allowing for the mechanical characterization of samples by simply grasping them.

The reason for the limited availability of multi-axis sensors for in- and out-of-plane sensing is related to the complexity of the different microfabrication approaches presented in literature. Therefore a novel microfabrication process solely based on a combination of photolithography and dry-etching steps has been developed, enabling a major reduction of the fabricational complexity of multi-axis in- and out-of-plane sensors and actuators.

Because of the limited range in which these sensing tools typically can operate, they are most commonly custom designed for each application. To enable their wide utilization without requiring a redesign when used in a different force range, a method for tuning the input range while taking measurements is incorporated into the sensors, enabling the best possible characteristics for a wide range of applications.

Methodology for the Calibration and Uncertainty Analysis of Microforce-Sensing Tools

Driven by the unavailability of an SI-traceable reference standard in the nanonewton range and the fact that none of the approaches by any of the National Metrology Institutes to realize a primary small-force reference standard has matured enough to be implemented, a different approach for the calibration of microforce-sensing tools had to be found.

A combination of the highly accurate, compensated SI-traceable semi-microbalance, deadweights and a custom macroscale reference sensor was used. With this blend of tools it was possible to benefit from the advantages of the mature microbalance technology while avoiding their limitations, such as their high stiffness and slow output frequencies. In combination with the implementation of the latest advancements in the field of multivariate uncertainty analysis using a Monte Carlo method, SI-traceable microforce calibration in the nanonewton to micronewton range became achievable.

Although promising results obtained by National Metrology Institutes around the world have been indicating the imminent availability of an SI-traceable primary realization of forces below the 10 μN limit, a suitable transfer standard, which will allows the dissemination of this primary standard to industrial standards or instruments, is currently not available. As a first in literature, the utilization of a single-axis capacitive microforce-sensing probe in a four-flexure

configuration has been evaluated as the most suitable candidate for a transfer standard. Its parallel deflection characteristic, compact size and the demonstrated low cross sensitivity to off-axis forces and changes in environmental conditions is making this probe a close to ideal candidate.

System Integration and Demonstration

The developed microforce-sensing tools and methodologies have been implemented into a variety of complete, automated measurement systems, which can be used for a great number of different applications enabling the measurement of properties for which only qualitative results exist to date.

The mechanical characterization of Fibronectin fibers has indicated the reversible breakage of their hydrogen-bond backbones. A methodology for the quantitative investigation of mechanotransduction by measuring the touch sensation of microorganisms has been developed. By using the microtensile tester, the micromechanical measurement of the properties of individual plant cells, attached to the living plant, has been demonstrated, providing a method for extracting the properties needed to construct a new generation of mechanistic models of plant growth, based on actual measured properties.

As indicated by these applications, there is evidence that the contributions made in the field of micromechanical and microdimensional metrology will open up new possibilities in different fields of research, where quantitative insight into the mechanics of small samples is needed. Further, these advancements will – following the miniaturization trend – enable the development of standardized equipment, such as micromechanical testing systems and microcoordinate measuring machines, taking the next step toward the measurement of smaller forces and dimensions.

7 References

[1] U.S. Congress Office of Technology Assessment, "Miniaturization technologies," *U.S. Government Printing Office,* Nov 1991.

[2] E. F. Schumacher, *Small is beautiful. A study of economics as if people mattered*. London, UK, 1993.

[3] M. Hulskamp, "Plant trichomes: A model for cell differentiation," *Nature Reviews Molecular Cell Biology,* vol. 5, pp. 471-480, Jun 2004.

[4] P. Ruther, J. Bartholomeyczik, A. Trautmann, M. Wandt, O. Paul, W. Dominicus, R. Roth, K. Seitz, and W. Strauss, "Novel 3D piezoresistive silicon force sensor for dimensional metrology of micro components," *IEEE Sensors 2005*, Irvine, USA, Nov 2005.

[5] E. Peiner and L. Doering, "Force calibration of stylus instruments using silicon microcantilevers," *Sensors and Actuators A: Physical,* vol. 123-24, pp. 137-145, Sep 2005.

[6] J. C. Doll, S. Park, A. J. Rastegar, N. Harjee, J. R. Mallon, G. C. Hill, A. A. Barlian, and B. L. Pruitt, "Force sensing optimization and applications," *Advanced Materials and Technologies for Micro/Nano-Devices, Sensors and Actuators*, Springer Netherlands, 2010, pp. 287-298.

[7] M. S. Kim and J. R. Pratt, "SI traceability: Current status and future trends for forces below 10 micronewtons," *Measurement,* vol. 43, pp. 169-182, Feb 2010.

[8] K. Abbas, Z. Leseman, and T. Mackin, "A traceable calibration procedure for MEMS-based load cells," *International Journal of Mechanics and Materials in Design,* vol. 4, pp. 383-389, Mar 2008.

[9] S. Yang and M. T. A. Saif, "Microfabricated force sensors and their applications in the study of cell mechanical response," *Experimental Mechanics,* vol. 49, pp. 135-151, Feb 2009.

[10] X. J. Zhang, S. Zappe, R. W. Bernstein, O. Sahin, C. C. Chen, M. Fish, M. Scott, and O. Solgaard, "Integrated optical diffractive micrograting-based injection force sensor," *Transducers: International Conference on Solid-State Sensors, Actuators and Microsystems* Boston, USA, Jun 2003.

[11] Y. Sun and B. J. Nelson, "MEMS capacitive force sensors for cellular and flight biomechanics," *Biomedical Materials,* vol. 2, pp. 16-22, Mar 2007.

[12] M. Despont, G.A. Racine, P. Renaud, and N. F. Rooij, "New design of micromachined capacitive force sensor," *Journal of Micromechanics and Microengineering,* vol. 3, pp. 239-242, Dec 1993.

[13] A. Nafari, A. Danilov, H. Rodjegard, P. Enoksson, and H. Olin, "A micromachined nanoindentation force sensor," *Sensors and Actuators A: Physical,* vol. 123-24, pp. 44-49, Sep 2005.

[14] J. Zlatanova and S. H. Leuba, "Magnetic tweezers: A sensitive tool to study DNA and chromatin at the single-molecule level," *Biochemistry and Cell Biology,* vol. 81, pp. 151-159, Jun 2003.

[15] C. C. Huang, C. F. Wang, D. S. Mehta, and A. Chiou, "Optical tweezers as sub-pico-newton force transducers," *Optics Communications,* vol. 195, pp. 41-48, Aug 2001.

[16] Y. Sun, B. J. Nelson, D. P. Potasek, and E. Enikov, "A bulk microfabricated multi-axis capacitive cellular force sensor using transverse comb drives," *Journal of Micromechanics and Microengineering,* vol. 12, pp. 832-840, Nov 2002.

[17] Y. T. Shen, N. Xi, W. J. Li, and J. D. Tan, "A high sensitivity force sensor for microassembly: Design and experiments," *IEEE/ASME International Conference on Advanced Intelligent Mechatronics (AIM)*, Kobe, Japan, Jul 2003.

[18] A. Sieber, P. Valdastri, K. Houston, C. Eder, O. Tonet, A. Menciassi, and P. Dario, "A novel haptic platform for real time bilateral biomanipulation with a MEMS sensor for triaxial force feedback," *Sensors and Actuators A: Physical,* vol. 142, pp. 19-27, Mar 2008.

[19] A. Tibrewala, A. Phataralaoha, and S. Buttgenbach, "Simulation, fabrication and characterization of a 3D piezoresistive force sensor," *Sensors and Actuators A: Physical,* vol. 147, pp. 430-435, Oct 2008.

[20] W. L. Jin and C. D. Mote Jr., "Development and calibration of a sub-millimeter three-component force sensor," *Sensors and Actuators A: Physical,* vol. 65, pp. 89-94, Feb 1998.

[21] D. Diddens, D. Reynaerts, and H. Van Brussel, "Design of a ring-shaped three-axis micro force/torque sensor," *Sensors and Actuators A: Physical,* vol. 46, pp. 225-232, Jan 1995.

[22] F. Beyeler, S. Muntwyler, Z. Nagy, C. Graetzel, M. Moser, and B. J. Nelson, "Design and calibration of a MEMS sensor for measuring the force and torque acting on a magnetic microrobot," *Journal of Micromechanics and Microengineering,* vol. 18, p. 025004, Feb 2008.

[23] F. Beyeler, S. Muntwyler, and B. J. Nelson, "A six-axis MEMS force-torque sensor with micro-newton and nano-newtonmeter resolution," *Journal of Microelectromechanical Systems,* vol. 18, pp. 433-441, Apr 2009.

[24] "World MEMS test equipment markets," *Frost & Sullivan,* 2008.

[25] "World co-ordinate measuring machines markets," *Frost & Sullivan,* 2005.

[26] "World micro metrology equipment markets," *Frost & Sullivan,* 2007.

[27] "World mechanical test equipment markets " *Frost & Sullivan,* 2008.

[28] D. Dusharme, "Micro measurement for a micro world," *Quality Digest,* Mar 2006.

[29] Carl Zeiss Industrial Metrology, http://www.zeiss.com/f25, Aug 2010, *F25 Microsystem CMM*.

[30] Mitutoyo Corporation, http://www2.mitutoyo.de/uploads/media/14_Vision_Measuring _Systems_01.pdf, Aug 2010, *Vision measuring systems*.

[31] J. R. Pratt, J. A. Kramar, D. B. Newell, and D. T. Smith, "Review of SI traceable force metrology for instrumented indentation and atomic force microscopy," *Measurement Science & Technology,* vol. 16, pp. 2129-2137, Nov 2005.

[32] E. Peiner, L. Doering, M. Balke, and A. Christ, "Silicon cantilever sensor for micro-/nanoscale dimension and force metrology," *Microsystem Technologies: Micro-and Nanosystems Information Storage and Processing Systems,* vol. 14, pp. 441-451, Apr 2008.

[33] A. Cherry, J. Abadie, and E. Piat, "Microforce sensor for microbiological applications based on a floating-magnetic principle," *IEEE International Conference on Robotics and Automation (ICRA)*, Roma, Italy, Apr 2007.

[34] L. D. Wang, J. K. Mills, and W. L. Cleghorn, "Development of an electron tunneling force sensor for the use in microassembly," *Microsystems and Nanoelectronics Research Conference (MNRC)*, Ottawa, Canada, Oct 2008.

[35] S. Fahlbusch and S. Fatikow, "Force sensing in microrobotic systems an overview," *IEEE International Conference on Electronics, Circuits and Systems (ICECS)*, Lisbon, Portugal, Sep 1998.

[36] Irvine Sensors Inc., http://www.irvine-sensors.com, Sep 2010.

[37] M. Wautelet, "Scaling laws in the macro-, micro- and nanoworlds," *European Journal of Physics,* vol. 22, pp. 601-611, Oct 2001.

[38] J. W. Judy, "Microelectromechanical systems (MEMS): Fabrication, design and applications," *Smart Materials & Structures,* vol. 10, pp. 1115-1134, Dec 2001.

[39] F. Beyeler, S. Muntwyler, Z. Nagy, M. Moser, and B. J. Nelson, "A multi-axis MEMS force-torque sensor for measuring the load on a microrobot actuated by magnetic fields," *IEEE/RSJ International Conference on Intelligent Robots and Systems (IROS)*, San Diego, USA, Oct 2007.

[40] Y. Zhu and H. D. Espinosa, "An electromechanical material testing system for in situ electron microscopy and applications," *Proceedings of the National Academy of Sciences of the United States of America,* vol. 102, pp. 14503-14508, Oct 2005.

[41] J. J. Brown, J. W. Suk, G. Singh, A. I. Baca, D. A. Dikin, R. S. Ruoff, and V. M. Bright, "Microsystem for nanofiber electromechanical measurements," *Sensors and Actuators A: Physical,* vol. 155, pp. 1-7, Oct 2009.

[42] H. Kahn, R. Ballarini, R. L. Mullen, and A. H. Heuer, "Electrostatically actuated failure of microfabricated polysilicon fracture mechanics specimens," *Proceedings of the Royal Society A: Mathematical Physical and Engineering Sciences,* vol. 455, pp. 3807-3823, Oct 1999.

[43] M. T. A. Saif and N. C. MacDonald, "A millinewton microloading device," *Sensors and Actuators A: Physical,* vol. 52, pp. 65-75, Mar 1996.

[44] H. Sato, T. Fukuda, F. Arai, K. Itoigawa, and Y. Tsukahara, "Parallel-beam sensor/actuator unit and its application to the gyroscope," *IEEE/ASME Transactions on Mechatronics,* vol. 5, pp. 266-272, Sep 2000.

[45] F. Beyeler, A. Neild, S. Oberti, D. J. Bell, Y. Sun, J. Dual, and B. J. Nelson, "Monolithically fabricated microgripper with integrated force sensor for manipulating microobjects and biological cells aligned in an ultrasonic field," *Journal of Microelectromechanical Systems,* vol. 16, pp. 7-15, Feb 2007.

[46] GEMAC Chemnitz GmbH, http://www.gemac.info, Sep 2010.

[47] N. A. Burnham, X. Chen, C. S. Hodges, G. A. Matei, E. J. Thoreson, C. J. Roberts, M. C. Davies, and S. J. B. Tendler, "Comparison of calibration methods for atomic-force microscopy cantilevers," *Nanotechnology,* vol. 14, pp. 1-6, Jan 2003.

[48] M. S. Kim, "The status of academic and industrial force metrology below 1 N and the corresponding strategy at KRISS," *International Measurement Confederation (IMEKO)*, Rio de Janeiro, Brazil, Sep 2006.

[49] Z. J. Jabbour and S. L. Yaniv, "The kilogram and measurements of mass and force," *Journal of Research of the National Institute of Standards and Technology,* vol. 106, pp. 25-46, Jan 2001.

[50] National Physical Laboratory, http://www.npl.co.uk/engineering-measurements/mass-force-pressure/mass/research/redefining-the-kilogram, Aug 2010, *Redefining the kilogram*.

[51] M. S. Kim, J. H. Choi, J. H. Kim, and Y. K. Park, "SI-traceable determination of spring constants of various atomic force microscope cantilevers with a small uncertainty of 1%," *Measurement Science & Technology,* vol. 18, pp. 3351-3358, Nov 2007.

[52] L. Liew, J.M. Moreland, and J. R. Pratt, "Design of a MEMS force sensor for quantitative measurement in the nano- to piconewton range," unpublished.

[53] P. J. Cumpson and J. Hedley, "Accurate analytical measurements in the atomic force microscope: a microfabricated spring constant standard potentially traceable to the SI," *Nanotechnology,* vol. 14, pp. 1279-1288, Dec 2003.

[54] M. S. Kim, J. H. Choi, Y. K. Park, and J. H. Kim, "Atomic force microscope cantilever calibration device for quantified force metrology at micro- or nano-scale regime: The nano force calibrator (NFC)," *Metrologia,* vol. 43, pp. 389-395, Oct 2006.

[55] R. S. Gates and J. R. Pratt, "Prototype cantilevers for SI-traceable nanonewton force calibration," *Measurement Science & Technology,* vol. 17, pp. 2852-2860, Oct 2006.

[56] P. J. Cumpson, P. Zhdan, and J. Hedley, "Calibration of AFM cantilever stiffness: A microfabricated array of reflective springs," *Ultramicroscopy,* vol. 100, pp. 241-251, Aug 2004.

[57] I. Behrens, L. Doering, and E. Peiner, "Piezoresistive cantilever as portable micro force calibration standard," *Journal of Micromechanics and Microengineering,* vol. 13, pp. 171-177, Jul 2003.

[58] J.R. Pratt, J.A. Kramar, G.A. Shaw, D.T. Smith, and J.M. Moreland, "A piezoresistive cantilever force sensor for direct AFM force calibration," *Materials Research Society Spring Meeting*, San Francisco, USA, Apr 2007.

[59] M.S. Kim, J.H. Choi, N.H. Bae, and B.I. Kim, "Piezoresistive cantilever for accurate force measurements at the micro/nano-size level," *International Congress and Exposition on Experimental and Applied Mechanics*, Orlando, USA, Jun 2008.

[60] Joint Committees for Guides in Metrology, "Guide to the expression of uncertainty in measurement," *International Organization for Standardization,* 2008.

[61] Joint Committees for Guides in Metrology, "International vocabulary of metrology — Basic and general concepts and associated terms (VIM)," *International Organization for Standardization,* 2007.

[62] Joint Committees for Guides in Metrology, "Supplement 1 to the guide to the expression of uncertainty in measurement − Propagation of distributions using a Monte Carlo method," *International Organization for Standardization,* 2008.

[63] Joint Committees for Guides in Metrology, "Draft: Supplement 2 to the guide to the expression of uncertainty in measurement − Models with any number of output quantities," *International Organization for Standardization,* 2009.

[64] I. Marson, H. Kahle, F. Chaperon, St Mueller, and F. Alasia, "Absolute gravity measurements in Switzerland: Definition of a base network for geodynamic investigations and for the Swiss fundamental gravity net," *Journal of Geodesy,* vol. 55, pp. 203-217, 1981.

[65] B. E. Kratochvil, L. X. Dong, and B. J. Nelson, "Real-time rigid-body visual tracking in a scanning electron microscope," *International Journal of Robotics Research,* vol. 28, pp. 498-511, Apr 2009.

[66] R. S. Fearing, "Survey of sticking effects for micro parts handling," *IEEE/RSJ International Conference on Intelligent Robots and Systems (IROS)*, Pittsburgh, USA, Aug 1995.

[67] A. Goktepe and E. Kocaman, "Analysis of camera calibrations using direct linear transformation and bundle adjustment methods," *Scientific Research and Essays,* vol. 5, pp. 869-872, May 2010.

[68] M. Guthold, W. Liu, E. Sparks, L. Jawerth, L. Peng, M. Falvo, R. Superfine, R. Hantgan, and S. Lord, "A comparison of the mechanical and structural properties of fibrin fibers with other protein fibers," *Cell Biochemistry and Biophysics,* vol. 49, pp. 165-181, Oct 2007.

[69] J. M. Gosline, P. A. Guerette, C. S. Ortlepp, and K. N. Savage, "The mechanical design of spider silks: From fibroin sequence to mechanical function," *Journal of Experimental Biology,* vol. 202, pp. 3295-3303, Dec 1999.

[70] W. Liu, L. M. Jawerth, E. A. Sparks, M. R. Falvo, R. R. Hantgan, R. Superfine, S. T. Lord, and M. Guthold, "Fibrin fibers have extraordinary extensibility and elasticity," *Science,* vol. 313, p. 634, Aug 2006.

[71] J. P. Collet, H. Shuman, R. E. Ledger, S. T. Lee, and J. W. Weisel, "The elasticity of an individual fibrin fiber in a clot," *Proceedings of the National Academy of Sciences of the United States of America,* vol. 102, pp. 9133-9137, Jun 2005.

[72] H. Lu, B. Isralewitz, A. Krammer, V. Vogel, and K. Schulten, "Unfolding of titin immunoglobulin domains by steered molecular dynamics simulation," *Biophysical Journal,* vol. 74, pp. A275-A275, Feb 1998.

[73] P. E. Marszalek, H. Lu, H. B. Li, M. Carrion-Vazquez, A. F. Oberhauser, K. Schulten, and J. M. Fernandez, "Mechanical unfolding intermediates in titin modules," *Nature,* vol. 402, pp. 100-103, Nov 1999.

[74] V. Vogel, "Mechanotransduction involving multimodular proteins: Converting force into biochemical signals," *Annual Review of Biophysics and Biomolecular Structure,* vol. 35, pp. 459-488, Feb 2006.

[75] E. Zamir, M. Katz, Y. Posen, N. Erez, K. M. Yamada, B. Z. Katz, S. Lin, D. C. Lin, A. Bershadsky, Z. Kam, and B. Geiger, "Dynamics and segregation of cell-matrix adhesions in cultured fibroblasts," *Nature Cell Biology,* vol. 2, pp. 191-196, Apr 2000.

[76] C. L. Zhong, M. Chrzanowska-Wodnicka, J. Brown, A. Shaub, A. M. Belkin, and K. Burridge, "Rho-mediated contractility exposes a cryptic site in fibronectin and induces fibronectin matrix assembly," *Journal of Cell Biology,* vol. 141, pp. 539-551, Apr 1998.

[77] G. Baneyx, L. Baugh, and V. Vogel, "Fibronectin extension and unfolding within cell matrix fibrils controlled by cytoskeletal tension," *Proceedings of the National Academy of Sciences of the United States of America,* vol. 99, pp. 5139-5143, Apr 2002.

[78] G. Baneyx and V. Vogel, "Self-assembly of fibronectin into fibrillar networks underneath dipalmitoyl phosphatidylcholine monolayers: Role of lipid matrix and tensile forces," *Proceedings of the National Academy of Sciences of the United States of America,* vol. 96, pp. 12518-12523, Oct 1999.

[79] J. Ulmer, B. Geiger, and J. P. Spatz, "Force-induced fibronectin fibrillogenesis in vitro,"

Soft Matter, vol. 4, pp. 1998-2007, Oct 2008.

[80] W. C. Little, M. L. Smith, U. Ebneter, and V. Vogel, "Assay to mechanically tune and optically probe fibrillar fibronectin conformations from fully relaxed to breakage," *Matrix Biology,* vol. 27, pp. 451-461, Jun 2008.

[81] E. Klotzsch, M. L. Smith, K. E. Kubow, S. Muntwyler, W. C. Little, F. Beyeler, D. Gourdon, B. J. Nelson, and V. Vogel, "Fibronectin forms the most extensible biological fibers displaying switchable force-exposed cryptic binding sites," *Proceedings of the National Academy of Sciences of the United States of America,* vol. 106, pp. 18267-18272, Oct 2009.

[82] J. C. Doll, S. Muntwyler, F. Beyeler, S. Geffeney, M. B. Goodman, B. J. Nelson, and B. L. Pruitt, "Measuring thresholds for touch sensation in C. elegans," *International Conference on Microtechnologies in Medicine and Biology (MMB)*, Quebec City, Canada, Apr 2009.

[83] A. Geitmann and J. K. E. Ortega, "Mechanics and modeling of plant cell growth," *Trends in Plant Science,* vol. 14, pp. 467-478, Sep 2009.

[84] National Physical Laboratory, "Buoyancy correction and air density measurement," *Good Practice Guidance,* 2002.

[85] L.K. Baxter, *Capacitive sensors: Design and applications*. New York: IEEE Press, 1997.

8 Appendix

8.1 Additional Source of Uncertainty

In the uncertainty analysis presented in Chapter 3, only the most relevant sources of uncertainty are considered. There are a number of additional sources that are neglected and not described in the analysis, since their magnitude will not have a significant influence within the considered numbers of digits.

For completeness, these additional sources of uncertainty are described in the following section; the estimation of their magnitude demonstrates their irrelevance for the uncertainty analysis.

Buoyancy correction

Variations in environmental conditions, such as temperature, barometric pressure and humidity, will affect the density of air, and therefore influence the buoyancy a mass artifact experiences, ultimately resulting in a variation in the force it exerts on a force sensor. Based on this effect, the variation in the buoyancy force can be calculated using the methodology presented in [84]. The resulting standard uncertainty, induced to the largest calibration weight used during the macroscale reference-force sensor calibration (4.4mN), is ~13 nN, 7nN and 1nN, based upon standard uncertainties of the temperature of 5°C, barometric pressure of 10 mbar, and relative humidity of 20%. Due to the small magnitude of these variations relative to the absolute magnitude of the applied calibration weight ($\sim 3 \cdot 10^{-6}$ for a 5°C temperature change), the variations in the buoyancy force are neglected in the uncertainty analysis of the force sensors.

Absolute gravitational acceleration *g*

The absolute gravitational acceleration g in Zurich, Switzerland has been measured in a joint effort by ETH Zurich, the University of Trieste and the Istituto di Metrologia in Torino. The measurements in Zurich (on June 7, 1978) showed that $g = 9.80647895$ m/s^2 [64]. A variation in g, related to a possible difference in the elevation of up to 100 m between the location of this gravitational measurement and the location of the force sensor calibration, results in a relative change of the gravitational constant of $\Delta g/g = 2.6 \cdot 10^{-5}$. Therefore, the uncertainty in g can be neglected in the uncertainty analysis of the force sensor.

Permittivity of the dielectric, ε

The permittivity of air changes with pressure, temperature, and humidity. At standard temperature (20°C) and pressure (1 atm), the permittivity of air changes with temperature at 2 ppm/°C for dry air, increasing to 7 ppm /°C for moist air. At 20°C, the permittivity of air changes with relative humidity at 1.4 ppm/% RH. A change of pressure of 1 atm changes the permitivity by 100 ppm [85]. As described by (2.13) these variations in the permittivity will influence the sensitivity of the sensing probes, but are of such small magnitude that they can be neglected.

Hysteresis

The uncertainty due to hysteresis is a result of a difference between the outputs of the sensor at a specified input when it is approached from the opposite direction. This uncertainty is characterized by the student's t-distribution, with N-1 degrees of freedom, where N is the number of measurements of the difference between the outputs when being approached from the opposite direction at a specific input. Due to the single crystalline material from which the microforce-sensing tools are fabricated, no hysteresis in their characteristics could be detected, as can be seen in Fig. 33, and is therefore neglected in the uncertainty analysis.

8.2 Process Sequence for the SOI-Based Tools

The details of this process sequence are classified as confidential.

The details of this process sequence are classified as confidential.

The details of this process sequence are classified as confidential.

8.3 Process Sequence for the Double SOI-Based Tools

The details of this process sequence are classified as confidential.

The details of this process sequence are classified as confidential.

The details of this process sequence are classified as confidential.

The details of this process sequence are classified as confidential.

8.4 Capacitive Readout Schematics

The details of the capacitive readout are classified as confidential.

The details of the capacitive readout are classified as confidential.

8.5 Calibration Setup Schematic

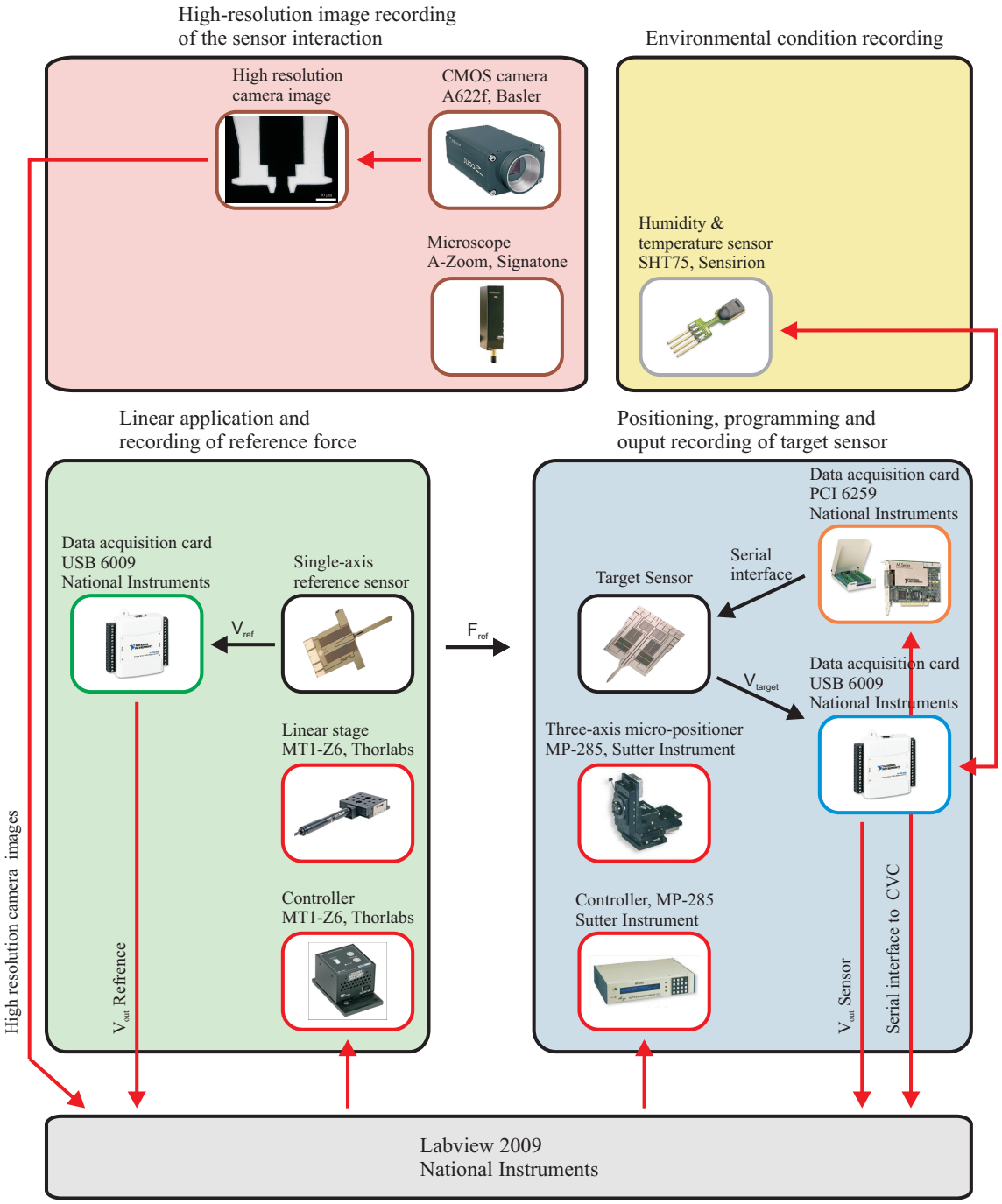

Fig. 53: Schematic of the calibration setup used for single- and multi-axis microforce and position feedback sensor calibration.

Curriculum Vitae

Simon D. Muntwyler

Adresse:	Pflugstrasse 6, 8006 Zurich, Switzerland
E-Mail:	simon.muntwyler@gmail.com
Mobile:	+41 (0) 76 509 63 77
Date / Place of Birth:	21.12.1980 / Zurich
Citizenship:	Switzerland

EDUCATION

Jan 2010 – Sep 2010 **IMD (International Institute for Management Development), Lausanne, Switzerland**

Participated in the EMBA program as a life start-up case, including a venture capital pitch in September 2010 in Silicon Valley

Mar 2007 – Dec 2010 **Doctor of Science (Ph.D.)**
ETH Zurich, Zurich, Switzerland
Institute of Robotics and Intelligent Systems
Thesis: Microforce-Sensing Probes and Methodologies for Micromechanical and Dimensional Metrology

Oct 2001 – Sep 2006 **Master of Science**
ETH Zurich, Zurich, Switzerland
Mechanical and Process Engineering with focus on Microsystems and Robotics
Master thesis: Design, Fabrication and Characterization of 3-Axis Capacitive MEMS Force Sensors
Semester project: Measuring and Modeling of a Wireless Resonant Magnetic Microactuator
Semester project: Microfabrication of a Flexible Polymer-Based Microthermoelectric Generator

Aug 2001 – Oct 2001 **Workshop Training**
Sulzer AG, Winterthur, Switzerland
Basic course in manual and mechanical manufacturing, milling, drilling, welding, etc.

EXPERIENCE

Jul 2007 – Jan 2011 **Chief Technology Officer and Cofounder**
FemtoTools GmBH, Zurich, Switzerland

FemtoTools designs and fabricates MEMS-based, high-quality measurement and handling instruments for research and development in the micro and nano domains.

Jul 2004 – Sep 2004 **Development Engineer Intern**
Paul Scherer Institute (PSI), Villigen, Switzerland
Designed, fabricated and programmed a peltier-based temperature-cycle chamber for the testing of detector chips in the Large Hadron Collider (LHC) of the European Organization for Nuclear Research (CERN)

Oct 2000 – Jul 2002 **Administrator in the IT System Engineering department**
Credit Suisse AG, Zurich, Switzerland

Jun 1998 – Oct 2000 **Scientific Attendant**
Swiss Science Center - Technorama, Wintherthur, Switzerland

AWARDS

- ZKB Pioneer Price Technopark 2010 - "Top three Swiss spin-off companies 2010"
- IMD Start-up Competition 2010
- Swiss Technology Award 2009
- ZKB Pioneer Price Technopark 2009 - "Top three Swiss spin-off companies 2009"
- Best Automation Paper - IEEE International Conference on Robotics and Automation (ICRA 2009)

REFEREED PUBLICATIONS

International peer-reviewed journals

S. Muntwyler, B. E. Kratochvil, F. Beyeler, and B. J. Nelson, "Monolithically integrated two-axis microtensile tester for the mechanical characterization of microscopic samples," Journal of Microelectromechanical Systems, vol. 19, pp. 1223-1233, Oct 2010.

S. Muntwyler, F. Beyeler, and B. J. Nelson, "Three-axis micro-force sensor with sub-micro-newton measurement uncertainty and tunable force range," Journal of Micromechanics and Microengineering, vol. 20, p. 025011, Feb 2010.

(IOP Select: Chosen by the editors for its novelty, significance and potential impact on future research)

E. Klotzsch, M. L. Smith, K. E. Kubow, S. Muntwyler, W. C. Little, F. Beyeler, D. Gourdon, B. J. Nelson, and V. Vogel, "Fibronectin forms the most extensible biological fibers displaying switchable force-exposed cryptic binding sites," Proceedings of the National Academy of Sciences of the United States of America, vol. 106, pp. 18267-18272, Oct 2009.

F. Beyeler, S. Muntwyler, and B. J. Nelson, "A six-axis MEMS force-torque sensor with micro-newton and nano-newtonmeter resolution," Journal of Microelectromechanical Systems, vol. 18, pp. 433-441, Apr 2009.

F. Beyeler, S. Muntwyler, Z. Nagy, C. Graetzel, M. Moser, and B. J. Nelson, "Design and calibration of a MEMS sensor for measuring the force and torque acting on a magnetic microrobot," Journal of Micromechanics and Microengineering, vol. 18, p. 025004, Feb 2008.

W. Glatz, S. Muntwyler, and C. Hierold, "Optimization and fabrication of thick flexible polymer based micro thermoelectric generator," Sensors and Actuators A-Physical, vol. 132, pp. 337-345, Nov 2006.

International peer-reviewed conferences

S. Muntwyler, B. E. Kratochvil, F. Beyeler, and B. J. Nelson, "Two-axis micro-tensile tester chip for measuring plant cell mechanics," IEEE Sensors, Waikoloa, USA, Nov 2010.

F. Beyeler, S. Muntwyler, and B. J. Nelson, "Wafer-level inspection system for the automated testing of comb drive based MEMS sensors and actuators," IEEE Conference on Automation Science and Engineering (CASE), Toronto, Canada, Aug 2010.

S. Muntwyler, F. Beyeler, and B. J. Nelson, "Three-axis micro-force sensor with tunable force range and sub-micronewton measurement uncertainty," IEEE International Conference on Robotics and Automation (ICRA), Anchorage, USA, May 2010.

Z. Nagy, S. Miyashita, S. Muntwyler, A. K. Cherukuri, J. J. Abbott, R. Pfeifer, and B. J. Nelson, "Morphology detection for magnetically self-assembled modular robots," IEEE/RSJ International Conference on Intelligent Robots and Systems (IROS), St. Louis, USA, Oct 2009.

F. Beyeler, S. Muntwyler, and B. J. Nelson, "Design and calibration of a microfabricated 6-axis force-torque sensor for microrobotic applications," IEEE International Conference on Robotics and Automation (ICRA), Kobe, Japan, May 2009.
(Best Automation Paper Award and Best Student Paper Award)

J. C. Doll, S. Muntwyler, F. Beyeler, S. Geffeney, M. B. Goodman, B. J. Nelson, and B. L. Pruitt, "Measuring thresholds for touch sensation in C. elegans," International Conference on Microtechnologies in Medicine and Biology (MMB), Quebec City, Canada, Apr 2009.

G. Dogangil, O. Ergeneman, J. J. Abbott, S. Pane, H. Hall, S. Muntwyler, and B. J. Nelson, "Toward targeted retinal drug delivery with wireless magnetic microrobots," IEEE/RSJ International Conference on Intelligent Robots and Systems (IROS), Nice, France, Sep 2008.

F. Beyeler, S. Muntwyler, and B. J. Nelson, "Design, fabrication and calibration of a silicon micro force-torque sensor," International conference of the European Society for Precision Engineering and Nanotechnology (EUSPEN), Zurich, Switzerland, May 2008.

F. Beyeler, S. Muntwyler, Z. Nagy, M. Moser, and B. J. Nelson, "A multi-axis MEMS force-torque sensor for measuring the load on a microrobot actuated by magnetic fields," IEEE/RSJ International Conference on Intelligent Robots and Systems (IROS), San Diego, USA, Oct 2007.

W. Glatz, S. Muntwyler, and C. Hierold, "Flexible polymer based microthermogenerator," Eurosensors XIX, Barcelona, Spain, Sep 2005.

Book Chapter

S. Muntwyler, F. Beyeler, and B. J. Nelson, " Microforce-sensing probes and methodologies for micromechanical metrology", Signal Measurement and Estimation Techniques for Micro and Nanotechnology, Springer-Verlag GmbH, to appear 2011.

Zurich, January 2011